DEVELOPMENT OF AN AUTONOMOUS IN-SITU BIOPRINTING SYSTEM FOR SKIN

Muhammad Salman Chaudhry

A Dissertation Submitted to the Faculty of Graduate Studies in Partial Fulfillment of the Requirements for the Degree of Doctor of Philosophy

Graduate Program in Earth and Space Science

York University

Toronto, Ontario

May 2024

Abstract

Bioprinting and skin tissue engineering stand at a pivotal threshold, necessitating a leap forward to realize its transformative potential. This study explores the integration of computational models, autonomous robotics, and customized biomaterials as key enablers for successfully navigating the complex anatomical landscape of the human body in bioprinting applications. It introduces a novel in-situ bioprinting approach, designed to precisely deposit biomaterials on unconventional and foreign targets/platforms. Central to this study is the development of an interconnected system that integrates (i) a geometric modeling procedure to generate a free-form/planar toolpath that enables printing on anatomical models, (ii) an autonomous tracking and control algorithm to respond to unprecedented motions of the printing platform, and (iii) a composite hydrogel formulation optimized for the direct extrusion printing process.

Empirical studies demonstrated that the slicing algorithm enhanced bioprinting adaptability and accuracy on free-form surfaces. Two slicing methodologies are proposed to effectively model multi-layered heterogeneous skin implants: top-down and bottom-up approaches. Both approaches leverage the implant interface's surface geometry, mitigating the staircase effect and providing control over interlayer interactions. This advancement is crucial for accurately replicating the structural complexity of skin implants.

Based on real-time visual feedback, the developed asynchronous adaptive tracking and printer control system demonstrated a capability to sustain print quality on substrates moving at speeds of up to 50 mm/min while managing speeds of up to 2500 mm/min. This is achieved by developing a framework for parallel execution of high-level tracking and low-level control algorithms, along with strategic switching between printing and tracking modes. This marks the first instance of successful printing on moving platforms and real-time guidance of the in-situ printing process.

The optimized GelMA/CNF composite biomaterial exhibited enhanced mechanical and rheological properties, indicating its suitability for skin bioprinting applications. Characterizing GelMA's transition temperature sensitivity to heating and cooling rates also facilitated its adaption for the direct extrusion printing process.

In-situ bioprinting technology offers great promise, but the challenges involved are multifaceted and must be addressed to achieve its full potential. While previous works focused on either hardware innovation or bioink development, this dissertation bridges these domains, offering a comprehensive

approach to the challenges of in-situ bioprinting. Objectives in this dissertation are addressed by an interdisciplinary approach, representing incremental advancements needed further to develop the in-situ bioprinting technology for the skin. The research presented herein sets the stage for realizing true bioprinting potential—that extends into revolutionizing wound healing, bioprinting, and the broader field of additive manufacturing.

Keywords: Bioprinting, Non-Planar Surfaces, Autonomous Robotics, Biomaterials, Tissue Engineering, Skin Implants.

Acknowledgments

Embarking on this scholarly journey, I have traversed paths paved with challenges and milestones, accompanied by an extraordinary constellation of individuals whose support was instrumental in shaping both the course of this research and the researcher I have become.

Foremost, I extend my deepest gratitude to my supervisor, Dr. Alex Czekanski, whose wise guidance, unwavering support, and academic rigor provided the beacon I needed to navigate through the complexities of this research. I would also like to extend my sincerest thanks to Dr. George Zhu, whose insightful feedback and unwavering commitment to excellence inspired me to broaden my perspectives and delve more deeply into the spheres of innovation and discovery.

To my fellow researchers and colleagues at the IDEA Lab, thank you for the stimulating discussions, collaborative experiments, and shared moments of breakthrough and contemplation. Our joint endeavors and collective brainstorming sessions were not only integral to the success of this research but also immensely enriching on a personal level.

My heartfelt thanks go to my family, whose love, patience, and belief in my aspirations provided the strength and motivation to persevere through the demanding moments of this academic pursuit. To my wife and children, your understanding and encouragement were my sanctuary; this achievement is as much yours as it is mine.

To all those who directly or indirectly influenced this academic voyage, your roles have been pivotal in the culmination of this endeavor. This thesis not only stands as a testament to my academic pursuit but also as a mosaic of the collective wisdom, support, and inspiration bestowed upon me by each one of you.

Thank you.

Table of Contents

List of Tables

List of Figures

Chapter 1 Introduction

Summary: In this introductory chapter, the foundational framework for the dissertation is laid out, outlining the critical challenges and advancements within the field of 3D bioprinting, particularly focusing on in-situ applications for the case of skin wound healing. The problem statement is defined, emphasizing the limitations of current bioprinting technologies when applied to non-linear and moving surfaces. The research objectives are outlined, and the justification of the study is presented. Finally, the structure of the dissertation is described. This chapter sets the stage for a detailed exploration of the literature, methodologies, and findings supporting the pursuit of these objectives.

1.1 Background

The advent of 3D bioprinting has opened new horizons in the fields of tissue engineering and regenerative medicine, offering groundbreaking approaches to traditional medical challenges. This technology, which enables the layer-by-layer construction of biological structures, has the potential to revolutionize healthcare by providing personalized, patient-specific tissues and organs [1]. Despite its promise, the application of 3D bioprinting has predominantly been confined to controlled environments, with a focus on static, flat surfaces that are disconnected from the dynamic nature of human anatomy [2].

The human body presents a complex landscape, constantly in motion and marked by its unique topography. Current bioprinting technologies face challenges when applied directly to the body, particularly due to the inability to adapt to living tissues' free-form and unpredictable nature [3]. These challenges include maintaining precision and stability during printing, ensuring material compatibility with human biology, and achieving functional integration post-implantation [4] [5]. The necessity for bioprinting capabilities that transcend these limitations is clear, especially for in-situ applications such as skin repair, where printing directly onto the patient could drastically reduce recovery times and improve clinical outcomes [6]. However, developing such advanced bioprinting systems requires a multidisciplinary approach, integrating insights from biology, material science, mechanical engineering, and computer vision/robotics. In response to this need, recent research efforts have begun to explore the possibilities of dynamic, in-situ bioprinting, aiming to create systems capable of operating directly on the human body [7]. These systems must compensate for human movement,

adapt to various surface topologies, and deposit biologically viable materials that can integrate seamlessly with existing tissues.

An integrated approach combining advanced robotic systems, bioprinting materials, and software algorithms is developed in this dissertation to address the gaps in current technology. By pushing the boundaries of what is currently possible in bioprinting, this research aims to bring us a step closer to a future where damaged tissues can be repaired or replaced directly at the point of care, tailored to each patient's specific needs. The importance of this research extends beyond the technical achievements. As the technology matures, it promises to improve patient outcomes, making treatments more accessible and adaptable [8].

1.2 Problem Statement

While rapidly advancing, the landscape of in-situ bioprinting confronts several substantial barriers when transitioning from theoretical models and benchtop experiments to practical, clinical applications. The primary obstacle lies in the technology's inability to adequately address human tissues and organs' dynamic, non-linear nature [9]. Traditional bioprinting techniques, which have shown remarkable success in creating static structures, falter when applied to the living human body, which presents a moving, breathing, and ever-changing platform.

This discrepancy between existing bioprinting capabilities and the requirements for successful in-situ tissue regeneration constitutes a gap in the field. The challenges are multifaceted: they include the need for systems that can accurately adapt to and print on moving surfaces, such as those affected by physiological movements like heartbeat and respiration [10]; the development of materials that not only mimic the complex properties of natural tissues but also adhere and integrate seamlessly when deposited onto a living host; and the creation of robust, precise, and flexible robotic platforms capable of executing this high-stakes printing while avoiding errors.

Moreover, bioprinting on dynamic surfaces involves complex mechanical and biological variables, requiring advanced control systems and feedback mechanisms to adjust the printing parameters in real-time [11]. The absence of such sophisticated systems results in the current state where bioprinting is largely limited to external body parts or in vitro applications, restricting its potential impact on direct wound healing and internal organ repair.

The problem is compounded by the lack of cost-effective, scalable solutions that can be widely adopted in clinical settings. While there have been notable individual successes in bioprinting, the field lacks

an integrated approach that combines the technological innovations necessary for breakthrough in-situ applications. The necessity for a solution that addresses these technical and practical challenges is critical not only for advancing bioprinting technology but also for the future of personalized medicine and regenerative therapies.

1.3 Research Objectives

This dissertation is dedicated to advancing the field of 3D bioprinting, particularly focusing on challenges that hinder the ability to print directly on the human body, a non-stationary and non-linear platform. The research is structured around four primary objectives, which are detailed below:

Objective I Development of a Free-Form Toolpath Generation for Skin Implant Modelling (Bioprinting on a Non-Planar Surface)

- Develop and refine an algorithm tailored for slicing free-form surfaces suitable for skin implant modeling. Address the non-planarity of the printing platform by establishing advanced tool path planning methodologies that prevent self-collision and ensure precise deposition.
- Incorporate a comprehensive 3D integration process for the target surface of the host platform within the slicing algorithm, enabling accurate localization of implant directly on the complex anatomical platform.
- Develop a low-cost, modular bioprinting hardware platform engineered to support in-situ bioprinting scenarios for skin implants. The design should facilitate adaptability to various printing environments, techniques, and materials, enabling future research.

Objective II Development of Autonomous Capabilities in a Bioprinter for Handling Non-Stationary Platform (Bioprinting on a Moving Surface)

- Create a modular and adaptable robotic framework that can support the bioprinting system, specifically tailored to navigate and operate on undulating and moving surfaces.
- Innovate and implement visual servo control strategies and mechanisms within the robotic framework. These should be designed to detect and respond dynamically to platform movements, including involuntary motions such as breathing or muscle twitches, at speeds up to 60 mm/min and 20 cycles/min.
- Develop a sophisticated software architecture capable of managing the parallel execution of printing tasks and real-time disturbance handling. This architecture should facilitate seamless

integration between the operations and the robotic system's response mechanisms, ensuring uninterrupted and accurate printing performance on non-stationary models.

Objective III Development of Bioprinting Materials Suitable for In-Situ Skin Printing (Biomaterials for In-situ Process)

- Formulate a biomaterial suitable for the process of in-situ bioprinting of skin implants based on visible light-based photopolymerization.
- Characterize and optimize the biomaterial for direct extrusion printing.
- Assess the formulated biomaterial through mechanical and rheological studies at various concentrations and states before and after cross-linking to ensure they meet the criteria for successful in-situ printing.

Objective IV Development and Integration of a Robotic System for Simulating In-Situ Bioprinting of Skin Implants (System Integration)

- Integrate the developed slicing algorithm, robotic framework, and biomaterial into an integrated platform.
- Facilitate comprehensive in-situ bioprinting experiments, enabling seamless operation and testing.
- Test the integrated bioprinting platform to identify and address any operational challenges.

These objectives guide the research towards a solution that addresses current limitations in bioprinting technology, aiming to impact the fields of in-situ fabrication.

1.4 Justification of the Study

Adapting traditional 3D bioprinting technologies to real-time clinical settings requires bridging the technical gap between traditional and emerging technologies [12]. Current bioprinting methods are primarily limited to static and flat surfaces, restricting their utility for direct applications on the human body, which presents complex, moving, and non-linear surfaces due to physiological activities like breathing and heartbeat.

This research addresses the critical challenges associated with in-situ bioprinting, particularly the need for systems that can adapt to and function on human tissues' unpredictable and varying topography. Developing a bioprinting system capable of accurate and precise operation on dynamic platforms is required to realize the full potential of robotic tissue engineering. Moreover, developing bioprinting

materials that are optimized for printing are essential for enhancing the integration and functionality for skin tissue printing [13]. The study's focus on creating adaptable, skin-like biomaterials responds to the urgent need for effective healing in the context of burns, wounds, and other skin conditions.

1.5 Dissertation Structure

This dissertation is organized into a structured framework to guide the reader through the comprehensive research. Below is a chapter-by-chapter description of the content and objectives of each part of the study:

Chapter 1 outlines the background of the research, highlighting the existing challenges and gaps in the field of 3D bioprinting and its application to dynamic, non-linear human tissues. The problem statement, research objectives, and importance of the study are defined, providing a clear rationale for the research. This chapter aims to establish the context and the scope of the study, setting the groundwork for the subsequent chapters.

Chapter 2 presents a comprehensive review of the existing literature on 3D bioprinting, robotic systems, biomaterials, and in-situ tissue engineering. This section critically evaluates previous studies, identifying their strengths, weaknesses, and gaps the current research aims to fill. The review provides a theoretical and empirical foundation for the study.

Chapter 3 is dedicated to developing and challenging a bioprinting system designed for non-planar surfaces. It covers the design process, development challenges, and testing methodologies. The chapter aims to provide a detailed account of the technical and practical considerations involved in adapting bioprinting technologies to complex surface geometries.

Chapter 4 focuses on the engineering and implementation of bioprinting systems for moving platforms; this chapter discusses the design of adaptive robotic systems, control strategies for motion compensation, and integrating these elements into the bioprinting process.

Chapter 5 is dedicated to formulating and characterizing biomaterial that is optimized for the printing process in skin tissue applications. It details the process of biomaterial development, from formulation to characterization, and discusses how these biomaterials are optimized for use in bioprinting applications. The chapter also examines the integration of these biomaterials into the broader bioprinting process and their performance in practical applications.

Chapter 6 deals with the comprehensive integration of developed technologies, focusing on autonomous robotic systems, slicing advancements, and biomaterial formulations into a bioprinting framework. This chapter discusses the step-by-step process of system integration, detailing each component, ranging from motion tracking and control algorithms to biomaterial delivery mechanisms, within the bioprinting ecosystem.

Chapter 7 summarizes the key findings of the research and discusses their implications for the field of bioprinting. Limitations of the current study and areas for future research are outlined to provide a roadmap for subsequent work in the field. This chapter concludes with a reflection on the broader impacts of the study and its potential contributions to advancing bioprinting technologies and applications.

Chapter 2 Literature Review

Summary: This chapter provides a comprehensive literature review on the emerging field of bioprinting, with a special focus on in-situ techniques for skin regeneration. The chapter begins with an introduction to bioprinting, outlining its significance and applications in tissue engineering and regenerative medicine. It then discusses in-situ bioprinting techniques, highlighting their potential to create tissue-analogous structures directly on patients. In subsequent sections, in-situ bioprinting techniques are dissected into robotic and hand-held approaches, offering insights into their operational frameworks and applicability in clinical settings. The discussion extends to slicing strategies and software solutions, contrasting traditional methods with advanced techniques tailored for non-planar and free-form surface printing, essential for realistic and functional tissue constructs. The chapter also addresses the practicality of in-situ fabrication on moving platforms, incorporating visual tracking and localization techniques from medical robotics to enhance printing accuracy and efficacy. It concludes with an overview of the field's challenges and prospects, from standardization and regulatory approvals to cell sourcing and clinical cost considerations.

2.1 Introduction to Bioprinting

The ability to replace and repair human organs and tissues has long been a human aspiration. Since the first successful organ transplant in 1954, transplantation medicine has evolved and expanded rapidly. However, there is no single country where donor rates meet the organ demand. Advances in bio-printing have propelled the field of tissue regeneration from science fiction to reality. Bio-printing refers specifically to the ‘3D printing’ of biological tissue structures capable of mimicking normal tissue function. This is accomplished by layer-by-layer deposition of bioink (bio-materials comprising live cells) in predefined 3D structures designed by computer-aided design (CAD) software [14] [15]. For a variety of applications, including drug screening, biomolecule delivery, disease modeling, regenerative medicine [16], and biohybrid robotics [14] [17], a functional 3D tissue or organ can be constructed by selecting appropriate bio-materials (live cells and various growth and differentiation factors). A bio-printer provides sufficient spatial control over developing constructs to aid the natural cellular repair process, a crucial element of the development of regenerative therapies. Therefore, the global research effort dedicated towards both bio-printing techniques is at a promising preliminary stage but is rapidly growing [18] [19] [20].

Skin is one of the largest organs of the human body, and as it forms the exterior of the body, it is also prone to wounds and burns of different types. Since the inception of in-situ bioprinting of skin in 2010 [21] [22], the ongoing interest of the research community has been proven by an ever-growing number of works published in the last few years dealing with materials [23], methods [24], and processes for its application in the skin [25].

Next, this chapter discusses a comprehensive review of the in-situ bioprinting of skin tissue, including an overview of the immune response to wound healing and the host response to biomaterials. This is followed by a discussion on the skin's mechanical structure and regeneration process and details about traditional and bioprinting-based wound healing strategies used for skin engineering. Finally, a comprehensive review of works dealing with in-situ skin bioprinting is discussed and analyzed.

2.2 Bioprinting Techniques

The most common bio-printing technique is *in vitro*, where the biological tissue is created in the lab for later transplantation to the needed site (see Figure 2-1(a)). However, this process has several challenges regarding the logistics of bio-implantation [16], as the fabrication of tissue is carried out outside its biological context. Regeneration requires a controlled environment in a bioreactor with the appropriate chemical and physical signals. Moreover, there is a risk of contamination in the storage, transportation, handling, and implantation phase, so a high degree of sterilization is required. In addition, the implant needs to maintain its structural integrity without swelling or shrinking after printing. Due to the resolution limitations related to the scanning and printing method, in vitro bioprinting can also result in a loss of geometric fit [25]. Geometric mismatch introduces unwanted surface features at the interacting surface, which can hinder regeneration by blocking essential environmental cues.

In the last two decades, tissues have also been fabricated or repaired directly on the intended anatomical location in the living body, using the body as a bioreactor [26]. This *in vivo* procedure, also known as *in-situ* bio-printing, constitutes a very promising research field. In-situ bioprinting occurs in the infected organ, such as the liver, spleen, or kidney. In the in-situ bioprinting process, live cells are grown on the patient (see Figure 2-1(b)). The tissue-based 3D printer builds a complete replica of the implanted tissue with a substance called “inks/bioinks" made of soft hydrogels. Cells are planted in the bioprinting chambers through a syringe pump and matured by protein-based crosslinking or sustained exposure to artificial light. The in-situ bioprinting process involves the biological material being grown on a live body with 3D bioprinting machines. Since the conception of printing tissue-like biostructure

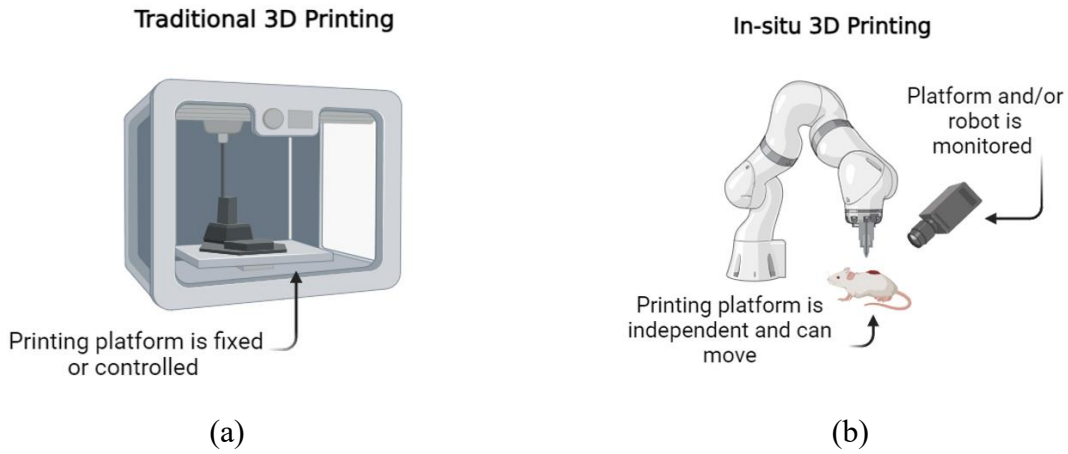

Figure 2-1: (a) In vitro printing scenario used in desktop printing: The platform here is stationary or controlled, (b) In-situ printing scenario: Printing is performed on a non-cooperative platform, a non-planar platform.

in-situ in 2007 [27], approaches based on robotics and hand-held delivery of biomaterial have been proposed for skin, cartilage, and bone fabrication, with great potential for future clinical translation.

The main utility of in-situ bioprinting over in vitro is that it does not involve recapitulating the microenvironment of the native tissue. The natural presence of the biochemical and biophysical signals in the host site supports different phases of cellular regeneration, like proliferation, differentiation, and migration [28]. Additionally, ease of handling, reduced costs, less labor involvement, and potentially fewer regulatory obstacles to in-situ bioprinting approaches than in vitro methods have become more attractive [26]. Although the two processes seem to be similar as they are based on the 3D printing of biological materials, the implications are multidisciplinary in nature, arising mainly due to the dynamic complexity of the in-situ printing environment. The in vitro bioprinting technology is adopted from and developed on desktop 3D bioprinting systems. Such systems can be described as having, at most, 3 degrees of motion and a controlled and planar deposition platform. In-situ bioprinting aims to fabricate structures on nonplanar and free-form surfaces that are not controlled and prone to movements and disturbances. Therefore, further advancement of 3D printing technology itself is crucial for such a highly complex and dynamic application of in-situ bioprinting.

2.3 Printing Modalities for Bioprinting

2.3.1 Extrusion Deposition

Among the various approaches to 3D bioprinting, extrusion-based deposition systems depend primarily on controlling the material's mechanical and temporal characteristics. The apparatus consists of syringe-like equipment mounted on an XYZ positioning system. Printing polymer or hydrogel by this

method facilitates extrusion through a syringe tip, controlled by pneumatic pressure, mechanical pistons, or computer software that drives the printing protocol. Because printing relies heavily on material properties, bioink must be viscous enough to extrude smoothly through a tip or nozzle of a small diameter to facilitate smooth extrusion and support itself mechanically in a 3D structure after deposition. The material's rheological properties can be tailored so that extruded filaments of the bioink will retain their shape even after they are extruded, such as by changing their elastic modulus. Furthermore, fluid-like components may still be present in the material, making extrusion possible.

2.3.2 Microfluidic Extrusion

Recent advances have been made by integrating microfluidic technology with extrusion-based bioprinting. Additionally, this system allows the extrusion of multiple bioinks through the same nozzle simultaneously, as well as precise control of the flow of the bioink. Microfluidic systems can be integrated with 3D bioprinters to fabricate high-resolution vascularized structures, fibers, and hollow structures [29]. Cell survival is improved by allowing oxygen and nutrients to diffuse freely through hollow microchannels within the construct. Cellular and material components cannot be precisely positioned, and pressure and flow are unstable. The fabrication of skin substitutes has been explored using microfluidics-assisted extrusion printing. An approach based on microfluidics was developed to fabricate skin tissue-like structures by printing living cells into sheets. The results of the murine wound model showed that an alginate hydrogel with human fibroblasts promotes wound healing and keratinization. A handheld device with a microfluidic printhead was developed to deliver biomaterials and cells directly to wounds using a microfluidic printhead [30]. The fibrin sheets had been shown to improve wound healing in porcine models with full-thickness burns by promoting re-epithelialization, dermal cell regeneration, and neovascularization. For print skin tissues and planar biomaterials on site, a handheld extrusion-based skin printer utilized fibrinogen, collagen, and hyaluronic acid in a dermal bioink fibroblasts and keratinocytes in an epidermal bioink [18]. In addition to delivering spatially organized biomaterials, tissues, and biohybrid structures, the system demonstrated the ability to deposit these materials onto compliant and inclined wound surfaces through operator-intervened delivery.

2.3.3 Ink Jetting

A drop-by-drop method of inkjet bioprinting is used to spray the bioink onto a substrate. A thermal or piezoelectric device drives the formation of bioink droplets. Thermal inkjet bioprinters are initially derived from commercially available desktop inkjet printers. These printers vary in spatial resolution, depending on their type, size, burst level, and temperature. In piezoelectric printers, pressure changes

occur within the cartridge as a result of acoustic waves or physical components that change size or shape. These changes force bioink through an output aperture. Because piezoelectric inkjet printers can control the size of bioink droplets, printing precision is generally excellent. The bioink viscosity during printing is the greatest limitation in developing bioprinting inkjet systems. Once the bioink has exited the print head, it must rapidly transition from a liquid state to a solid state in order to form a small droplet. This transformation can be achieved by causing crosslinking or gelation of the bioink chemically, enzymatically, physically, or something else. As a result, bioinks for inkjet bioprinting are constrained to a maximum viscosity. The printing speed of this method is relatively fast and offers a high degree of cell viability and low manufacturing costs. In contrast, this technique is unsuitable for printing high cell density or thick structures because of its limitations, such as possible damage to embedded cells caused by mechanical or thermal stress. An in-situ delivery of autologous dermal fibroblasts and epidermal keratinocytes was achieved using inkjet bioprinting and wound scanning imaging technology [19]. In layers tailored to the wound's depth and topography, fibrin/collagen hydrogel carried the cells and delivered them. Compared with current clinical cell spraying technologies, data showed increased re-epithelialization, reduced contraction, and extensive collagen fiber deposition, resulting in equivalent healing results.

2.4 Engineering Human Skin

2.4.1 Structure of Skin

The largest organ in humans is the skin, which forms the exterior surface through which the body interacts with the outside environment. This structurally complex tissue serves many functions for the body, which is crucial to protect the internal organs from the outside elements of the environment (Table 2-1). Moreover, skin helps regulate the body's internal temperature and also incorporates sensory elements that allow the feeling of the environment [31]. Functional skin features like hair follicles, sweat glands, vascularisation networks, and connective tissue form the entire tissue [32]. Structurally, skin consists of three layers with distinctive properties and functionalities. The outermost layer is called the 'Epidermis' and serves as the first barrier against outside substances. Water loss is responsible for creating the overall skin tone [31] [18]. The mechanical properties of the epidermis vary with the anatomical locations of the body [33] [34], with an approximate thickness of 95 μm and elastic modulus of 1.5 MPa [35]. The epidermis constitutes densely packed cells called Keratinocytes, which originate at the bottom of the layer 'stratum basale' and travel up to the outmost part 'stratum corneum. The major extracellular matrix material (ECM) components include keratin and collagen [36]. Under this, the layer of tissue that houses the connective tissue, nerves, sweat glands, and blood

vessels is called the 'Dermis.' Here, fibroblasts are abundant among other cell types like endothelial and Langerhans [36]. The dermal structure is provided through fibrous collagen, elastin, and proteoglycans-based ECM [37]. It is approximately 0.8 mm thick and has an elastic modulus of 0.02MPa. The next layer, 'Hypodermis,' consists mainly of blood vessels, nerves, and hair follicles. The dominant cell types include adipocytes, fibroblasts, endothelial, and smooth muscle cells. ECM support consists of collagen and elastin [36]. The thickness of the hypodermis is approximated to be 0.8 mm, and the elastic modulus is 0.002 MPa (ten times less than the dermis). Table 2-2 lists various mechanical properties of skin reported in the literature.

Layer	Thickness	Composition	Dominant Cell Type	Function
Epidermis	~95 µm, [18]	keratinized epithelium	keratinocytes, melanocytes, langerhans cells, merkel cells	A dense layer of keratinocytes at the outermost part of the skin inhibits bacteria from transmitting through the cell and causing water loss.
Dermis	1.4 mm, [18] 1.05 - 1.24 mm, [38] 1.094-1.033 mm, [39]	blood vessels, nerves, hair follicle	fibroblasts, endothelial cells, langerhans cells, hair follicle cell	It is primarily composed of fibroblasts, as well as a number of other cell types and an extracellular matrix that contains fibrous elastin 8.06 %, collagen 28.9 % [40]
Hypodermis	0.8 mm, [18] 1.1- 3.16 mm, [38]	blood vessels, nerves, hair follicle	fibroblasts, endothelial, smooth muscle cells	In addition to providing insulation, protecting the body, storing energy, regulating temperature, and connecting the skin to the bones and muscles, the subcutaneous layer also helps to regulate the body's temperature.

Table 2-1: Properties and composition and functions of different layers of skin tissue.

2.4.2 Design Driven In-Situ Constructive Modelling for an Ideal Skin Substitute

The goal for an ideal skin substitute extracellular matrix material is to replicate a microenvironment (biomimicry) that is facilitative of cellular regeneration processes like adhesion, proliferation, and differentiation.

2.4.2.1 Porosity

A high degree of an interconnected network of pores provides sites for cell attachments and allows for nutrient exchange and better tissue ingrowth [40] [41]. in vitro tissue engineering porosity, pore diameter, and wall thickness of the scaffold are important factors to consider when studying the biological behavior of the cell [40]. The implant's higher surface area to volume ratio will facilitate cellular migration and attachment. Pore size and shape play an integral role in influencing cellular

Name	Skin	Ref
Young's Modulus	250 kPa-140 MPa subject to anatomical location	[33]
	70 MPa (child), 60 MPa (adult)	[34]
	0.33 MPa (forehead) to 1.28 MPa (submandibular skin)	[44]
	2.9 MPa to 150 MPa	[45]
	19.5 MPa to 87.1 MPa	[46]
	88.3 MPa, back, indentation test, dynamic speed	[47]
	4.02 MPa abdomen, indentation test, quasistatic	[48]
	4.75 kPa - 17.99 kPa, forearm, in vivo laser displacement method	[39]
Tensile Strength	15.9 MPa @ 0.06 /s (quasistatic), 25.8 MPa @ 167/s (intermediate)	[49]
Strain at Break	1.17-3.07	[49]
	0.60-0.75	[34]
Stress Relaxation	4.74 MPa^{-07} (forearm), 7.8 MPa^{-07} (forehead)	[34]
Final Absolute Relaxation	0.01-0.04 MPa, forearm and submandibular	[34]
Viscosity Coefficient	dynamic viscosity 'μ' = 85.37 kinematic viscosity 'v' = 0.125 $Pa.s^n$	[50]
Storage Modulus G'	325 ± 93.7 Pa to 1227.9 ± 498.8 Pa	[50]
Loss Modulus G	68.5 ± 21.2 Pa to 189.9 ± 56.0 Pa	[50]
Porosity	200-400 um pore size, porosity, 68.53 ± 5.8%, mean pore diameter: 131.3 ± 96.8 um, wall thickness of pores 207.2 ± 251.7 um (acellular dermal matrix)	[43] [40]

Table 2-2: Mechanical, viscoelastic, and structural properties of native human skin tissue.

adhesion and migration to the implant structure [41]. The surface area is limited for binding proteins in materials with smaller pores. Materials with smaller pore sizes are shown to reduce capsule formation in vivo. Proteins can encounter steric hindrance at the material surface if the pores are too large. Conversely, a surface with large pores is able to bind proteins of any size if the pores are large enough. A popular choice of skin material, Collagen I's mineralization, and cellular organizations correlate with pore size [42]. For the advancement of in-situ skin regeneration, an ideal tissue construct should be highly porous with a network of interconnected pores between 200-400 μm [43].

2.4.2.2 Biodegradability

Once the implant tissue construct is printed in-situ, the cellular level interaction at the interacting surface starts regeneration, and the three-dimensional structure degrades. Understanding and controlling the biodegradability of the tissue is crucial to achieving a balance between the regeneration and degradation process [51]. The ingrowth of blood vessels, fibroblast, and epithelial cell proliferation needs at least three weeks to regenerate fully; hence, the printed tissue construct must maintain its structural integrity until after this period. For this, the biodegradability of the construct needs to be tuned accordingly [43]. Moreover, the degradation of biomaterial may induce unwanted foreign body responses. Therefore, the biodegradation of tissue construct at the native host tissue needs to be fully understood and controlled [52].

2.4.2.3 Crosslinking

Biomaterials such as crosslinked hydrogel are used as artificial ECM support to mimic the functionality of native skin. Chemically linking two or more molecules together through covalent bonds is called cross-linking. A crosslinking reagent is a molecule that contains two or more reacting ends that can attach chemically to a specific functional group on a protein or other molecule. By crosslinking, 3D bioprinting transforms polymer solutions into 3D structures. The cellular behavior of bio-printed constructs is significantly influenced by the crosslinking procedure, which plays a crucial role in the mechanical and physicochemical characteristics of the constructs [53]. A three-dimensional network is formed by crosslinking the active functional group of the polymeric chains with the crosslinking agent [54]. This reaction may be physically, chemically, or enzymatically driven, and the cross-linking method governs the mechanical and biochemical properties [55]. The resulting structure harbors cellular regeneration activities like adhesion, proliferation, and migration [54].

2.4.2.4 Surface Topography

There is a significant interest in how the surface topography of the implant influences cell-biomaterial interactions. The surface profile of the implant has been shown to modulate the blood-protein adsorption at the interface in the early healing phase [56]. It is difficult, however, to interpret the results of numerous studies due to an inadequacy of surface morphology characterization standards. In the case of surface fabrication, unintentionally creating confined spaces may lead to regions with structurally different behavior as a result of changes in the surface area resulting from changes in topography [56]. The effect of these unintended confined spaces on the host site's cellular response is

unclear. It is a challenge to quantify and compare this effect as the methods of fabrication and the resulting surface artifacts are different. Different surface roughness can, however, lead to differential protein adsorptions. The difference in surface textures of grooved silicone alters the deposition of serum fibronectin and vitronectin. Fibronectin deposition on surfaces of increasing roughness was also shown to increase with protein adsorption from single-protein buffers, though correction for surface area increases may reverse this effect. Although it is difficult to measure, altering surface topography may modulate protein adsorption, a factor that should be considered when designing biomaterial surfaces [57]. It is possible to modify the cellular response depending on the surface topography of an implant, which depends on the goal of an implant, such as increased adhesion and proliferation or prevention of foreign body response (FBR) for biological implants [58].

2.4.2.5 Implant Stiffness and Stability

Implant stiffness plays an integral role in inducing a specific lineage of cell type undergoing differentiation. Controlling the ECM stiffness offers the tendency to tune the terminal differentiation of human-derived mesenchymal stem (MSC) cells into a specific lineage [41] [59]. The stability and position of the implant with respect to the host site are essential in maintaining a non-inflammatory response. A stable implant provides direct contact between the mineralized host tissue and the interacting surface of the implant. An excessive interfacial micromotion of the implant also drives the immune response toward implant rejection. In dental implants, a stable separation between the implant and the host site of less than 100-200 μm enables healing responses dominated by the ingrowth of the bone and reduces fibrous scar formation [60]. Implant misfits may lead to increased compressive stress in bone, which can cause more interfacial microdamage and bone remodeling in the long term, even if there is improved stability at insertion [61].

2.4.2.6 Biocompatibility

The context of biocompatibility depends upon the type of biomaterials implanted and the healing response generated as a result. Non-degradable metallic implants that are free of endotoxins and toxic leaches will trigger a mild inflammatory response followed by the fibrous capsulation of the implant surface interacting with the host environment. The encapsulation is a life-long process that guides the host's cellular interactions with the implant. A non-degradable biomaterial free of endotoxin and toxic leeches and generates an adherent fibrous encapsulation is considered biocompatible [62]. For the constructive remodeling of the native host tissue, a nonfibrotic healing response is required. Engineering inert and biodegradable biomaterials can activate regulatory anti-inflammatory healing

responses characterized by the M2 phenotypic profile of the macrophages. The definition referring to biocompatibility in the case of in-situ bioprinting would be the ability of inert and biodegradable materials to trigger and guide the local microenvironment for wound healing, reconstruction, and tissue integration [62].

2.4.3 Natural Skin Regeneration Process

The regenerative cellular events occurring at the host site immediately following injury are improtant to understanding the native tissue's immunological response to an implant. Host response is activated with a multicity of events taking place at various timescales ranging from minutes to years. The human immune system has innate and adaptive components that initiate and guide the healing process at the host site [63]. The innate response process includes hemostasis (formation of the fibrin-platelet clot to slow further hemorrhage), inflammatory response (formation of granulation tissue), and fibrosis/fibrous encapsulation [64].

2.4.3.1 Immunological Response to Injury and Healing

Upon implantation of foreign material, the humoral and cellular components of blood surround the implant. Cellular collision, adsorption, and exchange processes lead to the formation of blood clots on the surface of a biomaterial due to the well-known Vroman effect, in which protein mobility and concentration are important factors in regulating blood protein adsorption early during the healing process (see Figure 2-2). The blood protein deposited on the implant's surface forms the provisional matrix. Bioactive molecules within the provisional matrix are released to orchestrate wound healing through natural, biodegradable, sustained release. In wound-healing, the provisional matrix is essential in providing structural and biochemical support. In vivo, our understanding of the regulating factors involved in the formation of the provisional matrix is less as most of the studies are conducted in in vitro settings [65]. More recently, interesting works have been published concerning the effect of engineered biomaterial in regulating an appropriate cellular response early in the healing process [65] [66] [67] [68].

Blood-material interaction with inflammation forms the early part of the host's response to injury. Acute inflammation lasts from minutes to days, depending on the nature of the injury. This process is related to the exudation of plasma protein and the migration of neutrophils. Neutrophils phagocytose (degrade and kill) foreign media by attaching and engulfment. Implants cannot be phagocytosed due to disparity in size, but other events, like the cellular release of leukocytes, may occur in an attempt to degrade the implant [65]. Consistent immunological stimulation leads to chronic inflammation and is

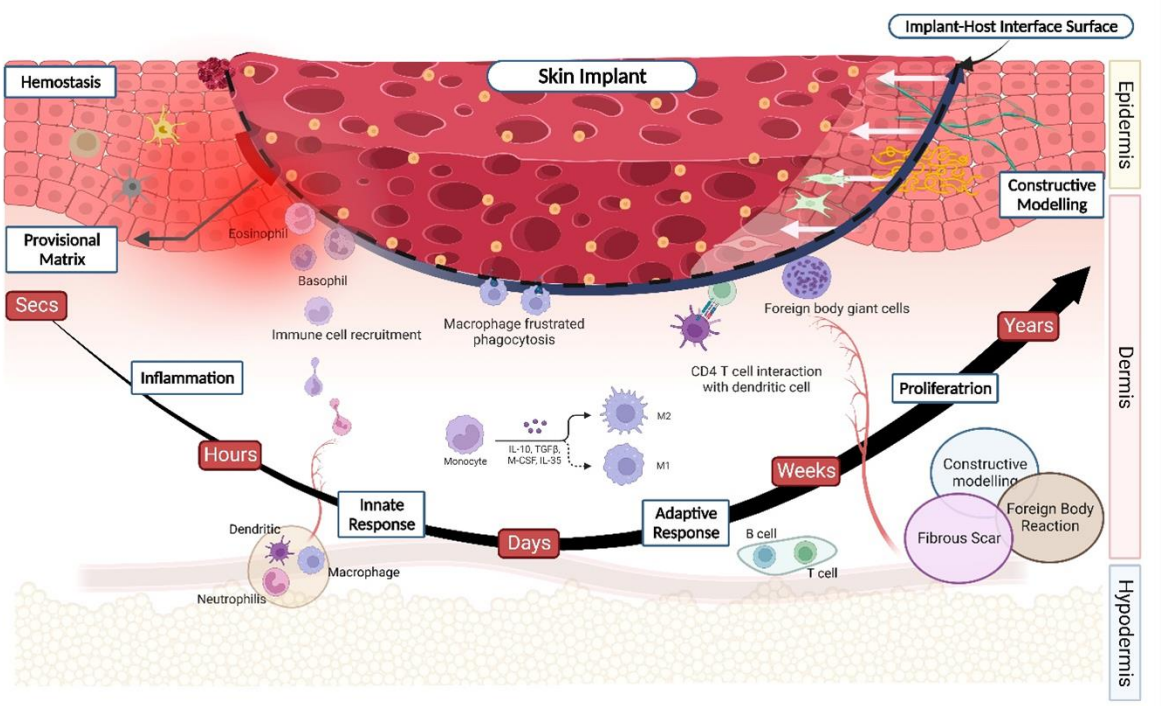

Figure 2-2: Cellular response of the body to implanted biomaterial on a timescale from the moment it is implanted to years after.

characterized by the abundance of macrophages, monocytes, and lymphocytes. Other factors that induce chronic inflammation include the biomaterial properties, in-situ motion of the implant, or the presence of infection.

Within 24 hours, the abundance of healing response composed of monocytes and macrophage activity, fibroblasts, and vascular endothelial cells are rapidly generated to start the granulation tissue formation. Overall, foreign body reaction is comprised of foreign-body giant cells and other granulation tissue components, e.g., macrophages, fibroblasts, and capillaries. The composition of the foreign response to the bio-implant depends on the form and topography of the implanted material. The biomaterial's surface properties, the implant's structure, and the relationship between the biomaterial's surface area and the implant's volume may affect the composition of the foreign-body reaction in the implant site [69]. In smooth-surface implants, macrophages and foreign-body giant cells are more prevalent than in implants with high surface-to-volume, such as fabrics, porous materials, particulate, and microspheres [70] [71]. The end stage of healing is the fibrous formation capsule around the implanted device which is regarded as a rejection phenomenon. In contrast, few biomedical devices require fibrosis to ensure implant stability and inadequate formation of fibrosis capsules may result in implant migration [65].

2.4.3.2 Regenerative Response in Skin Tissue

The innate system is (i) the first to respond to a danger signal, (ii) non-specific, and (iii) mediated by polymorphonuclear cells (such as neutrophils, basophils, and eosinophils), macrophages, and dendritic cells. Pathogens are killed by these cells, which then directs the adaptive immune system to respond specifically to the regeneration and healing challenges.

The adaptive part of the immune response to tissue repair comprises B and T cells. B cells target antigens for degradation by secreting antibodies. T cells can secrete cytokines that can affect innate and adaptive immune cells. T cells-directed immune response is activated when dendritic and macrophages are successfully bonded to the foreign media. Activated CD4 + helper T cells are known to regulate and guide the response to be either pro-inflammatory T_{h1} or anti-inflammatory T_{h2} immune polarisation profile [64]. Similarly, macrophages also initiate an adaptive immune response by activating toward a pro-inflammatory phenotype (M1) or regulatory anti-inflammatory (M2) phenotypic profile.

The two types of cells work in conjunction as macrophages receive cues early in the host response to promote polarization of T cells toward further T_{h1} or T_{h2}. An anti-inflammatory response promotes the constructive modeling/regeneration of the tissue.

Signals from the surrounding environment are incorporated into all the cells of the response system so that the response is acceptable to the local microenvironment [63]. Immune cells can form either fibrous connective tissue resembling the original host tissue or tissue similar to the original host tissue, depending on their phenotype, interactions with stem cells, and signals from the local microenvironment. As a result of unbalanced immune system activation, fibrosis or inflammation can occur [63]. Regenerative outcomes are significantly influenced by systemic immune profiles as well as local immunological profiles. There was a correlation between slower or faster surgical recovery at the systemic stage when specific blood immune signatures are present. For example, there was a negative correlation between bone repair and differentiated $CD8^{+}$T cells [72], but macrophages, T cells, and B cells correlated positively with bone repair [73].

In summary, as a result of applying a biomaterial to a traumatic wound or injury site, the number and type of immune cells that migrate to the site will increase. These immune cells are recruited based on the material's position in the tissue, the type of trauma, and the biomaterial's natural and physical properties. The addition of an implant to the surrounding host tissue creates an immune

microenvironment that induces phenotypic polarization, activation, and secretion of cytokines associated with different phenotypes. An implant's ability to recruit and/or differentiate stem and progenitor cells ultimately determines the success of one regenerative process.

In summary, it is necessary that materials reflect these above-mentioned needs and instantiate an immune response appropriate for the target site, as the response appropriate for skin healing and regeneration may differ from that of ocular tissue or muscle regeneration [74]. This is referred to as biomaterial-directed regenerative immunology [63].

2.4.4 Host Response to Biomaterials

For tissue regeneration to occur, biomaterials should match both the mechanical and biochemical properties of the native skin tissue. Biological cues, such as proteins from the ECM, bioactive peptides, and cytokines, are crucial to triggering cellular responses and attracting a host response. Providing the appropriate cues to control cell behavior requires matching the mechanical properties of native tissue. Mechanical mismatches between the tissue and biomaterial can result in mechanical failure, inflammation, tissue damage, and a loss of interfacial contact between the implant and the surrounding tissues.

For in-situ bioengineering of regenerative skin applications, ECM proteins and naturally occurring materials, such as hyaluronic acid, alginates, and chitosan, can provide several advantages in terms of biocompatibility since they are recognized by the surrounding biological environment and metabolically processed by it. Unlike many synthetic materials, naturally derived materials can be enzymatically or hydrolytically degraded by the host, facilitating their removal and integration. However, it should be noted that some synthetic materials are designed to be biodegradable and can be engineered to degrade at controlled rates suitable for tissue regeneration.

It has been noted that immunogenic reactions have been observed following the implantation of ECM proteins derived from animals and natural materials. Despite being similar to the host's endogenous ECM, implanted materials may contain antigenic determinants that are not present in the endogenous material. This issue is mainly common among animal-based ECM proteins. The immunogenic effect can be reduced by chemically modifying the ECM material or sourcing it from another source.

Changing natural materials' mechanical properties, such as their elasticity and tensile strength, by chemical modification and crosslinking is a common method of modifying their mechanical properties.

However, it is more difficult to modify natural materials because of their complex structures than synthetic polymers.

2.4.4.1 Collagen

Collagen is abundantly present in the ECM network of the human connective tissues, accounting for 70-80 % of the dermis by weight. It is a naturally sourced material synthesized through cell culture [75]. At least 28 different types of collagen have been identified, consisting of 46 distinct polypeptide chains, with collagen Type I being the most widely studied [76]. Collagen has a triple helical structure with repeated $[Gly\text{-}X\text{-}Y]_n$ sequence, where X and Y mostly frequently consist of amino acids, (2*S*)-proline (Pro,28%) and (2*S*,4*R*)-4-hydroxyproline (Hyp, 38%) [77] [78] [76]. Due to its high degree of biocompatibility, non-cytotoxicity, and support for cell growth, it is extensively used as a scaffold material in tissue engineering applications [23]. Cellular support is provided through its cell-adhesion peptides, serving as a signaling molecule [79]. Collagen is low in viscosity, has low strength, has poor structural stability, and degrades rapidly, making it difficult to adopt in bioprinting applications [23].

2.4.4.2 Gelatin

Gelatin is a natural protein-based biocompatible and biodegradable material produced through the hydrolysis of collagen [23]. The triple helical molecular structure of gelatin contains repeating units of glycine-proline/hydroxyproline-proline/hydroxyproline triplets [80]. Cellular support abilities of collagen-like (RGD) adhesion and (MMP-cleavable) degradation motifs are retained in the synthesis of gelatin. Gelatin is more biocompatible than collagennd has a lower risk of foreign body reaction or infection [81]. Gelatin demonstrates thermo-responsive behavior and undergoes gelation in an aqueous solution at a concentration higher than 2 -3 wt%. At lower temperatures, it exists as a gel with its oligomers intertwined in a triple-helix form and transitions to a solution state at higher temperatures ($T_g \sim 30^o$ C) [82]. Due to the ease of processing and the ability to modify, gelatin has been rapidly employed for skin bioprinting applications. Gelatin is extensively used in existing biomedical applications like wound dressing, surgical adhesive, and scaffold material [80].

2.4.4.3 Fibrinogen/Fibrin

Blood fibrinogen is made up of glycoproteins synthesized by the liver [83]. Fibrinogen is a precursor of fibrin and a part of the natural provisional matrix (clotting, the body's first response to injury healing). During the healing process, fibrinogen polymerizes together with platelets and contributes to clotting.

A fibrin matrix is formed when soluble fibrinogen is polymerized by thrombin, which is also produced by the liver [84]. Polymerized fibrin is a biodegradable matrix broken down in vivo by plasmin, a proteolytic enzyme. A patient's blood can be used to generate autologous implants for tissue engineering applications, reducing the risk of foreign body reaction since fibrinogen can be isolated from animal plasma as well as human plasma. Fibrin is excellent in activating cellular interaction through the natural presence of sites for cellular adhesion, ECM attachment, and growth factor binding [75]. A number of natural and synthetic polymers, including collagen, have been combined to enhance the mechanical strength of fibrin hydrogels [85].

2.4.4.4 dECM

Decellularized extracellular matrix-based hydrogel has recently gained a great deal of attention from the research community. Although the variation in the extraction process and a great batch-to-batch variation are major drawbacks, natural cellular signaling and attachment abilities make dECM an attractive choice for development into inks for bioprinting applications [86]. dECM retains significant bioactivity when implanted in-situ and stimulates endogenous stem/progenitor cell differentiation and immune response modulation [28]. One of the major advantages of dECM hydrogels is their capacity to target specific organs. Compared to decellularized cartilage, skin dECM may contain specific proteins and signaling factors that stimulate stem cell differentiation. In addition to its bioactivity, the resulting hydrogel's mechanical properties and printability can be affected by the variability in structural protein content caused by processing and source (age and organ) [87].

2.4.4.5 Chitosan

Chitosan is a natural polysaccharide consisting of D-glucosamine and N-acetyl-D-glucosamine repeating units. It is obtained from the deacetylation of chitin extracted from exoskeletons of crustaceans, e.g., shrimps, crabs, and fungal cell walls [88] [89] [90]. Intraperitoneal implantation of porous tubular chitosan is known to promote significant neutrophil migration in mice after one week [91]. Chitosan is a biocompatible and biodegradable material and is extensively employed in drug delivery and wound healing applications [84]. The immune response to chitosan depends upon the degree of deacetylation of the alkaline hydrolysis of chitin [92]. Chitosan with a low molecular weight (3 kDa) is associated with a pro-inflammatory response as compared to chitosan with a high molecular weight (50 kDa) [93]. Several types of chitosan hydrogels are available. These include network structures, ionic crosslinks, and polyelectrolyte complexes [94] [95]. Human enzymes such as

lysozyme break down chitosan, making it biodegradable. The type and density of the cross-linker and the hydrogel network affect degradation rates [96].

2.4.4.6 Alginate

Alginate is a naturally occurring anionic polymer obtained from brown seaweed. In alginate, mannuronic acid (M) and guluronic acid (G) are repeated in irregular blocks with varying ratios of MM, GG, and MG [97]. [Alginates range in molecular weight from 50kDa to 100,000kDa. The crosslinking of alginate hydrogels can be accomplished in a variety of ways. It is common to use divalent cations (Ca2+ or Ba2+) to form ionic bonds between neighboring strands to form chain associations. Alternatively, poly(guluronate) can be partially oxidized, followed by an adipic dihydrazide reaction to form covalent crosslinks with alginate. As a third crosslinking strategy, polyethylene glycol diamines are used to link alginate chains covalently. With varying compositions and crosslinking methods, gel stiffness and elasticity vary. Alginate gels can be tuned mechanically by tuning the M:G ratio, crosslinking method, and molecular weight [84]. Because alginate is relatively inert, easy to access, and gels well when divalent ions such as Ca are present, it has been extensively studied for many biomedical applications, including drug/protein delivery, tissue engineering, cell/microorganism immobilization, and food processing [98].

2.4.4.7 Hyaluronic Acid

Hyaluronic acid or hyaluronan is another naturally occurring linear polysaccharide consisting of N-acetyl glucosamine and D-glucuronic acid. It is abundantly present in mammalian ECM components of all types of tissues, particularly connective and epithelial tissues. As a result of HA's protein binding capacity, it causes inflammation by binding to the surface receptors on inflammatory cells, particularly CD44 and Toll-like receptors. However, the level of inflammation will vary depending on HA's molecular weight [99] [100]. There is evidence that low molecular weight HA causes pro-inflammatory responses, whereas high molecular weight HA inhibits inflammation [101]. The FDA has approved hyaluronic acid for its use in cosmetic and wound healing applications [102].

2.4.4.8 Gelatin Methacryloyl (GelMa)

GelMA transforms into its crosslinked form via physical, chemical, or enzymatic crosslinking techniques. Typically, physical crosslinking is facilitated by exposing GelMA to UV light in the presence of a photo-initiator, such as 1-[4-(2-hydroxyethoxy)-phenyl]-2-hydroxy-2-methyl-1-propan-1-one (Irgacure) [103] [104]. Given the concerns regarding UV radiation's potential adverse effects on

living cells, researchers have sought alternative crosslinking methods. One notable strategy employs the Eosin-Y system, which facilitates crosslinking using visible light around 500 nm [105] [106]. The inclusion of different photo-initiators invariably influences GelMA's rheological and mechanical attributes. For instance, when crosslinked with visible light agents like ruthenium and sodium persulfate, GelMA's physical and mechanical properties align closely with those obtained through UV agents such as Irgacure 2959 and lithium phenyl(2,4,6-trimethylbenzoyl) phosphinate (LAP) [107]. On the enzymatic front, systems like microbial transglutaminase (MTGase) can heighten the gel's viscosity and stabilize it rapidly [108]. It is evident that the choice of photoinitiator significantly impacts the final gel's mechanical and biological properties [109] [110]. Therefore, a comprehensive hydrogel characterization, specific to the photo-initiator employed, is of paramount importance [111].

Various additives, such as hyaluronic acid-methacrylamide [112] [113], poly(ethylene glycol) diacrylate, [114], bacterial cellulose [115] [116], and carbon nanotubes [117] [118], are incorporated into GelMA to adjust its properties. Another additive that shows promise in enhancing the mechanical and rheological properties of GelMA hydrogels is Cellulose Nanofibrils [116]. CNF, derived from renewable sources like cellulose, possesses unique properties, including high aspect ratio, mechanical reinforcement, and biocompatibility. By introducing CNF, the mechanical properties of GelMA hydrogels can undergo pronounced alterations, making them either more compliant or more rigid [116]. This intrinsic tunability is especially vital for bioprinting applications, where material properties can significantly impact the final product's integrity and functionality [116]. For instance, in a study conducted on GelMA/CNF printed scaffolds, cell cultures with 3T3 fibroblasts demonstrated non-cytotoxic and biocompatible features for the formulated inks [119]. This research successfully printed 3D scaffolds using low-concentration inks formulated by 1 w/v % 2,2,6,6-tetramethylpiperidine-1-oxyl radical (TEMPO)-oxidized CNF in addition to less than 1 w/v % of GelMA. Further exploring the capabilities of these bioinks, another investigation delved into formulations based on GelMA combined with oxidized cellulose nanofibrils [120]. The study provided an encompassing look at these formulations' printing performance, morphological, swelling, and biological properties. The results underscored that GelMA, which retains the cell-adherent motifs of collagen, can produce printable formulations with favorable attributes when combined with CNF. These characteristics make CNF an attractive candidate for improving the suitability of GelMA hydrogels for bioprinting applications. A comprehensive characterization of their preparation method and properties is necessary to explore the potential of GelMA-CNF hydrogels for bioprinting purposes further.

The rheological attributes inherently reflect the bulk properties of materials, profoundly influencing their flow behaviors during printing [121]. This determines the material's appropriateness for specific applications and provides insights into intrinsic properties, which can affect cellular adhesion and immune responses. These insights are invaluable, serving as foundational guidelines for creating and assessing new materials. Therefore, an in-depth mechanical assessment, complemented by a thorough analysis of outcomes, is required. A critical determinant of GelMA properties is the sol-gel transition temperature, particularly in the context of uncrosslinked GelMA. Recent research highlights the consequential roles of crosslinking temperature and heating-cooling rates in influencing this transition [122]. The study reports the pronounced impact of the cooling rate on the transition temperature. Such knowledge is pivotal for understanding GelMA's behavior, especially for applications demanding precise transition temperatures.

2.4.5 Current Approaches for Wound Healing

2.4.5.1 Skin Grafting

Autologous grafting is a widely used approach for treating acute cutaneous wounds caused by trauma or burn. It involves the ablation of necrotic tissue followed by grafting skin from a healthy donor site to treat large areas of the wound and restore the skin’s ability to act as a barrier. However, the healed tissue suffers from significant contraction and unorganized tissue remodeling, resulting in the appearance of a fibrous scar, no feeling of sensation and elasticity, and inconsistent aesthetic features [123] [124] [125]. Moreover, having insufficient harvestable skin is also a limitation when a patient's wounds exceed 60% of their body surface area. This means that autografts cannot adequately cover the injury in these cases, and a temporary dressing may be required before autografts can be applied [126] [127]. Meshing autografts increase the treatable surface area up to 4 times and have been shown to improve the survival rate of burn patients. On the other hand, it results in poor healing and creates visible scarring. Some other limitations include high cost, the high wait time to culture, and the possibility of catching an infection [128] [129]. Cell-sprayed autografts can also be used to treat deep partial-thickness burns. Even though re-epithelialization is improved by this method, uneven distribution may result, and eventually, viable cells may be lost [130]. Despite being considered the gold standard for wound management, skin grafting has one of its significant weaknesses: insufficient access to healthy donor tissue.

Skin grafting with split-thickness has proven safe and effective for treating burns, wounds, and other skin injuries when simpler methods like primary closure or negative pressure therapy are not sufficient

to close the wound. It is a well-established technique that does not require special equipment or materials, making it a cost-effective solution that a surgeon performs. Skin grafting can be performed quickly, particularly for small wounds, compared to in-situ bioprinting, a more complex procedure that can take longer time to plan. Split-thickness skin grafting is appropriate for wounds that need immediate coverage, such as those with well-defined edges and a well-vascularized (healthy) wound bed that can support graft in-growth. Mechanically demanding body areas, such as hands and joints, are commonly treated with thicker or full-thickness skin grafts, as thinner split-thickness grafts are susceptible to failure under high force and repetitive motion. Harvesting full-thickness graft involves the removal of the epidermis and dermis from the donor site and thus requires primary closure. Thicker grafts are more metabolically active and are avoided when treating wound beds with a restricted supply of nutrients, oxygen, and damaged vascular network. The final cosmetic outcome may be influenced by several factors, including the wound's location, the graft's thickness, and the quality of the patient's skin. The option of skin grafting is available immediately following the onset of injury, whereas in-situ bioprinting requires time for cellular culture and planning the procedure. Skin grafting procedures can result in rapid wound closure, reduced scarring, and favorable cosmetic outcomes in the right circumstances.

2.4.5.2 Engineered Skin Substitutes

Skin substitutes are engineered scaffolds that are used to facilitate the regeneration process of the dermal elements when applied to trauma or induced wounds. Dermal substitutes resembling the stratified layers of skin apply pressure on the wound to stabilize hemorrhage and maintain stability [131]. Naturally occurring materials (collagen, fibrin, keratin), which are already a part of skin ECM, are favored for the development of dermal scaffold due to the presence of protein motifs that facilitate cellular attachment [132]. For example, MatriDerm (MedSkin Solutions), composed of highly porous elastin membrane and collagen from bovine, can be used to treat full-thickness lesions [133]. Scaffolds are also developed from synthetic materials; for example, Biobrane-L (Bertek Pharmaceuticals) consists of flexible nylon fabric attached to a thin layer of porous silicon [134]. As a substitute for skin, scaffolds can be delivered separately or in combination with keratinocytes and fibroblasts in order to simulate the dermis and epidermis, respectively. Fibroblasts are populated inside a polymer matrix such as gelatin to deliver cell-laden skin substitutes, followed by seeding a layer of keratinocytes on top [135]. The cells proliferate and keratinize to form stratified layers of skin through the introduction of growth media and an air-liquid interface [136]. The resulting engineered scaffolds are employed widely for cells-based in vitro studies to study immunoreactivity [137], epithelialization [138] [139],

[140], and wound closure [141] for first and second-degree burn injuries. A few examples of commercially available bi-layered (epidermal/dermal) scaffolds include Orcel [134] and Apligraf [142], which consist of bovine collagen ECM seeded with allogenic fibroblasts and keratinocytes. Moreover, their application for the regeneration of the hypodermis layer has not been fully addressed and carries immense potential. Various techniques used to fabricate engineered skin substitutes include freeze-drying [140] [143], crosslinking [138], knitting [144], and electrospinning [145]. While engineered skin scaffolds have demonstrated some degree of re-epithelialization when applied to recapitulate the epidermis and dermis [134], they result in visible scarring.

Regardless of their usefulness for addressing specific properties of native skin tissue, these models neglect the complex physiology of the skin in order to focus on a singular goal [48]. Currently, it is not possible to recreate the complex hierarchical structure of native skin with hair follicles, pigment, and vessels [146]. Cell delivery is not spatiotemporally controlled to form layered structures mimicking skin [147]. 3D printing has been investigated for clinical applications to understand and provide regenerated functional skin. As a 3D bioprinting option, it can be used to mimic physical microenvironments for optimal cell behavior by spatially controlling material and cell deposition.

2.5 In-Situ Bioprinting Techniques for Skin

Works done to date concerning in-situ bioprinting of skin can be categorized into two groups depending on the method of delivery. The skin-type biomaterial is either deposited through a robotic or a handled device, as illustrated in Figure 2-3. Types of material deposition technology may vary within each of these categories, for example, inkjet, spray, etc. A summary of related works is presented in Table 2-3.

2.5.1 Robotic Approach

In the robotic approach, commercially available three degrees of freedom desktop 3D printers are used as the control mechanism for material delivery. The deposition nozzle has a maximum of 3 degrees of freedom and requires a controlled or stationary platform on which the target host is located. The overall printing procedure includes the realization of the CAD model through scanning setup and slicing the implant model through a slicer to generate printing instructions. The idea to use a 3D printing device for the spatial arrangement of extracellular material and cells for skin wound treatment in-situ originated in 2010 [21] [22]. A bioprinting device consists of 8 cartridges based on a desktop planar printing framework and is integrated with a scanning system. Printing on the full-thickness murine wound model (3 x 2.5 cm) is carried out with bioink consisting of 10 million fibroblasts for the dermal layer and 10 million keratinocytes for the epidermal layer. Thrombin is sprayed simultaneously through

an atomizing nozzle to form fibrin/collagen hydrogel. Results of the preclinical study conducted on the porcine model showed the presence of marked keratinocytes and fibroblasts at week 8, signifying the survival and proliferation of the cells to form skin tissue. Autologous keratinocytes and fibroblasts proved to be superior in healing by achieving full epithelization at week 8.

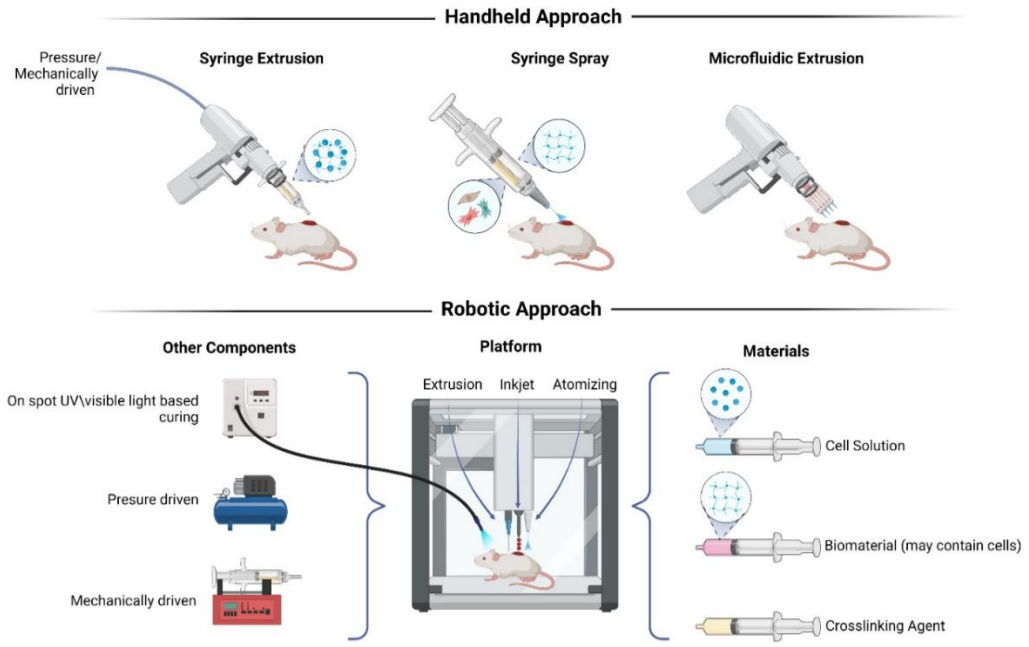

Figure 2-3: Overview of the two approaches to in-situ bioprinting of skin. Handheld approach and robotic approach.

In 2019, a proof of validation concept for a skin bioprinter incorporating allogenic and autologous skin cells embedded in a fibrinogen and collagen matrix was presented [19]. The biomaterial delivery system comprises a nozzle simultaneously atomizing thrombin that mediates the catalyzed coagulation of fibrin monomer from fibrinogen. Autologous and allogeneic epidermal keratinocytes and dermal fibroblasts are loaded in a cartridge-based delivery system. The system overall provides a deposition resolution of 260 µm and a motion resolution of 100 µm. Moreover, the addition of a scanning system allows for an accurate depiction of the implant to be fabricated. In murine models, 500 cells/droplets are delivered to a full-thickness excisional wound area measuring 3 x 2.5 cm. The presence of cells accelerated skin healing in-situ, and at week two, the total wound area was observed to be reduced by 15% of the original size. At week 3, a well-defined epidermis and assembled dermis embodying aligned collagen fibers are witnessed. In the porcine model, a 10 x 10 cm full-thickness wound model is delivered with biomaterial containing allogenic and autologous skin cells. The efficacy of the adopted technique is also compared with the spraying of biomaterial/cells. By week two, the wound site treated

with autologous keratinocytes and fibroblasts showed full recovery of wound area as compared to allogeneic and matrix-only treated wounds. Wounds treated with autologous cells exhibited mild inflammatory response, an early appearance of a mature vascularisation network (by week 8), and an organized arrangement of collagen fibers. In comparison to the spraying technique, the formation of the epidermis was not witnessed until week 4. In contrast, bioprinter-treated wounds showed early epithelialization with complete coverage of the wound as early as week 2.

Human skin cells like keratinocytes suffer from challenges related to sourcing and rejection [148]. Stem-cell-based therapies have shown considerable potential for improving the quality and rate of wound healing [149]. The use of autologous and allogenic amniotic-derived stem cells (AFS) and mesenchymal stem cells (MSCs) have also been explored for the application of skin printing [86]. A print head composed of pressure-driven nozzles is used to deliver a solution of fibrinogen and collagen with or without cells. Thrombin as a crosslinking agent is delivered through a separate secondary high-pressure nozzle. A sequence of hydrogel/cell and thrombin layers are printed on a single-thickness wound surgically created on a mid-dorsal region of a murine model. Results showed both MSCs and AFS were equally effective in wound healing and re-epithelization rates. However, AFS proved to be more effective in inducing a stronger, more mature, and more stable angiogenic response.

2.5.2 Hand-held Approach

The handheld approach is an alternative to robotic control for the spatial arrangement of biomaterial and cells in a wound-affected area. In 2018, a proof-of-concept study demonstrated the healing of full-thickness wounds in murine and porcine models through the microfluidic extrusion of biomaterial and cells [18]. The lightweight and portable device consisted of microfabricated cartridges delivering an epidermal layer composed of fibrinogen and hyaluronic acid and human keratinocytes and a dermal layer composed of fibrinogen/hyaluronic acid/alginate/collagen with human fibroblasts. Fibrinogen-based layers are deposited with thrombin to form fibrin-base clots immediately. The collagen/alginate-based layer is delivered with calcium chloride as the crosslinking agent. Porcine models showed a complete re-epithelization of the wound (2 cm x 4 cm) on day 20 when treated with a 0.3 mm thick fibrin/hyaluronic layer.

Another example of handheld-based treatment includes recent work incorporating multi-potent mesenchymal stem cells (MSCs) to treat a full-thickness burn wound [150]. The device is compact and lightweight (1.4 kg), with motor-driven microfluidic cartridges delivering cell-laden fibrinogen and hyaluronic sheets. Thrombin is used as a crosslinking agent. The in-situ delivery of a 0.2 mm thick

biomaterial layer was carried out on a porcine model on a 5 x 5 cm full-thickness wound. The MSCs/biomaterial-treated wound showed an accelerated epithelization rate and superior epidermal thickness and collagen fibers regeneration on day 28. MSC treatment also showed a high number of CD31+ endothelial cells, signaling the formation of a vascularization network. Another work concerned with in-situ bioprinting of skin implants includes a handheld device integrating spray, extrusion, and electrospinning as a method for material deposition [20]. In this work, the demonstration of this handheld device was carried out on a non-biological PDMS mold. In this multi-method printing, PEGAD is used for spraying, PCL for electrospinning, and gelatin/sodium alginate is based on treatment through extrusion. From a technological readiness perspective, the applicability of this technology is limited as of right now. The processing of materials includes components that are not biocompatible, for example, the dissolution of PCL in DCM, which is known to cause irritation and skin burns. Another concern is the high working voltage that is used for the electrospinning process and the use of UV light and its effect on cellular activity.

Well before the method of bioprinting in-situ was introduced to the tissue engineering community, investigations were made into the cell-based therapy for burn wounds through the delivery of skin cells onto the affected areas via spray [151], syringe [152] or a pressurized nozzle [153]. Some of the earlier methods related to in-situ delivery of biomaterial for wound healing applications are worth mentioning, and the methodologies can be categorized based on the instrument of delivery, namely, a syringe or spray. For example, treating deep dermal wounds covering 5% of a male body through syringe-based delivery of keratinocytes in a ringer lactate solution saw complete re-epithelization with no signs of inflammation [154]. In another example, a 1.0 x 10^6 cells/ml suspension of non-cultured keratinocytes was delivered to 8 patients with a mean treatment area of 3% of the body through a pneumatically controlled syringe spray. On days 12-13, full re-epithelization of the deep dermal burn wounds was observed in all patients [152]. Other noteworthy examples include the application of keratinocytes [155] [156] and mesenchymal [157] cellular solution with no matrix material on humans [155] and porcine [158] [159] [160] model for the treatment of mild to severe burn wound on the skin. Another mechanism for in-situ hand-held delivery of cells and biomaterials is through a pneumatic or hand-driven spray pump. Hand spray has been successfully used to deliver cultured [161] [162] [163] and non-cultured [151] keratinocytes and mesenchymal stem cells [164] with or without fibrin for the treatment of burn wounds in human [153] and animal models [161].

Method	Year	Biomaterial	Cell Type	Crosslinking	Deposition Method	Model	Wound Site	Ref
Bioprinter	2019	fibrinogen & collagen	autologous and allogenic keratinocytes & fibroblasts	enzymatic-thrombin	pressurized cartridge and atomizing nozzle	porcine and mouse	10 x 10 cm (porcine), 3x 2.5 cm (mouse)	[19]
Bioprinter (Handheld)	2018	epidermis: fibrinogen. hyaluronic acid; dermis : fibrinogen, hyaluronic acid alginate in collagen-I mixture	human fibroblast and keratinocytes	enzymatic-thrombin	microfluidic extrusion	porcine and murine	2 x 4 cm	[18]
Bioprinter	2012	collagen and fibrinogen mixed 1:1	AFS and MSCs	enzymatic-thrombin	Inkjet, Pressure Driven Cartridge and Nozzle	mid dorsal region of mice	2.0 cm x 20 cm (full thickness)	[148]
Bioprinter	2011	Fibrinogen & collagen	human keratinocytes and fibroblasts	enzymatic-thrombin	Inkjet for biomaterial& atomizing nozzle for thrombin	mice	3 x 2.5 cm (full thickness)	[22]
Bioprinter (Handheld)	2021	spray: PEGDA, electrospinning: PCL, extrusion gelatin + sodium alginate	NA	chemical and UV (5sec @ 365 nm)	spray, extrusion & electrospinning	non-biological (PDMS mold)	2.5x2.5 cm (3mm thick)	[20]

Bioprinter (Handheld)	2020	fibrinogen & hyaluronic acid	mesenchymal stem/stromal cells (MSCs)	enzymatic-thrombin	motor driven microfluidic cartridges	porcine	5x5 cm full thickness (Each deposited sheet is 0.2 mm in thickness)	[150]
Cell Based (Handheld)	2000	-	autologous keratinocytes	-	cellular solution in syringe	porcine	dorsum, 9 x 9 cm	[158]
Cell Based (Handheld)	2001	-	highly pigmented and non pigmented skin cells	-	cellular solution in syringe with spray nozzle	porcine	16 full thickness, dorsum, 3 x 3 cm	[159]
Cell Based (Handheld)	2001	-	cultured and non cultured keratinocytes	-	cellular solution in syringe with spray nozzle	porcine	87 full thickness wounds, 1.5 x 1.5 cm	[160]
Cell Based (Handheld)	2006	-	cultured autologous keratinocytes	-	cellular solution in syringe with spray nozzle	human	19 patients, deep dermal burn wounds	[155]
Cell Based (Handheld)	2011	-	non-cultured autologous keratinocytes	-	syringe with cell in Ringer's lactate solution	human	male. 43 years, deep dermal burn wound on elbow and arm measuring 5% of total body area	[154]
Cell Based (Handheld)	2011	-	non-cultured autologous keratinocytes	-	syringe with cell in Ringer's lactate solution	human	8 patients, mean age 30.3 years, mean treatment area 3% of body,	[152]

							partial thickness burn injuries at different anatomical locations.	
Cell Based (Handheld)	2017	fibrin (Vivostat® system)	non cultured autologous keratinocytes (ReCell system)	enzymatic	hand spray	human	29 year old, female, 25% of body area covered with burn wound(torso, abdomen, forearm, back, shoulder, legs)	[151]
Cell Based (Handheld)	2010	human fibrinogen (Tissel VH kit)	cultured autologous mesenchymal stem cells (MSC)	enzymatic-thrombin	pressurized spray consisting of a hand grip and nozzle	human	10 patients, mean age 46.1 years, mean treated area 2.05% of body, deep dermal burn wounds in leg. hand and chest	[153]
Cell Based (Handheld)	2007	human fibrinogen (Tissel VH kit)	keratinocytes	enzymatic-thrombin	spray system with a double barrelled syringe (Tissomat spray set)	human and murine model	1 x 1.5 cm full thickness wound (mice). human: 5 acute wound and 8 chronic non healing wound	[164]

Cell Based (Handheld)	2002	fibrin	cultured autologous keratinocytes	enzymatic-thrombin	pressurized spray (Vivosat®)	porcine	12 full thickness wounds	[161]
Cell Based (Handheld)	2003	fibrin (Tissel VH kit)	cultured autologous keratinocytes	enzymatic-thrombin	syringe with a spray nozzle	porcine	3 pigs, 18 full thickness wounds	[156]
Cell Based (Handheld)	2016	-	non-cultured autologous mesenchymal stem cells (MSC)	-	30 G needle with pressurized delivery (SkinGun, Renova Care, Inc.)	human	18-43 age, location: all over body	[157]
Cell Spray and Autograft	2015	fibrin	cultured autologous keratinocytes (Keraheal®)	enzymatic-thrombin	sheet and spray type application	human	all over body, severe burn wound	[162]
Cell Based (Handheld)	2012	-	cultured autologous keratinocytes	-	Tissomat® cell spray	human	16 burn patients, full thickness burn, all over body,51.3% burned area	[163]

Table 2-3: Review of works concerned with in-situ bioprinting/deposition of skin.

2.6 Slicing Strategies and Software Solutions

There are four fundamental steps to printing engineered tissue using bioprinting: modeling, slicing, printing, and quality control. Modeling is creating a digital 3D representation of tissue using computer-aided design software (CAD) [165]. When an in-situ approach is used, a surface scan of the target location will design the implant geometry. Implants are typically generated by subtracting the target model's geometry from the healthy model. A CAD model is exported as an STL model to slice an object, which most slicer applications accept. An STL (stereolithography tessellation language) representation is a collection of triangles representing an object's exterior surface boundary [166]. The STL model is sliced into thin layers (slices), typically around 0.05-0.3 mm thick during the slicing process. A slicer converts a 3D model of an object into a series of 2D cross-sectional layers. The toolpath is generated on each slice with a specific linewidth, layer height, and percentage infill. In the printing step, 3D printers build objects layer by layer using the sliced model sent to them as instructions. Following the instructions provided by the slicing software, the printer deposits material in a precise pattern. Lastly, the quality and accuracy of the printed object are tested. Measurements, checks for defects, and comparisons with the original design may be involved. In in-situ skin printing, the options for any post-processing are not available, and the quality control capability is limited as the implant is made to work on the wound. The current 3D in vitro printing technology is based on the following principles: (i) the printing workflow is based on planar slicing, and (ii) it prints on a flat surface [167]. These working conditions result in certain limitations due to planar deposition [168]. 3D structures are produced using planar slicing in bioprinting. The final 3D product is constructed by stacking 2D planar slices or layers of the desired 3D structure on top of one another. Printing a skin implant in-situ where the printing surface is not flat is not feasible when utilizing 3D printing technology built around planar slicing and designed to build on a flat surface due to issues like the stair casing effect [168].

2.6.1 Traditional vs. Advanced Slicing Techniques

Traditionally, sliced layers are deposited flat or planar in printing, which can weaken or delaminate layers under directional loads, such as tensile stress [169]. Moreover, converting the 3D model section to 2D layers results in a geometric loss and produces the well-known stair-casing effect [168]. Stair-casing can also be described as the stepwise representation of a sloped surface (as illustrated in Figure 2-4). Additionally, the printed fiber layup arrangement is known to affect the mechanical integrity of the object [170] [171]. The use of adaptive slicing can reduce the stair-casing effect of planar printing by creating non-uniform build layers by adjusting the layer thickness according to the shape of the object being printed [172] [173] [174]. Another strategy to reduce the effects of planar printing is to

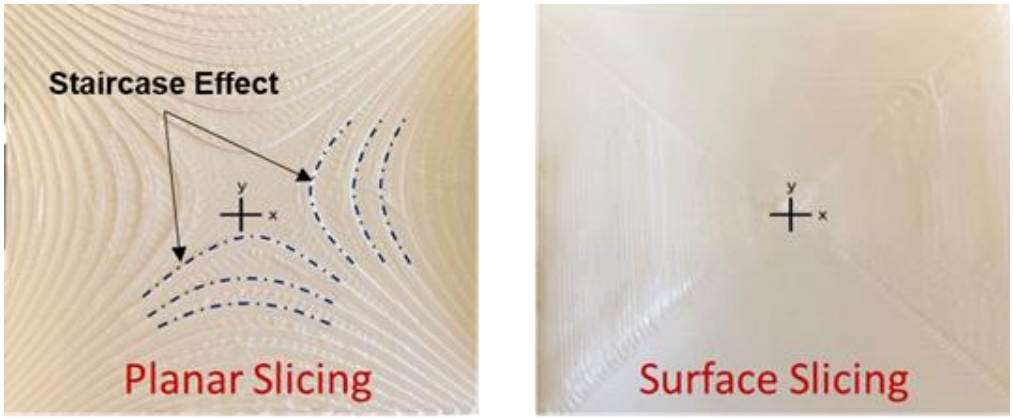

Figure 2-4: Illustration of the staircase effect in the planar printing process. Free-form surface slicing avoids staircases and produces smooth and geometrically accurate surface profiles.

slice the object with multi-directional tool paths, dividing it into different regions printed in different orientations [175] [176]. Another approach employed in fabricating complex structures in 3D printing is the multi-directional slicing method for conformal printing. An example of a simple and efficient multi-directional slicing algorithm is presented [109]. While this approach utilizes planar slicing, each plane is determined based on the geometric relationship between the plane and the 3D model, allowing for printing long curvilinear tube-like structures. Alternatively, the use of curved layers to enhance surface smoothness and reduce stair-stepping has been explored before [177] [178]. To improve surface quality and minimize "stair-stepping" in the final product, the surface is parametrically approximated. However, these techniques are unsuitable for all surface definitions.

2.6.2 Adaptations for Non-Planar and Free-form Surface Printing

Recently, there has been significant interest in developing techniques that enable printing on non-planar surfaces, particularly within the bioprinting community. One example involves evaluating a robotic path for material deposition by projecting the planar toolpath onto the deposition surface [179]. The algorithm was tested by printing a simple linear raster in a single layer on top of a non-planar 3D printed model, achieving an accuracy of 200 μm. Another study presented a non-planar slicing algorithm that blends planar and non-planar layers for reconstructing geometries and improving the aesthetics and electro-mechanical properties of 3D prints [180]. The internal structure uses planar layers, while the external shell utilizes non-planar layers, each having a shell and an infill. Tested on a 5-axis robotic printer, the approach adeptly printed on complex substrates and bone defects, outperforming existing methods by efficiently handling top and bottom non-planar surfaces. In another example, a cylindrical slicing method for additive manufacturing, creating a nonplanar toolpath

wrapped around a cylinder to generate parts suitable for the additive turning method, is developed. The model undergoes slicing into cylindrical layers, with each layer having an incrementally larger radius. This process yielded a three-dimensional toolpath suitable for the additive turning method. This approach addresses the lower tensile strength observed in conventional additive manufacturing and often reduces or eliminates the need for support structures.

The method's effectiveness is validated using a six-axis robotic manipulator equipped with a fused filament fabrication end effector and an external turning axis [181]. Another study presented work on designing nonplanar paths for single-shell layered robotic 3D printing and addressed challenges related to bifurcating shapes [182]. The authors introduce heuristics for target selection and surface segmentation, ensuring a uniform distribution of paths and preventing holes near bifurcations. The research also presents methods for interpolating multiple target curves on a single shape and handling asymmetric target curves. Fabricated prototypes successfully showcased the applicability and effectiveness of the proposed techniques. To reconstruct the surface of a wound, an alternative to expensive laser scanners is a simple design for a touch probe based on a light and spring system presented [183]. This design offers a cost-effective solution. Free-form surface slicing, it can produce a mechanically robust structure by exploiting the varying orientations between layers. It allows both the tensile and shearing components of the axial load to be decomposed, resulting in a more robust structure and a higher resistance to deformation with displacement. Since the layers vary in orientation, stress is distributed across the structure and not concentrated in one direction. For complex hydrogel bioprinting, another study outlines a method for 3D printing where a desired geometry is first imported, and planes in the X-Z and Y-Z axes are generated at increments corresponding to the desired print path width [184]. These planes intersect with the surface to create major paths connected into continuous paths within a layer using a nearest-neighbor algorithm. The resulting layers of paths are offset and duplicated to complete the full thickness of the print. G-code extrusion values are calculated based on nozzle size, material viscosity, and print speed. The process allows prints with either a single path direction or alternating path directions, and material changes can be inserted as needed.

2.7 In-Situ Fabrication on Moving Platform

Recent years have witnessed a surge in innovative methodologies aimed at fabricating tissue-analogous structures in-situ. These advances target applications such as the in-situ fabrication of skin, cartilage, and bone either directly on biological hosts or using models for demonstration through leveraging open-loop processes that are typically controlled either through 3 degrees of motion or by the manual

intervention [148] [22] [20] [150] [185]. A recent advancement, 'adaptive 3D printing', extends this notion by enabling direct printing on dynamic surfaces using integrated robotics and computer vision [186]. However, its application has been primarily limited to simple 2D scalar geometries. While such developments are promising, a prominent gap in these studies is their oversight of broader printing challenges. For instance, when the substrate isn't anchored to the printer, issues arise concerning alignment, reference frame establishment, employing a linear print head on a non-linear platform, and adopting a slicing methodology. The heart of these challenges lies in crafting a control strategy that seamlessly governs fabrication on shifting platforms, an aspect often underrepresented in in-situ bioprinting and broader 3D printing literature. In an endeavor to traverse these intricacies and establish platform-independent printing, insights from robotics, computer vision, tracking, and their application in related fields are needed.

2.8 Visual Tracking and Localization Techniques in Medical Robotics

Robotic manipulators are great for industrial and specialized applications that are humanely complex or sometimes even dangerous to perform [187] [188]. The first example of a surgical robot is the PUMA [189], which was introduced in the 1980s. Robot-assisted surgery has since evolved substantially, and the FDA-approved da Vinci surgical robot was commercialized in the 2000s [190]. Today, many commercial surgical robots are developed around this system [191] [192] [193] [194] [195], demonstrating that robotics has proved highly reliable in assisting and performing complex surgical operations [196] [197]. It is foreseeable that future bioprinting technology will evolve through incremental robot-assisted improvements [195] [198]. An essential task in the undertaken study is to enhance the robotic 3D printer’s ability to track the uncooperative target by developing and applying appropriate visual-servo control. A visual servoing task controls the position and orientation of the robots relative to the position of the target computed from image input [199]. The tracking is carried out through marker-based detection by vision sensors (camera).

Numerous visual tracking techniques are reported in the literature. For example, optical flow is a widely used technique for motion estimation and tracking problems that computes the relative motion of the object and the camera across many frames through intensity changes in pixels. This technique is used in intraoperative imaging to capture the motion of the parenchymal surface during the surgical procedure [200] and to estimate the pose of the robotic instrument [201] [202]. Other techniques for robotic tool tracking include multi-view stereo [203], mean shift algorithm [204], and tracking by detection [205]. More recently, machine learning algorithms such as neural nets and deep learning

frameworks have also been developed for tracking and localization, specifically in the medical field, including combining deep learning and bone tracking data for camera pose estimation [191]. In robotics, Simultaneous Localization and Mapping (SLAM) methods are employed on robots placed in an unknown environment tasked with mapping and self-localization [206] [207]. In medical robotics, SLAM techniques have been used for estimating camera pose in minimally invasive laparoscopic surgeries [36]. In the presence of measurement noise and process disturbances, a Kalman filter is used for the optimal estimation of the target state [206]. In robotics, it is a popular tracking filter choice with many visual-based feedback applications [207] [208]. In medical robotics, it is applied to the problem of tool detection and pose estimation [203] [209]. The Kalman filter assumes knowledge of a-priori noise covariance matrices related to process and measurement, allowing the estimation of hidden state variables that are not measured directly. Another critical function of the Kalman filter is the prediction capability in case of no measurement, which is critical given the independent operation of the visual feedback and printing control loop, each adhering to distinct temporal scales.

2.9 Challenges and Prospects

2.9.1 Standardization & Regulatory Approvals

Using different materials and techniques in in-situ skin bioprinting raises questions regarding the evolution of regulatory concerns and regulatory framework within each element. There are no regulations specific to in-situ skin bioprinting, as it is a relatively new technology. However, several regulatory concerns need to be addressed before the approval of the in-situ bioprinting process, for example, the safety of the in-situ bioprinting process, intellectual ownership, ethical concerns, and legal concerns.

Food and Drug Administration (FDA) authority in the US has already concerted efforts with the American Society for Testing and Materials (ASTM F2211-13(2021)) to recognize consensus standard guidelines for Tissue Engineered Medical Products (TEMPs) [210]. Moreover, standards specific to skin substitutes include, for example, ASTM F2311-08 (Classification of Therapeutic Skin Substitutes, withdrawn 2017). To further develop the in-situ bioprinting field, the research community can rely on the developed standards for tissue engineering applications; for example, ASTM F2212-20 describes the standard guide for characterization of type I collagen as starting materials for surgical implants and substrates for tissue-engineered medical products. Furthermore, the FDA also established the Office of Combination Products in 2002 to fast-track the regulatory assignment and premarket review of novel therapeutics under the Medical Device User Fee and Modernization Act of 2002 (MDUFMA) [211] [212]. Currently, there are four existing expedited regulatory pathways by FDA: Fast Track

development (US FDA, 2017b), Breakthrough Therapy designation (US FDA, 2014a), Accelerated Approval (US FDA, 2014b), and Priority Review for drugs (US FDA, 2014d) [212]. Moreover, the 21st Century Cures Act (Cures Act) was passed in December 2016 in the United States. Under this law, patients with severe or potentially life-threatening conditions will be able to receive novel therapies faster and easier. As part of the Cures Act, eligible biologics products may be designated as Regenerative Medicine Advanced Therapy (RMAT), while specific innovative medical devices can be reviewed under the Breakthrough Devices program (US FDA, 2016). There is a commitment on the part of the FDA to provide expanded access to patients for the treatment of select diseases with high mortality or morbidity risks. It is possible for in-situ bioprinting of skin to be clinically applicable by combining these alternative routes to provisional and full approval so that more patients with the greatest medical needs can benefit from the most advanced treatments.

2.9.2 Cell Sourcing

In most cases, in vitro cell expansion will be required before surgery for in-situ skin fabrication due to the high number of cells required [213]. As a result, ethical concerns appear regarding the approval of in vitro stem cell expansion and the subsequent direct use of these cells in surgery [214]. Many countries disapprove of using stem cells, such as embryonic stem cells (ESCs), due to ethical concerns and noncontrollable differentiation [215]. In addition, proliferative senescence and loss of stem cell properties can also occur during stem cell expansion in the laboratory [213] [213]. It can induce an inappropriate immune response after printing allogeneic cells, biological or non-biological material. A lack of integration with the host tissue can lead to improper development and rejection of the construct by the host [216].

2.9.3 Printing Phase

In the implant design, new approaches must be developed to fabricate a heterogeneous skin construct representing the skin's natural structure. Studies based on controlled porosity, surface design, and cellular distributions have rarely been reported in the case of skin [217]. Development of material needs to address challenges currently faced, such as post-implantation swelling and implant shrinkage. Moreover, innovative slicing methodologies can be used to design structural layers with controlled surface topography and mechanical properties in the preprinting phase. Currently, flexibility in customizing deposition toolpath is very limited as the printing workflow is planar and adopted from the in vitro bioprinting [218]. During the printing phase, real-time tracking and compensation of the printing site via high-resolution sensors are needed to avoid deposition inaccuracies arising from the

body's possible movement. In addition, opportunities exist in AI's application for real-time monitoring of the printing process for possible defects. If such in-situ printing technologies can be successfully delivered for the skin, broader applications in tissue engineering can benefit the skin alone.

2.9.4 Post-Printing Phase

Post-printing maturation of the construct is influenced by factors such as structural fidelity, the immunogenic response of the host, cellular regenerative support, and degradation kinetics [17] [215]. A number of bioinks require external environmental cues for phase change, i.e., gelation, to occur after printing (e.g., UV light curing, chemical exposure, and temperature change). Traditional surgical procedures cannot deliver these cues in a consistent manner within a living body when in-situ bioprinting is performed [219] [220]. Therefore, the number of bioinks developed for the in-situ bioprinting of skin is limited because of issues like biocompatibility and toxicity of external cues. However, ultraviolet as an external cue has recently been successfully used to treat chondral defects in sheep via in-situ bioprinting [221]. There is a need to revisit the biocompatibility of these external cues when applied to the application of in-situ skin fabrication and formulate bioinks that are suitable for in-situ processes. Vascularization needs for skin tissue maturation needs to be addressed for in-situ bioprinting in a clinical setting. In this case, the skin layers that demand minimal or no vascularization (e.g., dermis) have no such issue [222]. Due to the absence of an internal vascular network, an insufficient supply of nutrients and oxygen to deeper layers of skin is a challenge in the maturation process [215]. For the implanted skin constructs to integrate properly with surrounding tissue, vascularization must be achieved within four days [223]. Initial vasculature networks can be designed in implant geometry to support the vasculogenesis process carried out by cells. The problem of delayed vascularization can be alleviated by combining cell-based, biomaterial-based, and microfabrication approaches [210]. Another challenge is to control the post-printing degradation rate of the natural tissue formation process. The ECM protein production rate should match the printed biomaterial's degradation rate to provide sufficient time for tissue maturation [17].

2.9.5 Clinical Cost

Costs associated with cellular therapies (US$10 – 100/cm^2) and skin substitutes (> US$100,000 for greater than 50% of the body area) are high due to the overhead of surgical and hospital expenses [211]. The cost of current therapies in wound care must be considered so that the cost-effectiveness of in-situ bioprinting may be determined when setting long-term priorities in wound care [211]. However, during

acute care of burn wounds, determining cost-effectiveness is secondary to the more immediate needs of patients.

2.9.6 Clinical Applications of In-situ Bioprinting of Skin

3D printing, biological materials directly onto wound sites in-situ bioprinting promotes tissue regeneration by 3D printing biological materials directly onto the wound. Bioprinting can potentially improve wound healing outcomes in several clinical applications, including in-situ wound regeneration. For example, it can improve wound healing outcomes by stimulating the regeneration of damaged tissues. This is done by delivering the arrangement of cells, growth factors, and matrix directly onto the wound site. In addition, in-situ bioprinting can reduce scarring and improve wound aesthetics by controlling the spatial arrangement of cells and extracellular matrix components. Moreover, through the delivery of growth factors and cells directly to the wound site, as well as through the provision of a structured template for tissue regeneration, in-situ skin technology can aid in faster wound closure. Furthermore, technology for in-situ skin bioprinting is portable, meaning it can reach the patient without needing a hospital setting. Further research and development are necessary to fully realize the potential of in-situ bioprinting in wound healing and other clinical settings.

In-situ skin bioprinting is well-suited for wounds requiring a larger surface area of skin regeneration and complex geometries, such as chronic wounds, burns, and extensive traumatic injuries. Skin implants offered by this method are customized according to the wound's size, shape, and contours. Bio-printed implant tissue contains living cells that can proliferate and differentiate to form new skin tissue, contributing to the potential for more rapid healing than skin grafts, which may take longer to integrate into the surrounding tissue.

The standard gold treatment for wound repair is split-thickness skin grafting, which involves the removal of healthy skin from a donor site, which can result in pain, scarring, and functional impairment. In comparison, in-situ bioprinting does not require the removal of healthy skin, reducing the risk of donor site morbidity. However, it may involve biopsy or blood removal to source cells that can be cultivated and expanded in the laboratory to produce a large tissue supply. In-situ bioprinting is a suitable alternative therapy in cases where the success rate of split-thickness graft is less, for e.g., patients with a large burn area ($\geq$ 35%) of the body, age greater than 55, and the presence of other medical conditions [224]. In the case of severe burn injuries, the donor tissue cannot cover the wound thoroughly, and meshed grafts are known to result in undesirable cosmetic outcomes. Using in-situ bioprinting to treat traumatic injuries with large surface areas and complex geometries can be

advantageous. When treating chronic wounds, split-thickness skin grafting might be less effective since the graft may not adhere well to the surrounding tissue. In-situ bioprinting of skin may provide an alternative strategy to the treatment of wounds that do not heal with conventional approaches in the reconstructive ladder [225].

2.9.7 Future Prospects

Recent advances in tissue engineering and bioprinting have opened up opportunities to fabricate skin implants in-situ. Cells can be delivered with scaffolds using bioprinting techniques, guiding and supporting the regeneration process at the cellular level. Even though the concept of printing on a live biological platform is still in its infancy, recent demonstrations of in-situ bioprinting of skin suggest a promising outlook. Fabricating customized skin tissue seems like a naturally progressive step in moving away from in vitro dermal substitutes that cater to a singular goal. However, the problem of creating live skin tissue is inherently complex and different from the in vitro process owing to the dynamic physiology of the human body and the critical requirements needed for the printing process. The current in-situ printing approach is adopted from the in vitro bioprinting process. While lab-based bioprinting can be used to present a proof of concept for the in-situ printing of skin, there is a need to develop technology that is more suitable for the dynamic conditions encountered when printing on a live body.

The actual execution of in-situ skin printing will differ from being handheld or robotic, and each method has strengths. The handheld approach seems less expensive and easier to administrate than the robotic framework to deliver skin. When extended to free-form fabrication, the planar framework of current tabletop technology will be essential in applying skin layers aligned with the wound surface's contours. The operation of printing on a living body is dynamic, and complexity lies in handling physiological and random motion during the printing operation. The printing modality (printing nozzle, UV light exposure, etc.) affects the host's cellular activity, and their adaption for use in a surgical setting is a challenge. An important aspect is device design, software, and AI integration. In-situ, skin bioprinting is a technically complex process that requires specialized equipment and expertise, which may limit its availability and accessibility. The surgeon involved, who may not have much technical knowledge about the printing device, will significantly benefit from an ergonomic design and a user-friendly interface that requires minimal human intervention. AI integration in the device will regulate printing parameters and ensure precision and surgical quality. Integrating online monitoring and inspection sensor systems and a feedback control system can provide opportunities for real-time quality

control while printing a tissue construct. Additionally, high-definition 3D scanning and machine vision systems will allow for real-time corrections of printing errors caused by the dynamic printing surface.

In-situ skin bioprinting is still in its early stages of development but is rapidly growing and developed for use in clinical settings. Subsequent growth and demonstration of this concept need reimagining the bioprinting technology suitable for complex in-situ environments. Currently, in-situ skin bioprinting is technologically limited, which restricts its use to smaller wounds or simpler injuries. Moreover, the long-term stability and functionality of the printed skin tissue remain to be thoroughly evaluated. The limitation of current technology also serves as an opportunity for future directions. To further the field of in-situ bioprinting, a multidisciplinary effort is needed to focus on biomaterial-directed regeneration and the design of sophisticated implants for in-situ printing processes. With advancements in in-situ bioprinting of skin, cell-infused engineered skin can be made on-demand and customized to a patient's wounds.

2.10 Conclusions

Achieving skin regeneration remains an ambitious goal, but new techniques and methods in bioprinting are making it increasingly possible. In-situ skin bioprinting is still in its early stages of development but is rapidly growing and developed for use in clinical settings. Subsequent growth and demonstration of this concept need reimagining the bioprinting technology suitable for complex in-situ environments. Currently, in-situ skin bioprinting is technologically limited, which restricts its use to smaller wounds or simpler injuries. Moreover, the long-term stability and functionality of the printed skin tissue remain to be thoroughly evaluated.

From a material point of view, biomaterials derived from natural sources have been investigated in-situ because of their higher biocompatibility and similarity to native skin. Although many natural biomaterials are available for tissue engineering of skin in vitro, three of them (collagen, gelatin, and chitosan) have been used extensively in-situ or commercially. Natural polymers have poor mechanical properties and are rapidly degraded, which hinders their use in clinical settings, therefore a suitable crosslinking strategy is immensely important for in-situ skin regeneration.

Both GelMA and synthetic materials have their respective advantages and limitations in wound healing applications. GelMA offers biocompatibility, tunable mechanical properties, and ease of modification, making it a versatile option for bioprinting and tissue engineering. Its ability to support cellular adhesion and proliferation is particularly beneficial for creating functional wound healing scaffolds.

On the other hand, synthetic materials provide controlled and reproducible properties, which can be crucial for standardized wound healing applications. However, they often result in visible scarring and fail to fully mimic the complex hierarchical structure of native skin.

The limitation of current technology also serves as an opportunity for future directions, that should be addressed by a multidisciplinary effort focused on biomaterial-directed regeneration and the design of sophisticated implants for in-situ printing processes. For the advancement of in-situ bioprinting, an improved technological framework for developing bioprinters is necessary. This requires combining current knowledge in skin regeneration directed by biomaterials, identifying limitations in current state-of-art, and conducting translational research to construct a new technological framework that incorporates emerging technologies.

Chapter 3 Bioprinting on Non-Planar Surfaces

Summary: This chapter deals with challenges associated with bioprinting on non-planar surfaces, a crucial advancement for in-situ tissue engineering applications. The chapter begins with an introduction to the complexities and necessities of adapting bioprinting techniques for free-form non-linear platforms. Next, the development of slicing software is presented in detail, followed by the technical advancements and adjustments required to transition from flat to 3D surface bioprinting. Moreover, the construction of in-situ bioprinting hardware is discussed, including the crucial steps of registration and localization of the target printing platform. Testing and evaluation of the developed system are detailed, with a focus on the multilayer slicing of skin implants and the application of bottom-up and top-down approaches to surface slicing. The chapter concludes by addressing the challenges and limitations encountered in developing and applying bioprinting on non-planar surfaces.

3.1 Introduction

3D printing technology has readily evolved to provide specialized solutions for skin wound healing applications in tissue engineering [16]. In in-vitro approach to bioprinting, a complex geometry scaffold is fabricated to provide the necessary structural and biological environment for the cells to regenerate [226]. Recent advancements in in-situ approach to bioprinting have enabled the printing of engineered biomaterial for skin (with or without cells) directly on the body [26]. These bio-printed implants attached to the biological host interact with the body's natural response to trigger wound healing [65]. The most challenging aspect of bioprinting is ensuring that the printed tissues remain functional after printing [227]. Based on the biology of the cells being used and the target tissue, biomaterials, growth factors, and implant design must be understood and balanced appropriately [87]. It has been shown that the surface characteristics of the implants significantly affect the innate and adaptive immune response and are crucial to the transfer of blood and nutrients to cells embedded in the implant [66]. Moreover, in-situ printing is typically conducted using printers designed for flat surfaces and planar layer slicing, which are inadequate for printing on the inherently non-planar geometry of the human body. Therefore. developing specialized in-situ bioprinting slicing technique is necessary to achieve customized surface characteristics and tunable implants.

Next, this chapter presents a slicing design and tool path generation methodology for a skin implant based on free-form surface slicing. Our approach enables the creation of implants with multiple layer sections, each slice with a different surface design and toolpath parameters, and is free of the stair-

casing effect. With this approach, each of the three sections of the skin implant can be designed to have properties like porosity and mechanical strength that are native to each skin layer. Moreover, the proposed method allows the fabrication of skin implants with an enhanced degree of geometric fit and avoids the effect of planar fabrication, like the stair-casing effect. The mathematical models used to represent free-form surfaces and demonstrate the applicability of the models to generate G-code files for non-planar slicing surfaces of skin implants are also provided. Moreover, visualizations of the simulated toolpath and show some test results to illustrate the effectiveness of this approach are also presented.

3.2 Development of Slicing Algorithm

3.2.1 Planar Slicing Method

The planar slicing process for bioprinting starts with a triangulated mesh representation (STL model) of the implant geometry. STL file is a collection of many triangulated facets' ζ' representing the body's exterior, defined by coordinates of vertices '*v*' and average vector '*n*' (see Figure 3-1) [172]. Planar tool path for bioprinters is created by slicing STL models into horizontal cross-sections. A 2D polygon or the exterior boundary of an implant is formed by intersecting the model of the part with a plane. Stacked 2D slices will approximate the 3D object when printed with a specific layer thickness. Calculating the intersection of the STL model of the implant with the slicing plane creates the boundary of each 2D sliced polygon (see Figure 3-1). This is done by computing the intersection of the slicing plane with every triangular facet in the STL model, which is a simple geometry problem. The slicing plane and a facet plane have a line of intersection bounded by two points if they intersect. These line fragments form the boundary of the 2D sliced polygon. A suitable toolpath trajectory is then calculated based on the infill pattern, determining how the cross-section's interior is filled. Typically, each layer of the linear fill is rotated 90° every other time, creating a 0°/90° infill pattern. A step-by-step illustration of the planar slicing procedure is presented in Figure 3-1.

3.2.2 Surface Slicing Method

In comparison to planar printing, where an object is sliced with a horizontal plane, surface slicing utilizes the free-form representation of a surface to create the layers of the object to be printed. First, the model representation of a free-form surface is described, followed by the procedure developed for slicing.

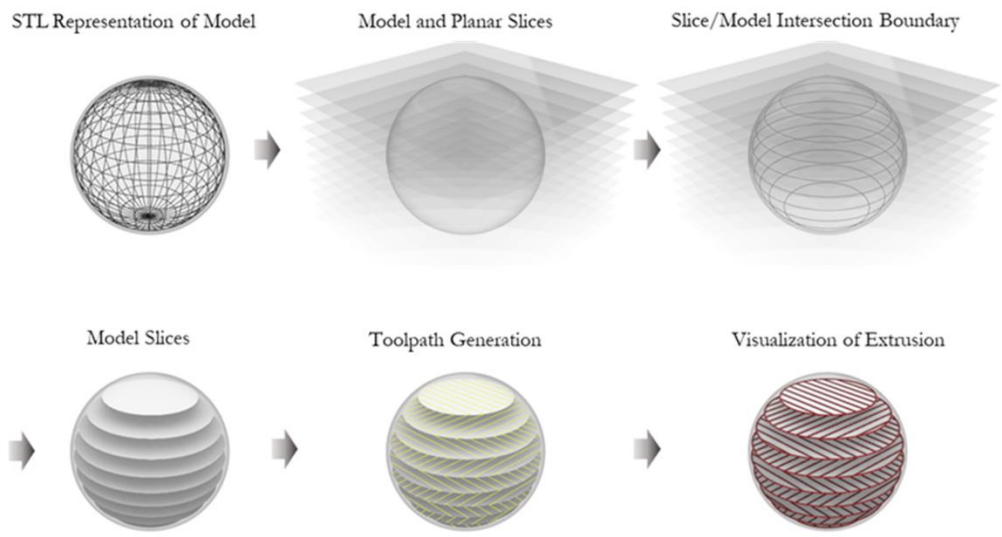

Figure 3-1: A step-by-step illustration of the planar slicing process, STL representation, overlay of model and slicing planes, creation of layer boundary, slice representation, toolpath generation, and visualization of final deposition.

3.2.2.1 Surface Representation

Surfaces can be represented in computational geometry in a variety of ways. Parametric functions and implicit equations are two of the most common methods of representing curves and surfaces in geometric modeling. Surface slicing involves representing each layer as a parametric surface. In parametric form, an *x*-*y* point is represented by independent explicit functions. To represent complex high-degree surface curves, they are numerically unstable and inefficient to process, as they must satisfy many constraints (the number of control points is directly related to degree). Several piecewise polynomial curves can be joined together at breakpoints called *knots*. Segmental divisions of the parametric domain are marked by knots or breakpoints and are connected under continuity constraints. Any of the standard polynomial forms can be used to represent a curve segment $C_i(u)$. B-spline basis functions are utilized as weights, similar to Bezier basis functions. However, their application has two notable differences: firstly, the domain is divided by knots, and secondly, the basis function remains constant within each interval.

It is possible to represent parametric surfaces in various ways, and one of the commonly used methods is the tensor product form. In this approach, surfaces are defined as bidirectional curves using bivariate basis functions of u and v. These basis functions are derived from the product of univariate basis functions [228]. A tensor product surface patch is created by moving a curve through space while enabling it to undergo deformations. A curve *C(u)* can be defined as a vector value function based on

the parameter u, mapping a straight-line segment into three-dimensional space. Similarly, a surface patch is based on two parameters, u and v, and is formed by mapping a u-v plane into Euclidean three-dimensional space.

A curve with p-th degree B-spline bases functions and control points P_i can be represented as,

$$\mathbf{C}(u) = \sum_{i=0}^{n} N_{i,p}(u)\mathbf{P}_i \;\; a \le u \le b \tag{3-1}$$

A surface, in general, can be defined as,

$$\mathbf{S}(u,v) = \big(x(u,v), y(u,v), z(u,v)\big), (u,v) \in \Re \tag{3-2}$$

A tensor product of a surface takes the form,

$$\mathbf{S}(u,v) = \big(x(u,v), y(u,v), z(u,v)\big) = \sum_{i=0}^{n}\sum_{j=0}^{m} f_i(u)g_j(v)\mathbf{b}_{i,j} \quad \text{where } \begin{cases} \mathbf{b}_{i,j} = (x_{i,j}, y_{i,j}, z_{i,j}) \\ 0 \le u, v \le 1 \end{cases} \tag{3-3}$$

Furthermore, a slicing surface is a Non-Uniform Rational B-Spline (NURBS) surface patch with degree p in the u direction and degree q in the v direction,

$$\mathbf{S}(u,v) = \frac{\sum_{i=0}^{n}\sum_{j=0}^{m} N_{i,p}(u)N_{j,q}(v)w_{i,j}\mathbf{P}_{i,j}}{\sum_{i=0}^{n}\sum_{j=0}^{m} N_{i,p}(u)N_{j,q}(v)w_{i,j}} a \le u, v \le b \tag{3-4}$$

here, the bidirectional net of control points is defined by $\{P_i\}$, $\{N_{i,p(u)}\}$, and $\{N_{j,q(v)}\}$ are the NURBS basis functions. NURBS surface is reduced to a Bezier's surface patch if the control points for u and v are the same as the order of the B-spline basis function.

The strength of NURBS formulations is the ability to accurately represent complex surfaces and conics such as ellipses, hyperbolas, and circles. Furthermore, NURBS formulation offers local approximation. Control points can only affect a local portion of the surface if they are moved. To achieve local shape control, control point movement and weight modification are critical. Since the method has been adopted into many international standards, such as IGES, STEP, etc., it has become the most widely used geometric representation method in CAD/CAM. NURBS-based surface models can be accessed by software such as Rhino 3D, which offers a Python scripting interface and access to its common API. The NURBS surface-based slicing process was implemented using the Grasshopper plugin for Rhino 7 and Python-based RhinoScriptSyntax API, which provides access to powerful NURBS functionality.

3.2.2.2 Surface Slicing Procedure

Once the desired surface for slicing is modeled, the rest of the procedure is similar to the planar slicing procedure. The selection of the slicing surface governs the output surface characteristics of the object. In in-situ printing of implants, a free-form surface fitted to the scanned point cloud of the wound/defect site will result in an implant with a surface profile that is similar to wound geometry. A sliced implant with a surface that matches the exterior of the implant will yield a high degree of surface smoothness on the outer surface. Next, a set of vertically offset surfaces spaced at layer height is generated. The intersection of each surface in the set is computed with the geometry of the implant to yield the boundary of slices that exist on each surface and are bounded inside the implant model (see Figure 3-2). The intersection of each boundary curve with the respective surface generated the slices on which the toolpath is computed. For each slice, the perimeter toolpath is computed by offsetting the boundary curve on the surface by a distance equal to half of the linewidth (printing parameter). Next, an infill raster is generated for each slice by extracting the first two iso-parametric curves in the u and v directions from the underlying surface. Seed points for the infill curve are generated by dividing the two seed curves into smaller segments equal to linewidth, and the resulting points are extracted. The length of these segments controls the amount of infill and the final porosity of the implant. At each of the seed points, ISO curves on the surface are extracted and sorted in an array. The collection of perimeter and infill curves represents the toolpath movement of the deposition nozzle. Lastly, the toolpath curves need to be converted to G-code format, which is a sequence of point-to-point movement commands along the path curves. The software workflow of surface slicing is illustrated step-by-step in Figure 3-3.

3.2.2.3 Toolpath Generation and Flow Calculations

Each G-code command contains instructions for the position of the nozzle and also the amount of filament to be extruded along the path. A typical G-code command of "G0 X1 Y1 Z1 E1" would mean a movement to coordinates (1, 1, 1) while extruding 1 unit of filament. The E value is the length of filament with a diameter d_f needed to fill the volume defined by the print area A_e and path length L_e. In Slic3r software, the print area is approximated by a rectangular center with a semi-circle on either side [229]. For implementation, the cross-section of the printed fiber or the print area A_e is represented by an ellipsoidal cross-section along the traveling path length of the nozzle. By an ellipsoidal cross-section or extrusion area A_e across the length of the traveling motion. The height of this rectangle is the layer

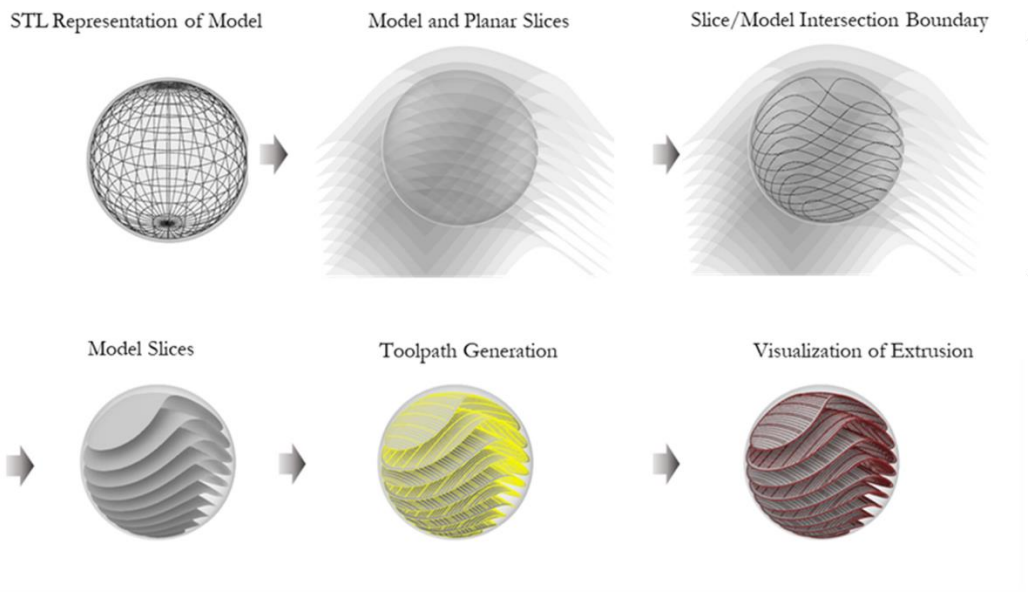

Figure 3-2: A step-by-step illustration of the surface slicing process, STL representation, overlay of model and slicing surfaces, creation of layer boundary, slice representation, toolpath generation, and visualization of final deposition.

height, and its width is the deposition line width. A_e and E are calculated by using the following equations,

$$A_e = \pi * w_e * h_l \tag{3-5}$$

$$E = A_e * L_e * \pi \left(\frac{d_f}{2}\right)^2 \tag{3-6}$$

where E is the length of extrusion, and L_e is the path length to be traveled from the current coordinates to the position defined in the geometric code (G-code). The final output is implemented according to formatting and the firmware of the bioprinter.

3.3 Construction of In-situ Bioprinting Hardware

The experimental verification of surface-based printing was conducted using a setup comprising a Dobot Magician robotic manipulator running on Marlin, an open-source Arduino-based firmware. In the printing mode, the system exhibited a remarkable resolution of up to 0.1 mm and enabled printing within a maximum volume of 150 *mm* x 150 *mm* x 150 *mm*. This product is marketed with a maximum rated payload of 500 g, arm length of 320 mm, and a maximum speed when moving in a straight line

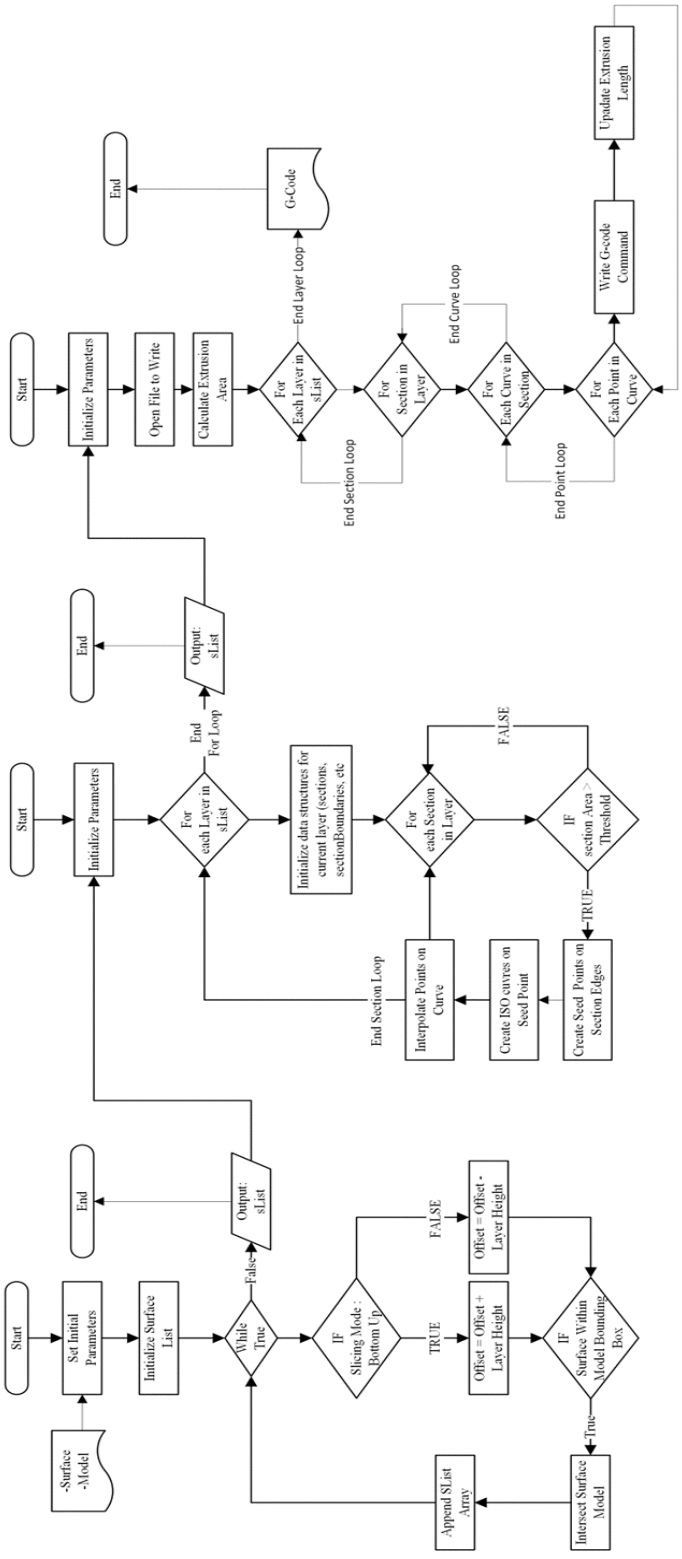

Figure 3-3: Surface slicing and toolpath generation workflow is decomposed into three parts: slicer, toolpath generation, and G-code generation.

of 800 mm/s. This arm has an integrated motor controller that can realize numerous motion functions, such as linear and arc interpolations. The motion of the manipulator is controlled by G-code programming sent from the computer via the serial interface. Each line of the G-code script indicates the target point and amount of material to be extruded. Since the command lines are sent to the printer sequentially, the printer has to wait for the first command to execute before reading the next command. Dobot Magician in the 3D printing mode allows for the use of the RepRap Marlin 3D printing framework and allows for a communication protocol that is native to most commercial 3D printing devices. For localization of the hand model, the visual system incorporated two cameras: a USB camera (Microsoft LifeCam Studio) that streams at a rate of 30 fps with a pixel resolution of 1920 x 1080 and a secondary 16 MP (ELF USB) camera (see Section 3.3.1 for details). Both cameras were two-dimensionally calibrated to the printing surface using the perspective calibration model. Prior to the calibration, the image underwent thresholding and a particle filtering step.

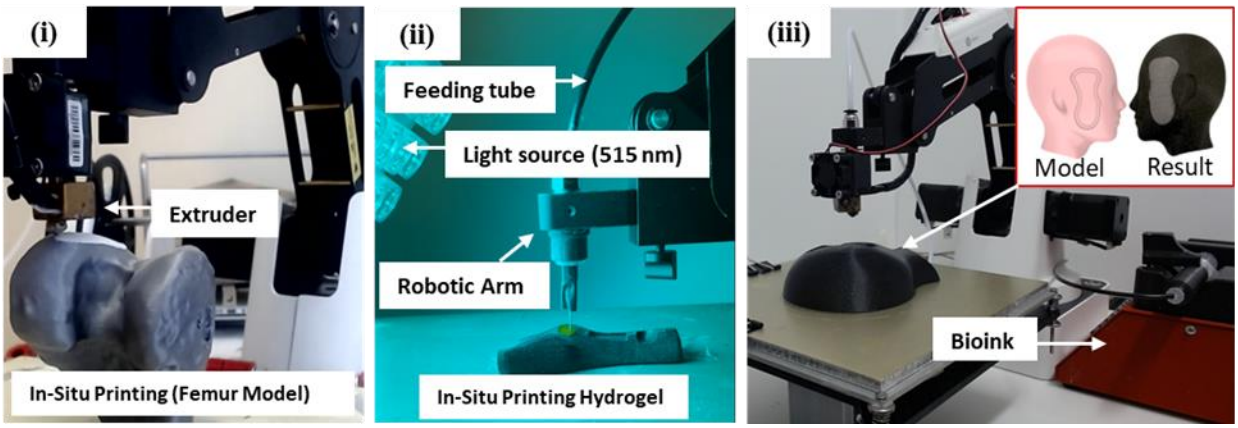

Figure 3-4: Functional setup of the in-situ bioprinter: (i) polymer in-situ printing of an implant on a femur model, (ii) in-situ printing of photo-cross linkable hydrogel under cyan light, (iii) overall setup of the bioprinter.

The print head was specifically customized to accommodate two distinct material types: polymers and hydrogels. Polymers, e.g., PLA and PCL, were extruded through a heated nozzle measuring 0.4 mm in diameter. Hydrogels, such as Gelatin methacryloyl (GelMA), were dispensed through a motor-driven syringe (10 ml) dispenser connected to a deposition needle (ranging from 22G to 26G) via a black feeding tube. Modifying gelatin with methacrylate anhydride created a photo-cross-linkable GelMA biopolymer capable of crosslinking under visible light. This process employed eosin Y as the photo-initiator in conjunction with triethanolamine (TEOA) and vinyl caprolactam (VC). The composition of hydrogel consisted of 20 µL of eosin Y, 400 μL of TEOA, 0.2g VC, and 1 G GelMA in 10 ml phosphate buffered solution (PBS). The LED lamp emitted CYAN light at 515 nm at an irradiance of 25 mw/cm^2. The functional in-situ bioprinting setup is presented in Figure 3-4.

Hand and face models were printed separately with wounds of different geometries and thicknesses for demonstration purposes using a planar desktop 3D printer (Prusa Mk3). The wound geometry is generated by subtraction of the healthy hand model with the wound model. In practical applications where the healthy model is not available, other techniques for computing the implant geometries are required [230]. An important input to the surface slicing procedure is the slicing surface, which can be computed from the wound's scanned surface profile or flexibly selected according to the design requirements. In the first case, where the surface is defined from the point cloud, a simple method such as that described in [231] can be used to approximate the wound surface from the point cloud generated from the 3D profile scanner. While it is a good approach to use the wound surface for the initial layers to maximize contact, other types of surfaces can also be used to slice the implant. For examples, three different surface profiles can be used to slice the three sections of the skin implant. It is also suggested that the top layers be sliced with a surface that represents the exterior of the healthy model to ensure an aesthetically smoother match with the wound boundary. To validate the printability and applicability of the surface slicing method, the implant on the hand model is printed with PLA material with a total of 3 layers, and the face model is printed with PLA and GelMA hydrogel.

3.3.1 Registration and Localization of the Target Printing Platform

Localization of the printing area/platform within the robotic workspace is a crucial step to ensure successful printing when printing on foreign objects. Cameras were mounted to provide a clear, unobstructed view of the model and any associated tags placed on the phantom model and the printing platform (see for Chapter 4 for details). These cameras were calibrated, capturing calibrated grid points to estimate intrinsic and extrinsic parameters. During this camera calibration process, threshold operations were conducted, followed by the application of a particle filter. This approach was instrumental in accurately determining the pixel coordinates of a circular grid pattern. Subsequently, the target's registration was accomplished through a feature extraction process utilizing a grayscale pyramid template matching algorithm. An initial point cloud dataset of visual tags on the workspace was captured using these cameras. From this dataset, one point was selected as the workspace origin, which was then set as the robotic workspace origin.

To ensure high precision and accuracy, the tracking system was calibrated using a reference grid. The robot's position was measured repeatedly to assess precision, accuracy, and repeatability. Statistical analysis, including standard deviation and mean error calculations, confirmed the system's reliability with a relative error of less than 1%.

In practical applications, a 3D scanner would be employed first to capture a high-resolution scan of the phantom model. This scan, serving as the reference dataset, is crucial for the effective application of the Iterative Closest Point (ICP) algorithm. The phantom head/hand model was positioned within the robotic workspace, aligning with this reference dataset. The robotic arm played a pivotal role in capturing a secondary point cloud dataset. This was achieved by carefully positioning the printing nozzle on the designated tags or selected landmarks and recording these points. The ICP algorithm was then applied, aligning the point cloud data captured by the robot (consisting of tags/selected markers) with the high-resolution 3D scan or the corresponding CAD model. Adjustments to the algorithm's parameters were made iteratively to ensure optimal alignment with minimal residual error.

Upon accurately localizing the model, the coordinates of the CAD model or the 3D scan were transformed into the robotic arm's coordinate system. This transformation is critical, particularly when designing implants on the wound site of a phantom head/hand model. The implant's toolpath is generated within the robotic workspace's coordinate system, ensuring that when printed, it aligns perfectly with the localized platform. This procedure lays the foundation for the precise alignment of the printing process within the workspace.

3.3.2 Hydrogel Formulation

To synthesize visible light-based GelMA [232], 10 g of gelatin (type A, gel strength 300) from porcine skin (G2500, Sigma-Aldrich) is dissolved in 100 ml phosphate-buffered solution (PBS) while stirring at 200 rot/min and maintaining the temperature between 37-45 ^{0}C (to avoid thermal gelation) for 90 mins. For functionalization of gelatin, 6 g of methacrylic anhydride (94% purity, 2,000 ppm topanol A as inhibitor, Sigma-Aldrich) is slowly added in dark conditions while vigorously stirring at 1500 rot/min for 3 hours. After the reaction, the solution is centrifuged to remove unreacted methacrylic anhydride, followed by dilution of the supernatant solution with an equal volume preheated of ultra-purified water. The resulting solution is transferred to a dialysis membrane tube (12 kDa) for dialysis against ultra-purified water for seven days at 40 ^{0}C. After, the pH of the GelMA solution is adjusted to around 7.4 using 1 NaHCO3 (1M), followed by freeze drying for seven days.

Visible light-based GelMA biomaterial is amalgamated by dissolving 1 g of freeze-dried GelMA in 5 ml of PBS while stirring and heating at 40 0C. After GelMA has fully dissolved, 0.2 g n-vinylcaprolactum (98% stabilized, Sigma-Aldrich), 400 μl of triethanolamine, and 20 μl of eosin-y free acid in dark conditions [2]. Biomaterial is crosslinked under cyan light (500 nm), delivering power at 25 mW/cm^2 for 30 secs.

3.4 Testing and Evaluation

3.4.1 Multilayer Slicing of Skin Implant

The surface slicing methodology developed was applied to the application of in-situ bioprinting of a skin wound defect model. For demonstration, a wound was created on a 3D hand model to generate the implant geometry. Different cases of slicing surfaces were simulated and presented in the following subsections.

3.4.2 Bottom-Up and Top-Down Approach to Surface Slicing

In the bottom-up approach, the surface of the wound is first fitted and evaluated from the scanned point cloud. Next, this surface is used to slice the implant geometry vertically, as presented in Figure 3-5. In this approach, the first slice exactly matches the wound site and avoids the formation of the stair-case effect, which is crucial in the application of skin implants. Moreover, an exact geometric match would maximize the contact area of the implant and the wound site and reduce implant misfit and possible displacement from the desired location. The formation of stair-cases in the contact surface produces void areas with reduced biological activity and transfer of nutrients in the implant. However, the bottom-up approach would result in an exterior surface that is not controlled as the bottom surface can be geometrically distinct from the top surface. Bottom-up slicing is simulated in Figure 3-5, and the top-bottom view of the implant is also presented to visualize the resulting surface characteristics.

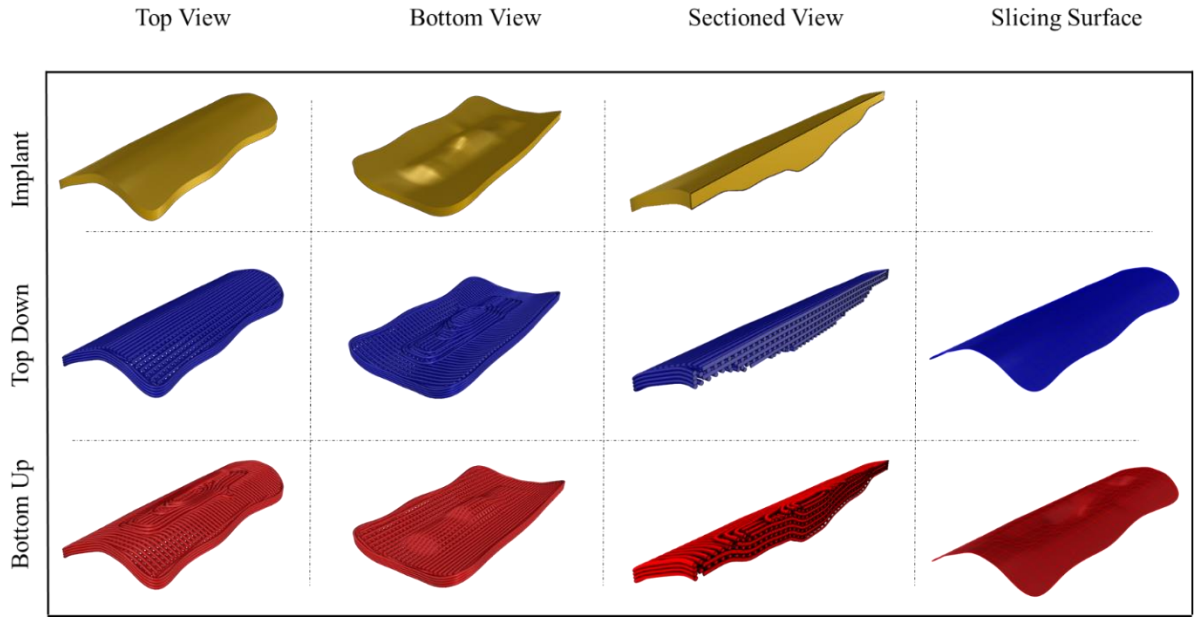

Figure 3-5: Visualization of the top-down and bottom-up approach to surface slicing.

In the top-down approach, the exterior/top surface of the implant is used as the slicing surface of the implant model. Similarly, the exterior surface of the implant is used to slice the implant vertically downward. This approach preserves the exterior surface as the deposition nozzle is moving along the iso-parametric curve lying on the surface. Figure 3-5 illustrates an implant with geometrically distinct top and bottom surfaces sliced with the top-down approach. The simulated G-code showing the final deposition pattern is also shared and shows the perseverance of the top surface after printing. The infill direction of each layer is rotated 0/90^{o} to yield a criss-cross pattern.

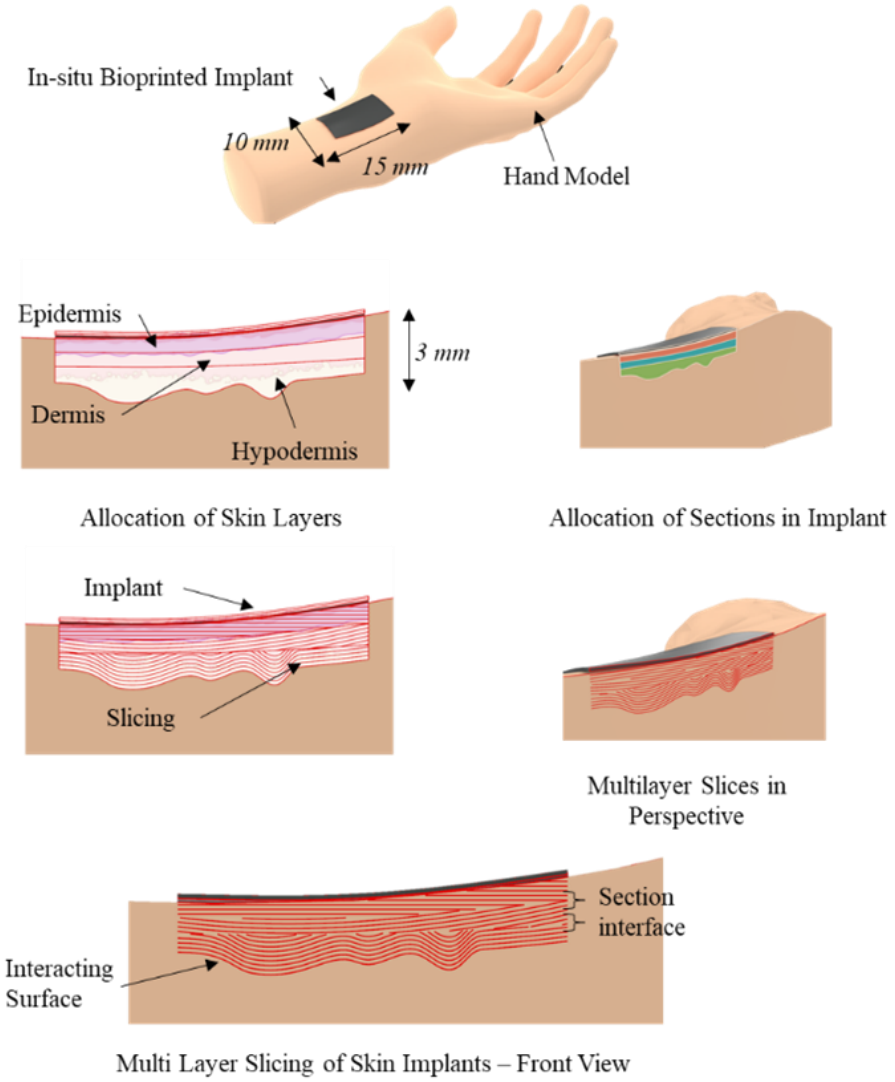

Figure 3-6: Visualization of implant, layers, and slice design placed in the hand model with different views. The illustration of the multi-layered design of skin implant where each section represents a layer of the skin.

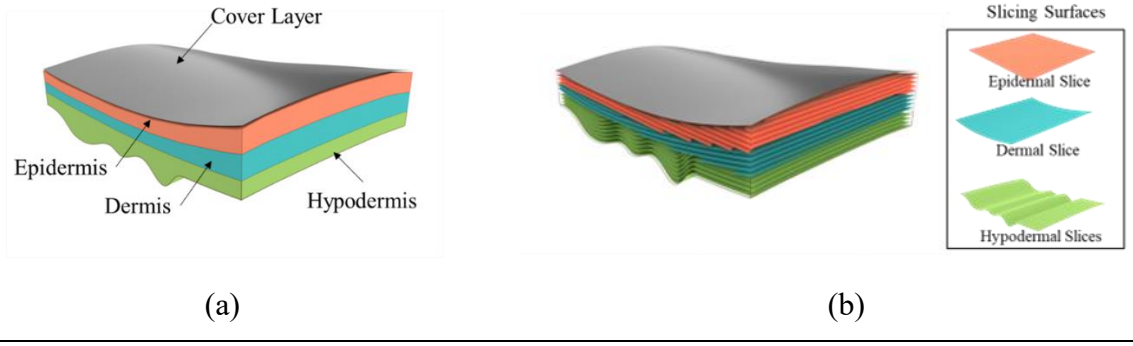

Figure 3-7: (a) The illustration of the multi-layered design of the skin implant where each section represents a layer of the skin, (b) Visualization of slices in each layer (epidermis dermis and hypodermis) of the implant sliced with a different surface

3.4.3 Multi-Layered Slicing for Skin Implants

Replicating a section of skin in bioprinting design for full-thickness wound healing applications requires that the implant ideally be designed with three different regions mimicking the properties of the epidermis, dermis, and hypodermis. Depending on anatomic location, each region has different thickness and mechanical properties, as discussed previously in Section 2.4. Properties like porosity and material stiffness are known to affect cellular migration and differentiation [61], [66]. Moreover, the surface of the implant in contact with the wound site serves as the first barrier that contains the exudation of fluid, proteins, and blood cells. At the implant wound interface, the provisional matrix is formed, which then guides the regeneration of the tissue constructs [98]. Geometric characteristics like topography, degree of fitness, and smoothness of the surface are known to influence and be used to modify cellular responses like adhesion and proliferation at an early stage in healing [56].

By using a slicing design procedure, an implant with the tuneable micro-structural arrangement of deposition lines can be attained to guide cellular migration. Distance between the infill raster lines of the implant is controlled to attain specific porosities for each layer of the skin. Careful material selection yields the correct mechanical and structural properties native to each layer of the skin. Using the wound surface to slice the implant model (bottom-up approach) enhances the geometric fit of the interacting surface and avoids the area of voids caused by the stair casing effect.

The proposed method for free-form surface slicing is used to demonstrate the design of a skin implant with three different regions dedicated to the epidermis, dermis, and hypodermis. Figure 3-6 shows an example of the multi-layered design of a skin implant for wounds located on a hand model. The implant has a rectangular cross-section with measurements *of 15 mm x 10 mm* and a maximum thickness of 3 mm with three layered sections and a cover layer (see Figure 3-7(a)). The bottom/interfacing layer is

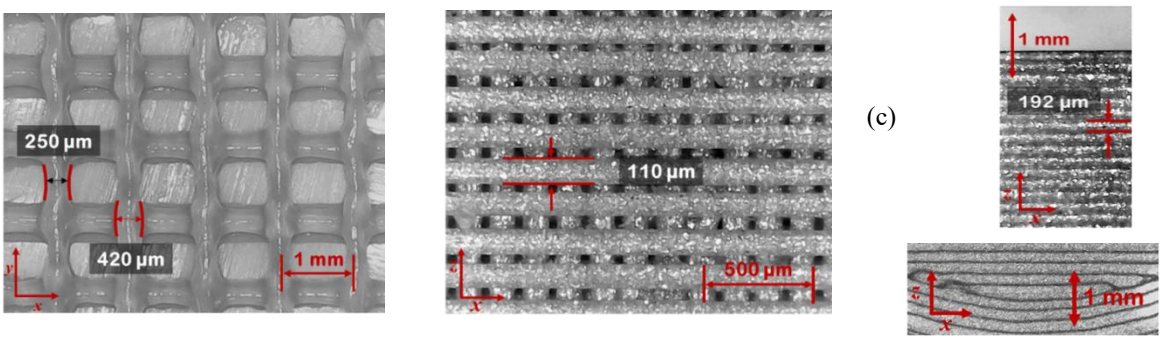

Figure 3-8: Printing quality and resolution assessment for the robotic bioprinter, (a) 35% Pluronic F-127 gel, image scaling 120 pixel/mm, mean linewidth 340 µm, pore size analysis: width: 717 ± 7 µm, max deviation: 42 µm, height: 618 ± 11 µm, max deviation: 60 µm, (b) Polymer printing, image scaling 330 pixel/mm, mean line width 110 µm, pore size analysis: width: 48.9 ± 3 µm, max deviation: 14.6 µm, height: 50 ± 3 µm, max deviation: 12 µm, (c) Mean layer height 192 µm, (d) Surface printed layer arrangement on a non-constant depth cross-section at a z-axis resolution of ~200 µm.

a free-form surface created to mimic the complex geometry encountered in the wound scenario. The wound model was created by subtraction of the wound with the hand model/face model was printed with a high-resolution resin printer and using CAD software a point cloud is generated to simulate scanning of the wound surface. This is done to replicate a practical workflow of the in-situ bioprinting of skin wounds. A surface fitted to the point cloud is used to slice the hypodermal (bottom or interacting) layer of the implant. Different surface profiles are used to slice the epidermis and dermis region. The top layer is sliced with the outer/top surface of the implant to enhance surface smoothness and fitting of the implant with respect to the wound site (see Figure 3-7(b)). A stiffer top layer will act like a cover to protect the softer layers of the implant beneath it. Moreover, since each layer, especially the top layer, is very thin, typically less than 0.5 mm (top layer), this would allow for only a few printing layers per section; for the top layer, it may even be one, depending on the bioprinter. In this scenario, planar slicing and printing become inefficient as the interlayer adhesion and geometric correctness become compromised. For the single-layer section, surface slicing is the only suitable strategy that replicates a complete section of skin in single-layer definitions. Another advantage of using surface slicing to create multi-layered skin implants is the interaction zone created in between epidermal, dermal, and hypodermal sections. The epidermal-to-dermal and dermal-to-hypodermal section interfaces can be designed to tune and facilitate cellular migration because these regions offer natural endpoints of biomaterial deposition lines with cells embedded coaxially. These interfaces are visible in the 2D cross-sectional view of the hand model with multi-layered slices corresponding to each skin layer presented in Figure 3-6.

3.4.4 In-Situ Bioprinting of Skin Implant on a Hand and Face Model

To facilitate the printing of biomaterial, a 4-degree-of-freedom robotic arm (Dobot) was customized. Ensuring precise in-situ positioning of the hand model in relation to the bioprinter was a critical task. A marker-based tracking and platform localization strategy was developed using imaging sensors and described in the methodology section. This enabled the measurement of the hand position in the workbench coordinate system, which was then utilized to transform and update the G-code coordinates in real time during printing. A marker-based tracking and platform localization strategy based on imaging sensors for in-situ placement of implant G-code was employed. This technique facilitated the accurate measurement of the hand position within the workbench coordinate system. These measurements were critical, as they were used to dynamically transform and update the G-code coordinates, thereby ensuring a seamless integration between the model and the bioprinter.

The bioprinter was verified by performing printing quality and resolution assessment for hydrogel and polymer printing. In summary, the printing performance specs are as follows. When printing with hydrogel (F-127), the linearity (max error/length) of the printed lines ranged between ± 0.1. The recorded line width of printed strands ranged between 0.25 and 0.42 mm. The polymer printing assessment conducted on the robotic bioprinter resulted in a line width of around ~100 μm ± 3 μm, and layer resolution was verified to be 192 μm. Layer resolution was also assessed in the case of a non-constant depth cross-section scenario. The printing assessment results are illustrated in Figure 3-8.

The surface slicing procedure developed was carefully assessed through its application in simulating the in-situ bioprinting of a skin implant model. This evaluation aimed not only to showcase the technique's versatility but also its capability to handle free-form surfaces adeptly. A complex non-planar deposition platform was devised by simulating a wound, measuring 0.6 mm in depth, on both a hand and a face model. The creation of the wound implant involved computing the intersection of the healthy skin surface and the simulated defect. This implant was subjected to slicing procedures incorporating diverse surface designs, aiming to test and validate the methodology's flexibility and adaptability. A fitting surface design for slicing the implant was chosen, which was subsequently used for toolpath computation and G-code generation, as detailed in Figure 3-3.

For the hand model, the implant was sliced to encompass a single surface, divided into three distinct layers, each measuring 0.2 mm in height. Figure 3-9 showcases the simulated G-code execution on the hand model while also depicting the successfully in-situ printed implant on the hand model. Similarly, for the face model, a total of three layers, each having distinct geometrical characteristics, as seen in

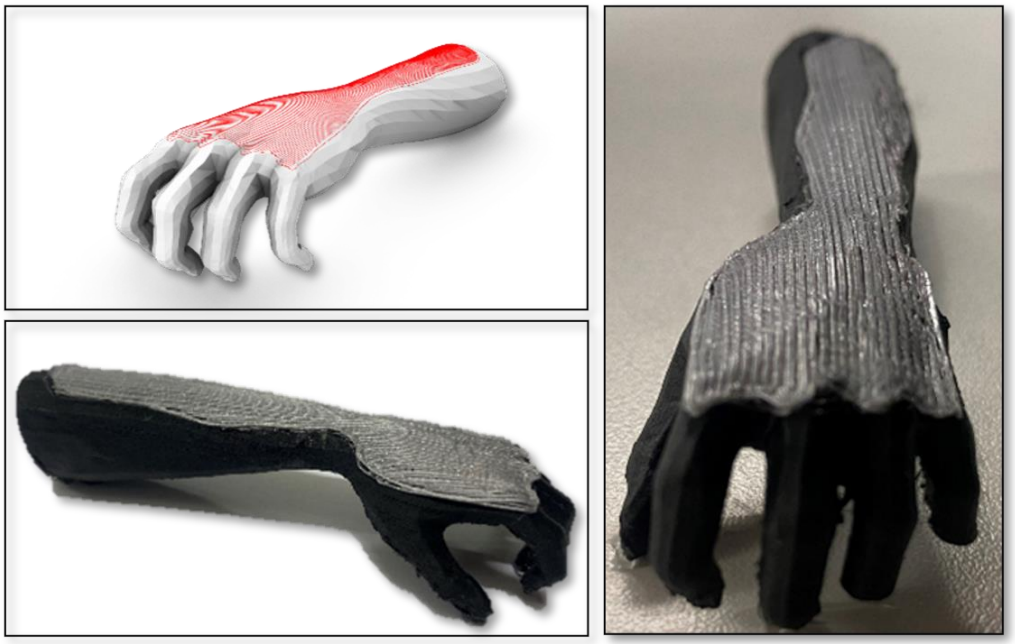

Figure 3-9: Demonstration of in-situ bioprinting using surface slicing and toolpath generation procedure on a hand model: simulated model, and final printed model.

Figure 3-10, were defined. The bottom two layers were printed using PLA, and the top layer was deposited using a hydrogel formulation. This biomaterial was composed of acellular gelatin methacryloyl (GelMA), using eosin Y as a photoinitiator. The toolpath generation considered various parameters, such as a line width of 0.4 mm, a deposition nozzle diameter of 0.4 mm, and a feeding tube diameter of 1.75 mm.

The top layers of the implant were accurately aligned with the exterior surfaces of both the hand and face models. A noteworthy observation was the absence of a staircase effect in the in-situ printed implants. This outcome signifies not only the efficiency of the free-form surface slicing but also suggests its potential applicability in future in-situ fabrication tasks.

3.5 Challenges and Limitations

In addressing the challenges faced in non-planar deposition, a few limitations and proposed improvement strategies must be acknowledged. The compatibility of materials poses a concern, as biomaterial s might struggle to adhere to curved or inclined surfaces; exploring different biomaterial formulations and additives could prove beneficial here. Achieving high resolution and a smooth surface finish on non-planar geometries is another challenge, but it can be mitigated by optimizing printing parameters and utilizing post-processing techniques. Additionally, the need to balance print speed with

structural stability is recognized, and real-time monitoring and feedback systems might be a solution. Moreover, ensuring uniform cooling or curing is crucial, and adjustable systems tailored to the geometry of the printed structure can be advantageous.

Software limitations pose another challenge but can be avoided through open-source collaborations or customized solutions. Concerns regarding calibration and error propagation can be addressed with advanced sensor systems and machine learning for real-time adjustments. The constraints of the printhead can limit printable structures, but versatile printheads can be an effective countermeasure. Positioning and localization are critical, and incorporating advanced sensors and computer vision can improve accuracy. Additionally, complex collision avoidance methods in path planning can be addressed by employing sophisticated algorithms. Lastly, improving the accessibility of printing surfaces can be achieved by designing robotic arms with an extended range of motion. Strategically addressing these limitations can pave the way for advancements in non-planar deposition in bioprinting.

In addition to the limitations previously acknowledged, specific constraints related to our hardware and algorithm impacting the performance of our non-planar deposition process are identified. These limitations are crucial for understanding the scope and potential applications of our methodology. The geometry of the print head, particularly in our hydrogel extrusion system, plays a pivotal role. A long conical-shaped nozzle (5 mm radius, 20 mm length) restricted the maximum printing depth at 15 mm. The clearance angle is approximately 70° with a 20° added clearance. For the polymer printing head, the maximum depth at which the nozzle can effectively print is limited to 5 mm, and it can handle surfaces inclined up to 30 degrees relative to the horizontal plane. The printing speed was fine-tuned

Figure 3-10: Demonstration of multi-material in-situ printed implant (i) simulated model, (ii) PLA in the base layer, and (iii) GelMA on the top layer.

to 300 mm/min, with a traveling speed of 1000 mm/min. The smallest layer height tested on the bioprinter is 0.1 mm, catering to the need for fine resolution in certain applications. A major limitation of the hardware is its limited degree of freedom. When printing on inclined surfaces, the print head remains aligned to the horizontal workspace. To fully harness the capabilities of surface slicing, a robotic printer with a higher degree of freedom is recommended. This would allow the printing nozzle to align with the normal direction of the surface, ensuring smoother finishes and preventing the smudging of printed lines. Another challenge is finding better localization strategies for positioning the platform onto the robotic workspace. The current approach accumulates errors when manually positioning and collecting the point cloud. Furthermore, more points are needed to achieve a better estimate of the pose transformation of the platform coordinate. This limitation highlights the need for more precise and automated methods in setting up and calibrating the printing process to enhance the overall accuracy and reliability of our non-planar deposition system.

3.6 Conclusions

In-situ approach to skin bioprinting, where the tissue construct is fabricated at the wound site, is a viable approach to future skin wound healing applications. In this process, slicing is an important step that creates the layers of tissue to be printed. Moving from planar slicing to surface slicing-based printing is a step forward in advancing the design-driven approach to designing bio-printed implants. This chapter describes an approach to the design of an implant through advanced surface slicing. Planar printing effects like stair-casing is avoided at the implant interface when an approximation of the native surface of the wound site is used as a slicing surface for the tissue implant geometry. Moreover, a multilayer slicing design and toolpath generation of a skin implant incorporating the epidermis, dermis, and hypodermis is proposed. The developed methodology was implemented on a customized robotic printer delivering biomaterial. The overall quality of the final printed product is also shared and is evidence of the superior finish of the exterior surface and the applicability of the methodology presented. Surface slicing makes it possible to design bio-printed skin implants with very thin and non-planar cross-sections. A proper slicing design of microstructural features specific to each layer and interaction zones within these dermis, epidermis, and hypodermis can facilitate regeneration at the cellular level.

Chapter 4 Autonomous Bioprinting on Moving Surfaces

Summary: Chapter 4 deals with the development and application of robotic systems designed for visual-controlled bioprinting on non-stationary surfaces. It begins with an overview of the challenges, followed by an examination of the working coordinate systems crucial for accurate bioprinting in robotic workspace. To deposit biomaterial on moving platforms, the integration of camera models for real-time tracking and adjustment through visual servo control mechanisms is presented. The implementation of the Kalman filter improves system predictability and response to environmental changes. An extensive experimental setup is described, leading to a detailed presentation of results and their implications for the field.

4.1 Introduction

The ability to print on moving surfaces holds immense potential across diverse applications. Among these, in-situ bioprinting is a prominent example where the capability to deposit biomaterials precisely on non-cooperative (moving) substrates can revolutionize advanced wound care solutions and regenerative medicine. Till now, in-situ bioprinting has targeted the direct fabrication of geometrically complicated biostructures or ‘implants’ on live platforms such as mice [233], sheep [234], and other biological entities [19]. These biostructures, when embedded with live cells, don't merely mimic the native tissue but initiate a host-mediated immunological regenerative response. Yet, the unique demands of such dynamic substrates highlight the limitations of conventional printing technologies in their respective fields. Traditional desktop-based 3D printers, for instance, are constrained by their inherent need for a stationary, planar platform [26]. In the context of a live host, where the deposition surface is unpredictable due to physiological motions, conventional technologies stumble. There's an evident requirement for advanced printing technologies capable of accommodating non-planar, shifting surfaces [235] [236]. This underlines the pressing need to evolve and integrate platform-independent printing methodologies that can adeptly cater to such dynamic scenarios.

While conventional 3D printing excels in producing performance-ready parts, its foundational methods are unsuitable for complex, on-site fabrications, such as bioprinting intricate geometries directly on living organisms [148] [234] [19]. These applications expose the inadequacies of static printing platforms when faced with the unpredictability of physiological movements [20], [26], [235], [236].

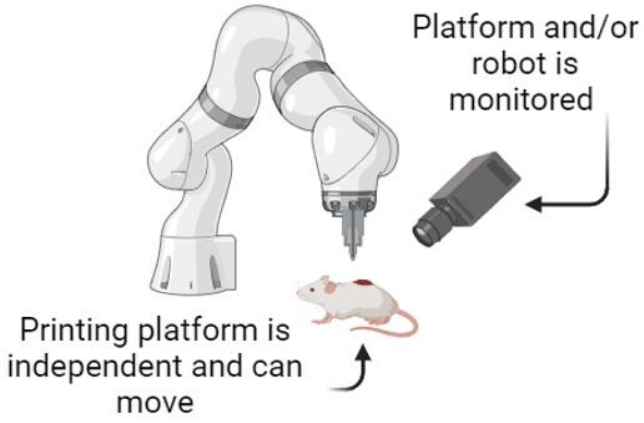

Figure 4-1: 3D Printing methodology tailored for free-form fabrication on non-cooperative platforms.

Addressing the limitations of traditional 3D printing technologies, which are tailored for stationary and planar platforms and falter in the face of the unpredictability inherent in physiological movements, is crucial. Anticipated advancements are likely to stem from robotic enhancements, following a trajectory similar to that seen in surgical applications [195], [198]. Advancements in adaptive 3D printing have begun to shift the trend by integrating robotics and computer vision [186]. Yet, these innovations have primarily addressed only a subset of the challenges, often restricting applications to simple geometries due to limitations in alignment, reference frame synchronization, and control strategies [185].

This chapter paper develops the potential of enhancing a robotic 3D printer's ability to precisely track and adapt to non-stationary targets/platforms (see Figure 4-1). This enhancement is facilitated by developing sophisticated visual servo control mechanisms [199]. Central to our approach is a computer-vision-based tracker designed to counterbalance platform motion throughout the printing process. The framework underlying this tracking strategy and its integration with the printing workflow is detailed. To gauge the efficacy of our visual tracking and feedback control system, evaluations were conducted by printing basic three-dimensional geometries on a 2D non-cooperative surface. Sections 4.2-4.5 outline the framework developed for the tracking approach, elaborating on its incorporation into the printing process. Finally, Sections 4.6 & 4.7 provide a comprehensive experimental analysis and discussion of our test platform, and a demonstration of the efficacy of our tracking algorithm through empirical results is provided, validating our system's performance in challenging printing scenarios.

4.2 Working Frame of References

Several frames of reference are needed to conduct quantitative analysis in a robot controlling operation with visual sensors. These frames of reference are illustrated in Figure 2-1. The camera coordinates the frame $\boldsymbol{\mathcal{F}}_C$ serves as an egocentric view and is located at the camera location. In the real image frame of reference $\boldsymbol{\mathcal{F}}_I$, the 3D point '**S**' is projected onto the real image plane at coordinates as ${}^{I}\mathbf{S}$ with coordinates ${}^{\boldsymbol{I}}[x, y, z]$. In the pixel frame $\boldsymbol{\mathcal{F}}_P$, each pixel is attached to a pixel coordinate, so the point ${}^{P}\mathbf{S}$ is expressed in $[u, v]$, which denotes the integer row and column of the pixel. The object frame of reference $\boldsymbol{\mathcal{F}}_O$ is located on the printing platform and needs tracking. Each point on the platform is known through its CAD file and is updated in real-time once tracked. These coordinates are transformed to the main world coordinate reference (denoted by $\boldsymbol{\mathcal{F}}_w$), which contains the manipulator's body. Additionally, we require a frame of reference attached to the robotic printer's printing nozzle (denoted by $\boldsymbol{\mathcal{F}}_E$).

Any point **P** with respect to the world coordinate frame is represented by the notation, ${}^{W}\mathbf{P}$. World coordinates are converted to target object coordinates given the *pose* between the frames of references denoted by ${}^{o}x_{W}$. The *pose* consists of a rotation matrix, ${}^{o}\boldsymbol{R}_{W}$, which represents the orientation of the world frame with respect to the object frame and a translation vector ${}^{o}\mathbf{t}_{W}$, specifying the origin of the world frame with respect to the object's frame of reference. Our work assumes the world reference frame when the leading superscript is not specified. Mathematically, this transformation can be represented as follows:

$$ {}^{o}\mathbf{P} = {}^{o}x_{W}({}^{W}\mathbf{P}) \tag{4-1} $$

$$ {}^{o}\mathbf{P} = {}^{o}\mathbf{R}_{W}\,{}^{W}\mathbf{P} + {}^{o}\mathbf{t}_{W} \tag{4-2} $$

In matrix notation, this equation can be written as a homogenous transformation as follows.

$$ \begin{pmatrix} {}^{o}\mathbf{P} \\ 1 \end{pmatrix} = \begin{pmatrix} {}^{o}\mathbf{R}_{W} & {}^{o}\mathbf{t}_{W} \\ 0^{T} & 1 \end{pmatrix} \begin{pmatrix} {}^{W}\mathbf{P} \\ 1 \end{pmatrix} \tag{4-3} $$

where,

$$ {}^{o}\mathbf{T}_{W} = \begin{pmatrix} {}^{o}\mathbf{R}_{W} & {}^{o}\mathbf{t}_{W} \\ 0^{T} & 1 \end{pmatrix} \tag{4-4} $$

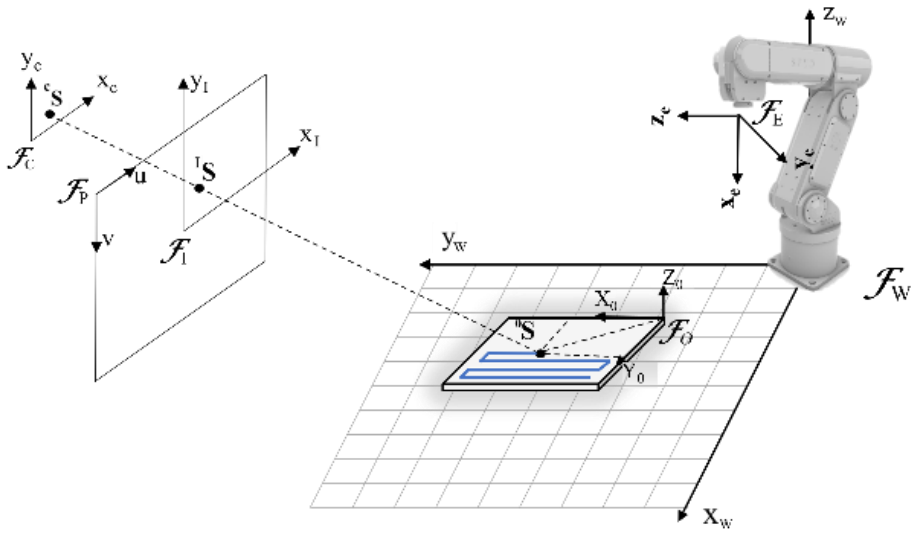

Figure 4-2: Different working frames of reference for visual feedback-based robotic printing. The task for the controller is to update the transformation matrices for these frames of reference in real time based on the pose of the platform.

This homogeneous transformation matrix converts points in the world frame to the object frame of reference; its inverse will transform from the object to the world frame of reference.

$$ {}^{o}\mathbf{T}_{w}^{-1} = {}^{w}\mathbf{T}_{o} = \begin{pmatrix} {}^{o}\mathbf{R}_{W}^{T} & -{}^{o}\mathbf{R}_{W}^{T}\,{}^{o}\mathbf{t}_{W} \\ 0^{T} & 1 \end{pmatrix} \quad 4\text{-}5 $$

The robotic manipulator is assigned to operate within one or more frames of reference. For example, the visual sensor provides target coordinates in the camera frame, while the printing module prints within the object frame of reference. Simultaneously, the manipulator receives positioning coordinates in the end-effector frame of reference. The primary objective of the visual tracker is to detect the platform and update the necessary transformations between these frames of reference. This enables the robotic manipulator to mimic the platform's motion and perform the printing operation in parallel. These capabilities are achieved through techniques developed in visual servoing, which are explained later in Section 4.4.

4.3 Camera Model and Integration

The coordinate conversion from the world frame of reference $\boldsymbol{\mathcal{F}}_{w}$ to the camera frame of reference $\boldsymbol{\mathcal{F}}_{C}$, can be summarized through the following transformation.

$$ {}^{C}X = {}^{C}\boldsymbol{T}_{W}\,{}^{W}X \quad 4\text{-}6 $$

here the matrix ${}^{C}T_{W}$, consists of numerous transformations that include the projection of the 3D scene onto the 2D image plane and then to the camera frame, followed by the rotation and translation that sets the camera into the world frame. This section presents the projection model used to derive this transformation.

The robotic manipulator's control relies on feedback information provided by the visual sensor, so it is essential to understand the geometric characteristics of image processing. From a fundamental point of view, a camera is a device that contains a lens that projects a 3D scene onto a 2D image plane. Some additional information can retrieve the loss of the depth data associated with each pixel from multiple sensors, multiple views of the target, or a predetermined relationship between several target points. The most widely used models to describe image formation include perspective projection, orthographic projection, and affine projection.

We assume the lens to the center as the origin of $\boldsymbol{\mathcal{F}}_{C}$, and *f* as the camera's focal length. Under the perspective transform, the world coordinates (*X, Y, Z*) are projected onto the image plane as (*x, y*). Using similar triangles, this can be described as:

$$\frac{-x}{X} = fZ \tag{4-7}$$

If the origin is moved to the image plane, the perspective projection is defined by the following relation:

$$x = \frac{fX}{f - Z} \tag{4-8}$$

Similarly, the y-coordinate in $\boldsymbol{\mathcal{F}}_{C}$ is given by:

$$y = \frac{fY}{f - Z} \tag{4-9}$$

A complete perspective camera model is typically presented like this:

$${}^{C}X = K[R\ t]{}^{W}X = {}^{C}\boldsymbol{T}_{W}\,{}^{W}X \tag{4-10}$$

This can be expressed in detail as follows:

$${}^{C}X = \begin{bmatrix} f_u & s & c_u \\ 0 & f_v & c_v \\ 0 & 0 & 0 \end{bmatrix} \begin{bmatrix} 1 & 0 & 0 & 0 \\ 0 & 1 & 0 & 0 \\ 0 & 0 & 1 & 0 \end{bmatrix} \begin{bmatrix} \boldsymbol{R_{3x3}} & \boldsymbol{t_{3x1}} \\ 0_{1x3} & 1 \end{bmatrix} \begin{bmatrix} {}^{W}X \\ 1 \end{bmatrix} \tag{4-11}$$

This equation is composed of two parts and can be referred to as the extrinsic and intrinsic parts of the camera model. The extrinsic part comprises the Euclidean transformation from $\boldsymbol{\mathcal{F}}_{w}$ to $\boldsymbol{\mathcal{F}}_{C}$ and the

perspective projection from 3D to 2D ([$R\ t$]). By combining the perspective projection and Euclidean transformation, we can arrive at the extrinsic part of the camera model:

$$[R\ t] = \begin{bmatrix} 1 & 0 & 0 & 0 \\ 0 & 1 & 0 & 0 \\ 0 & 0 & 1 & 0 \end{bmatrix} \begin{bmatrix} R & t \\ 0 & 1 \end{bmatrix} \quad 4\text{-}12$$

The intrinsic matrix part of the perspective camera model is denoted by 'K' and represents the transformation from the image plane to the camera's frame of reference. This matrix is a homogeneous matrix commonly known as the camera calibration matrix. Elements of the calibration matrix include the optical center (c_u, c_v), the skew parameter s is required to describe the non-orthogonal structure of the detector array with respect to the optical axis, and parameters f_u and f_v are scaled focal length f. Before the visual servoing task, calibration of visual sensors must be performed. In this process, the intrinsic and extrinsic parameters of the camera are determined by observing known features in the image plane [237]. Camera calibration is an open research topic, and several methods for precise calibration are presented in [206].

4.4 Visual Servo Control Mechanisms

Visual servoing systems can typically be classified by camera configuration; either the camera is mounted on the robotic manipulator (eye-in-hand configuration) or in the world frame observing the object and the robot. In an eye-in-hand type setup, the camera frame is attached to the end effector frame; thus, the transformation changes with the robotic movement. The second configuration, the eye-to-hand, has the camera fixed in the workspace. In this case, the image coordinates of the target are independent of the robotic motion.

Visual servoing systems can also typically be classified by control type. In image-based visual servoing (IBVS), the controller is designed based on directly extracted features from the image. Pose-based visual servoing (PBVS) involves estimating the target's pose, which is extracted from the image features in conjunction with its geometric model (see Figure 4-3). A visual servoing control scheme's basic component minimizes an error function **e**(t). Let us define the kinematic error function as the relative difference between the pose vector of the printing nozzle **P** and a stationing point **S** on the deposition platform, both expressed in the world frame $\boldsymbol{\mathcal{F}}_W$ as;

$$\mathbf{e}(t) = \mathbf{P} - \mathbf{S} \quad 4\text{-}13$$

Note that $\widehat{\boldsymbol{S}}_{\mathrm{P}}$ estimates the stationing point's current position observed in the image frame, which can be expressed with respect to $\boldsymbol{\mathcal{F}}_W$ by knowing the camera pose and calibration metrics ($\widehat{\boldsymbol{S}}_{\mathrm{P}} =$

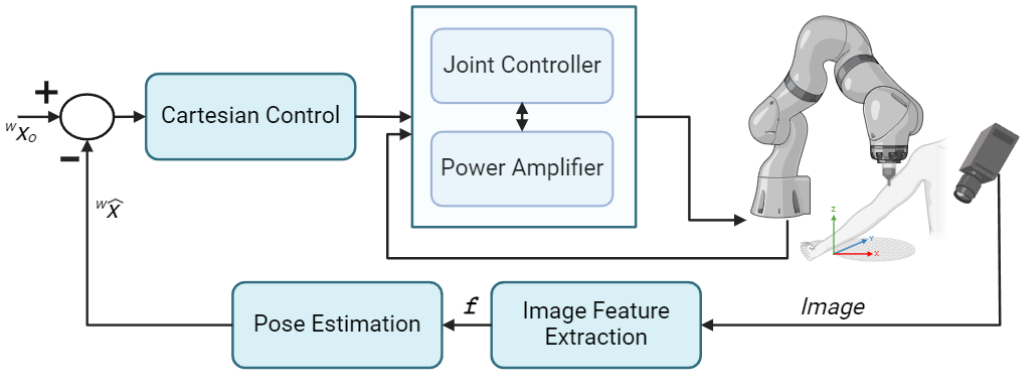

Figure 4-3: Fixed camera visual servo control architecture for position-based look and move operation.

${}^{W}x_{C} \,.\, {}^{C}x_{I} \,.\, {}^{I}\boldsymbol{S}$). **P** can be integrated through the kinematic transformations that relate the indicated values in the robot's joint space to the end effector frame of reference. In this case, the system observes only the target and can be referred to as an Endpoint Open-Loop (EOL) system. Furthermore, the EOL system can be converted to an Endpoint Closed-Loop (ECL) system if the systems observe the platform and printing nozzle [237]. In this case, ${}^{I}\boldsymbol{P}$ goes through several transformations and can be expressed as $\widehat{\boldsymbol{P}}_{S} = {}^{W}x_{C} \,.\, {}^{C}x_{I} \,.\, {}^{I}\boldsymbol{P}$. Equation 4-13 in the case of EOL and ECL takes the following form:

$$\mathbf{e}(t) = {}^{W}x_{E}\,{}^{E}\mathbf{P} - {}^{W}x_{C} \cdot {}^{C}x_{I} \cdot {}^{I}\mathbf{S} \qquad 4\text{-}14$$

$$\mathbf{e}(t) = {}^{W}x_{C} \cdot {}^{C}x_{I} \cdot {}^{I}\boldsymbol{P} - {}^{W}x_{C} \cdot {}^{C}x_{I} \cdot {}^{I}\boldsymbol{S} \qquad 4\text{-}15$$

Let us consider that the robot task space is restricted to $\Re^3$ as a rigid link that constrains the pose of the printing nozzle relative to the platform. In this case, the robotic manipulator's control input is the desired transitional velocity. A proportional regulator control is applied to drive the system to an equilibrium state of zero kinematic error:

$$u = -k\,({}^{W}\hat{x}_{E}\,{}^{E}\boldsymbol{P} - {}^{W}\hat{x}_{C}\,{}^{C}\boldsymbol{S}) \qquad 4\text{-}16$$

Here, '*k*' is the *proportional* feedback constant greater than zero. Also, Equation 4-16 is based on EOL system configuration. This can be converted into an ECL system by the visual system observing both the printing nozzle and the platform. In this case, Equation 4-16 becomes:

$$u = -k\,({}^{W}\hat{x}_{C}\,{}^{C}\boldsymbol{P} - {}^{W}\hat{x}_{C}\,{}^{C}\boldsymbol{S}) = -k\,{}^{W}\hat{x}_{C}\,({}^{C}\boldsymbol{P} - {}^{C}\boldsymbol{S}) \qquad 4\text{-}17$$

4.5 Implementation of the Kalman Filter

Before describing the implementation of the extended Kalman filter, let's understand the need for such a prediction algorithm. Sensors like cameras and stereo techniques map the precise position of the target object. Most modern visual sensors like USB webcam and firewire cameras output data at a rate of up to 100 fps. This restricts the control algorithm's timing to match the cameras' data rate output. Moreover, the uncertainty in the observation related to hardware and software factors is essential.

The target's velocity and acceleration can be estimated by measuring the position at each frame. Newton's equation of motion can be easily used to predict the object's future position. In between the measurements, the robotic arm tracks the position of the target based on the estimated acceleration and velocity. Upon receiving the new observation, the model is updated by considering the uncertainty in the measuring and estimation process.

Using Newton's second law as a basis and assuming constant acceleration, the position of an object in three-dimensional space over time can be estimated with the following kinematic equations:

$$\begin{cases} x = x_0 + \dot{x}\Delta t + \frac{1}{2}\ddot{x}\Delta t^2 \\ y = y_0 + \dot{y}\Delta t + \frac{1}{2}\ddot{y}\Delta t^2 \\ z = z_0 + \dot{z}\Delta t + \frac{1}{2}\ddot{z}\Delta t^2 \end{cases} \quad 4\text{-}18$$

Here, the system's state is the target parameters [x, y, z, $\dot{x}$, $\dot{y}$, $\dot{z}$, $\ddot{x}$, $\ddot{y}$, $\ddot{z}$]. The state variables are inputted into the prediction algorithm. The above set of equations describing the relationship between input and output can be referred to as the state space model. Assuming a small time increment and constant acceleration in each increment, the extrapolated state at time n:

$$\begin{cases} \hat{x}_{n+1,n} = \hat{x}_{n,n} + \hat{\dot{x}}_{n,n}\Delta t + \frac{1}{2}\hat{\ddot{x}}_{n,n}\Delta t^2 \\ \hat{y}_{n+1,n} = \hat{y}_{n,n} + \hat{\dot{y}}_{n,n}\Delta t + \frac{1}{2}\hat{\ddot{y}}_{n,n}\Delta t^2 \\ \hat{z}_{n+1,n} = \hat{z}_{n,n} + \hat{\dot{z}}_{n,n}\Delta t + \frac{1}{2}\hat{\ddot{z}}_{n,n}\Delta t^2 \\ \hat{\dot{x}}_{n+1,n} = \hat{\dot{x}}_{n,n} + \hat{\ddot{x}}_{n,n}\Delta t \\ \hat{\dot{y}}_{n+1,n} = \hat{\dot{y}}_{n,n} + \hat{\ddot{y}}_{n,n}\Delta t \\ \hat{\dot{z}}_{n+1,n} = \hat{\dot{z}}_{n,n} + \hat{\ddot{z}}_{n,n}\Delta t \\ \hat{\ddot{x}}_{n+1,n} = \hat{\ddot{x}}_{n,n} \\ \hat{\ddot{y}}_{n+1,n} = \hat{\ddot{y}}_{n,n} \\ \hat{\ddot{z}}_{n+1,n} = \hat{\ddot{z}}_{n,n} \end{cases} \quad 4\text{-}19$$

The general form of the state extrapolation equation in the matrix form is

$$\hat{\boldsymbol{x}}_{+1,n} = \boldsymbol{F}\hat{\boldsymbol{x}}_{n,n} + \boldsymbol{G}\boldsymbol{u}_n + \boldsymbol{w}_n \tag{4-20}$$

Here, $\hat{x}_{n+1,n}$ is the predicted state of the platform or the tracking object, $\hat{x}_{n,n}$ is the estimated state at time step n, $\boldsymbol{u}_n$ is the control or input variable, which is an input to the system that is measurable, w_n is the process-related noise that is not measurable, $\boldsymbol{F}$ is the state transition matrix, $\boldsymbol{G}$ is the control matrix that maps the control to uncertainty in the x coordinate measurement. The state variables. To develop the extended Kalman filter for the case of the robotic printer, we consider the control input to be the acceleration vector measured directly from the printing platform. In this case, we have additional information based on the actual movement of the platform. Thus, the state extrapolation model can be described as:

$$\begin{bmatrix} \hat{x}_{n+1,n} \\ \hat{y}_{n+1,n} \\ \hat{z}_{n+1,n} \\ \hat{\dot{x}}_{n+1,n} \\ \hat{\dot{y}}_{n+1,n} \\ \hat{\dot{z}}_{n+1,n} \end{bmatrix} = \begin{bmatrix} 1 & 0 & 0 & \Delta t & 0 & 0 \\ 0 & 1 & 0 & 0 & \Delta t & 0 \\ 0 & 0 & 1 & 0 & 0 & \Delta t \\ 0 & 0 & 0 & 1 & 0 & 0 \\ 0 & 0 & 0 & 0 & 1 & 0 \\ 0 & 0 & 0 & 0 & 0 & 1 \end{bmatrix} \begin{bmatrix} \hat{x}_{n,n} \\ \hat{y}_{n,n} \\ \hat{z}_{n,n} \\ \hat{\dot{x}}_{n,n} \\ \hat{\dot{y}}_{n,n} \\ \hat{\dot{z}}_{n,n} \end{bmatrix} + \begin{bmatrix} 0.5\Delta t^2 & 0 & 0 \\ 0 & 0.5\Delta t^2 & 0 \\ 0 & 0 & 0.5\Delta t^2 \\ \Delta t & 0 & 0 \\ 0 & \Delta t & 0 \\ 0 & 0 & \Delta t \end{bmatrix} \begin{bmatrix} \ddot{x}_n \\ \ddot{y}_n \\ \ddot{z}_n \end{bmatrix} \tag{4-21}$$

Next, the generalized observation model in the matrix form is given by:

$$\boldsymbol{z}_n = \boldsymbol{H}\boldsymbol{x}_n + \boldsymbol{v}_n \tag{4-22}$$

$$\begin{bmatrix} x_{n,\,measured} \\ y_{n,\,measured} \\ z_{n,\,measured} \end{bmatrix} = \begin{bmatrix} 1 & 0 & 0 & 0 & 0 & 0 \\ 0 & 1 & 0 & 0 & 0 & 0 \\ 0 & 0 & 1 & 0 & 0 & 0 \end{bmatrix} \begin{bmatrix} x_n \\ y_n \\ z_n \\ \dot{x}_n \\ \dot{y}_n \\ \dot{z}_n \end{bmatrix} \tag{4-23}$$

Here, $\boldsymbol{z}_n$ is the observation vector, $\boldsymbol{H}$ is the observation matrix, $\boldsymbol{x}_n$ is the system state matrix, and $\boldsymbol{v}_n$ is the noise vector related to measurement. Process-related noise matrix Q is evaluated by projecting the variance in acceleration σ^2 onto the state transition matrix from the state-space model.

$$\boldsymbol{Q} = \boldsymbol{G}\sigma_a^2\boldsymbol{G}^T \tag{4-24}$$

$$\boldsymbol{Q} = \sigma_a^2 \begin{bmatrix} \frac{\Delta t^4}{4} & 0 & 0 & \frac{\Delta t^3}{2} & 0 & 0 \\ 0 & \frac{\Delta t^4}{4} & 0 & 0 & \frac{\Delta t^3}{2} & 0 \\ 0 & 0 & \frac{\Delta t^4}{4} & 0 & 0 & \frac{\Delta t^3}{2} \\ \frac{\Delta t^3}{2} & 0 & 0 & \Delta t^2 & 0 & 0 \\ 0 & \frac{\Delta t^3}{2} & 0 & 0 & \Delta t^2 & 0 \\ 0 & 0 & \frac{\Delta t^3}{2} & 0 & 0 & \Delta t^2 \end{bmatrix} \quad 4\text{-}25$$

The measurement noise is assumed to be described by a zero-mean Gaussian distribution with covariance matrix **R**. It is also assumed that the *x, y, and z* values are uncorrelated.

$$\boldsymbol{R_n} = \begin{bmatrix} \sigma_{x_m}^2 & 0 & 0 \\ 0 & \sigma_{y_m}^2 & 0 \\ 0 & 0 & \sigma_{z_m}^2 \end{bmatrix} \quad 4\text{-}26$$

Here, σ_{xm}^2 refers to the measurement uncertainty in the *x*-coordinate measurement.

The Kalman filtering process starts with an initial estimate of state and covariance matrix **F**. At each time step, a predicted state and uncertainty are computed through the extrapolation model is computed based on the Equation 4-20. Next, the predicted states and uncertainty are corrected based on the observations and the measuring devices' associated covariances. The equations associated with both steps are summarized below.

$$\begin{gathered} Prediction\ Step \\ \hat{\boldsymbol{x}}_{n+1,n} = \boldsymbol{F}\hat{\boldsymbol{x}}_{n,n} + \boldsymbol{G}\boldsymbol{u}_n \\ P_{n+1,n} = FP_{\boldsymbol{n,n}}\boldsymbol{F^T} + Q \end{gathered} \quad 4\text{-}27$$

$$\begin{gathered} Correction\ Step \\ \boldsymbol{K}_n = \boldsymbol{P}_{n,n-1}\boldsymbol{H}^T\left(\boldsymbol{H}\boldsymbol{P}_{n,n-1}\boldsymbol{H}^T + \boldsymbol{R}_n\right)^{-1} \\ \hat{x}_{n,n} = \hat{x}_{n,n-1} + \boldsymbol{K}_n\left(z_n - \boldsymbol{H}\hat{x}_{n,n-1}\right) \\ \boldsymbol{P}_{n,n} = (\boldsymbol{I} - \boldsymbol{K}_n\boldsymbol{H})\,\boldsymbol{P}_{n,n-1}\,(\boldsymbol{I} - \boldsymbol{K}_n\boldsymbol{H})^T + \boldsymbol{K}_n\boldsymbol{R}_n\boldsymbol{K}_n^T \end{gathered} \quad 4\text{-}28$$

Here, $\mathbf{K}_n$ is the Kalman gain at a given time step. Since the initial pose of the target is unknown, an inappropriate estimate can lead to poor convergence of the Kalman filter. To improve the performance, the detected position of the target, as retrieved from the camera, is used as the initial estimate. In our application of the Kalman filter, a simplified motion model is used and validated against empirical data to estimate acceleration, ensuring reliability despite the absence of detailed system dynamics derivation.

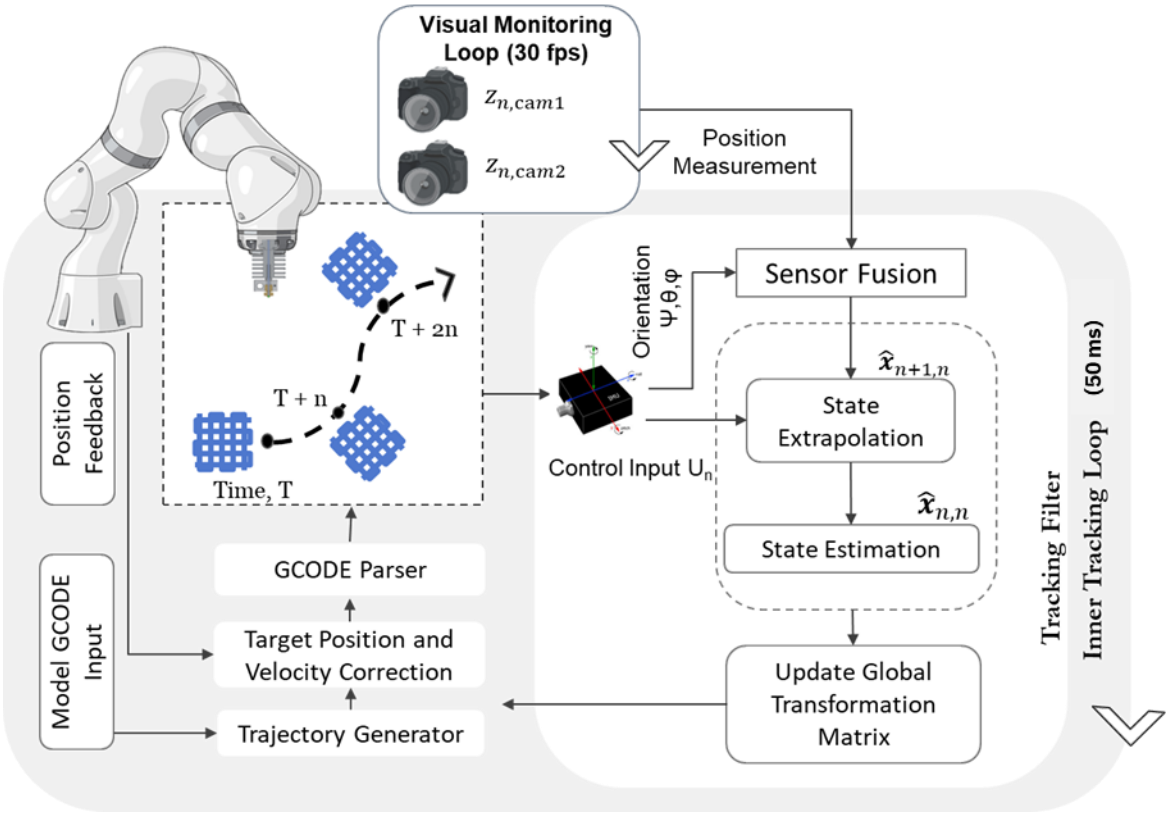

Figure 4-4: Visual servo control architecture for the position-based look, move tracking, and printing operation.

In handling acceleration within a Kalman filter model under a constant acceleration assumption, there are two primary approaches. When used as part of the state model, acceleration is explicitly included as a variable within the state model. This method offers more precise tracking but requires a deeper understanding of these dynamics. Alternatively, deviations from constant acceleration can be treated as part of the process noise. This approach simplifies the model by treating unexpected changes in acceleration as random variations, which may lead to underestimations of the system's dynamics but simplifies computation. Choosing between these approaches depends on the frequency and magnitude of acceleration changes; frequent or significant changes favor a more complex state model, while infrequent, minor changes may be adequately managed as noise (see Appendix B for implementation details).

4.6 Experimental Setup

The current experimental testing scenario follows: When the platform is stationary, the robotic printer can fabricate structures like any other 3D printer. The external platform produces uncooperative motion at a uniform velocity during printing. Currently, the visual sensor tracks the motions and compensates

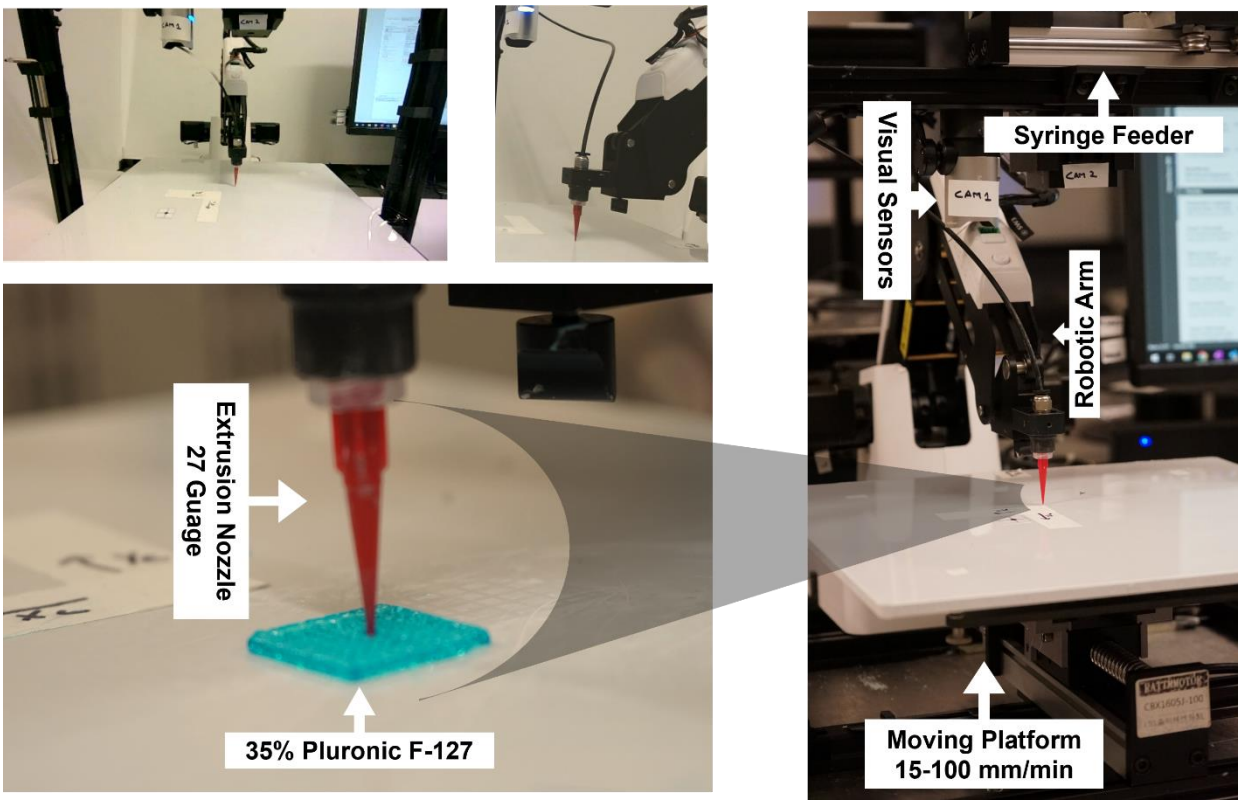

Figure 4-5: Experimental setup, robotic arm-based bioprinter with integrated visual sensor and a fully tracked platform.

for this motion in parallel to the printing process. The overall printing and control software architecture can be visualized in Figure 4-4.

Positioning System: The experimental demonstration was carried out using a low-cost, off-the-shelf 4-axis robotic manipulator (Dobot Magician) (Figure 4-5). This product is marketed with a repeat position accuracy of 0.25 mm, a rated payload of 500 g, an arm length of 320 mm, and a maximum speed when moving in a straight line of 800 mm/s. This arm has an integrated motor controller that can realize numerous motion functions, such as linear and arc interpolations. The motion of the manipulator is controlled by G-code programming sent from the computer via the serial interface. Each line of the G-code script indicates the target point and amount of material to be extruded. Since the command lines are sent to the printer sequentially, the printer has to wait for the first command to execute before reading the following command. Dobot Magician in the 3D printing mode allows for using the RepRap Marlin 3D printing framework and a communication protocol native to most commercial 3D printing devices.

Material Deposition System: The manipulator is integrated with a customized material extrusion subsystem to enable robotic 3D printing. These include a thermistor, heating block, cooling fan, stepper motor attachment for extruding polymer filament, and an alternate syringe dispensing system for hydrogel delivery. The extrusion system is controlled via Marlin open-source firmware originally developed for FDM (fused deposition modeling) based 3D printers through an Arduino micro-controller and RAMPS 1.4 breakout board for the Pololu stepper motor driver. The syringe dispenser consists of a NEMA 17 stepper motor and a 12 ml syringe holder attached to a precise ball screw linear stage actuator. The communication interface for this system is also via serial interface, and the control commands are scripted in G-code.

Visual Tracking: The visual system incorporates two cameras: a USB camera (Microsoft LifeCam Studio) that streams at a rate of 30 fps with a pixel resolution of 1920 x 1080 and a secondary 16 MP (ELF USB) camera. Both cameras are two-dimensionally calibrated using the perspective calibration model to the printing surface. Before calibration, the image undergoes thresholding and a particle filtering step. During tracking, the shift in the platform's position is determined by locating a marker within the image using the grayscale value pyramid algorithm. Supplementing this visual system is an inertial measurement unit (IMU) sensor affixed to the platform (for testing purposes). IMUs provide raw data on linear accelerations and angular velocities, which are fundamental for the accurate estimation of motion dynamics in three-dimensional space. These measurements are particularly valuable in environments where camera sensors might be limited by line-of-sight issues. Moreover, IMUs operate with high data rate outputs, allowing for real-time motion tracking. However, IMUs are prone to accuracy issues due to sensor drift, noise from thermal variations, electronic interference, and manufacturing flaws. Additionally, integrating acceleration data to calculate velocity and position can lead to cumulative errors. For our final demonstration, the deviations from the constant accelerations were treated as a part of the process noise as described in Section 4.5

Testing Platform: The platform consists of a flat surface mounted on a servo-controlled linear stage. This platform consists of high-accuracy encoders, and its positional data can be extracted. This controlled motion is used to validate the calibration of the visual sensors and assess the tracking performance. The platform runs independently of the robotic printing setup and produces motion to simulate an uncooperative platform having 1 degree of freedom. It can generate pulse response and periodic motion. At all times, the camera is tracking a marker located on the printing platform, which serves as the origin of the platform coordinate frame. The updated printing coordinates are obtained through knowledge of platform geometry and tracked motion when the platform is in motion.

Software Platform: The high-level visual servo controller is deployed as two loops running at different step times and sharing information (see Figure 4-4). The control loop generates positional control commands in G-code format. This loop implements the Kalman filter and updates the global transformation matrix and the model G-code on every loop iteration. The vision loop is run in parallel and implements the image acquisition and detection of the marker representing the platform's origin. The visual loop is limited to 30 Hz due to the response rate of the camera hardware. The control loop must send commands faster to maintain synchronization with the platform and printing action. In case the updated image measurements are unavailable, the control loop relies on the Kalman filter's prediction step, which continues to track the motion of the platform based on the last measurement received. When the image measurement is available, the tracking filter model is updated.

4.7 Results and Discussion

Figure 4-5 illustrates the components of the experimental setup. The printing platform is supported on a linear stage attached to the aluminum structure housing the printer. By rotating the linear stage relative to the robot pose produces a motion in 2 degrees of freedom. The vision system captures the motion of the platform, and motion compensation is applied to the printing process in real-time during printing. The prints are conducted with a linewidth of 0.3 mm, printing speed of up to 60 mm/min, and platform speed of up to 200 mm/min. Before conducting printing test on a moving platform, the tracking filter's performance and capabilities are assessed. Precision was evaluated by calculating the standard deviation of repeated position measurements, which was found to be 0.05 mm. Accuracy was

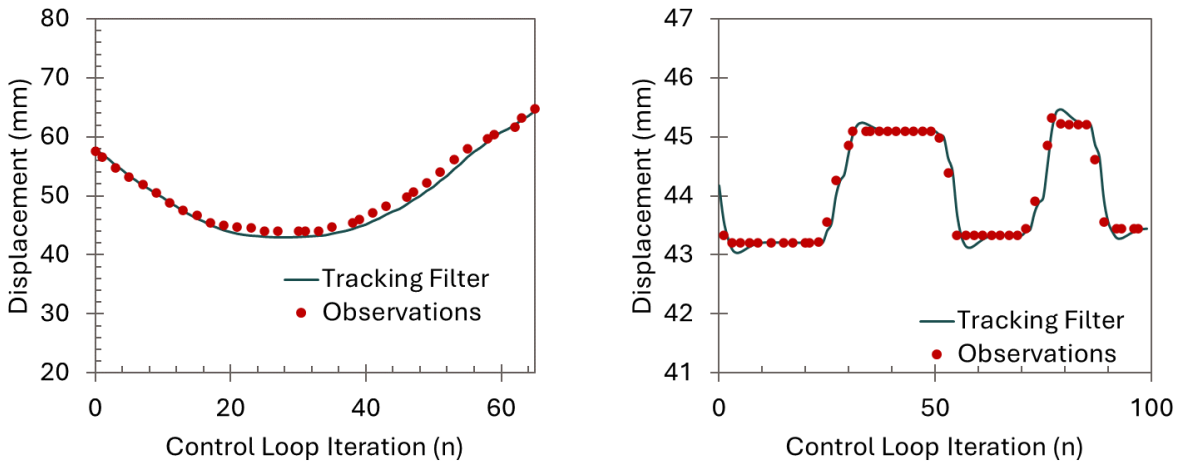

(a) (b)

Figure 4-6: (a) Visualization of Kalman filter output(blue) and observations input (red dot). (b) Performance of tracking filter output and observations input subjected to random motion. Filter output(blue) and observations input (red dot).

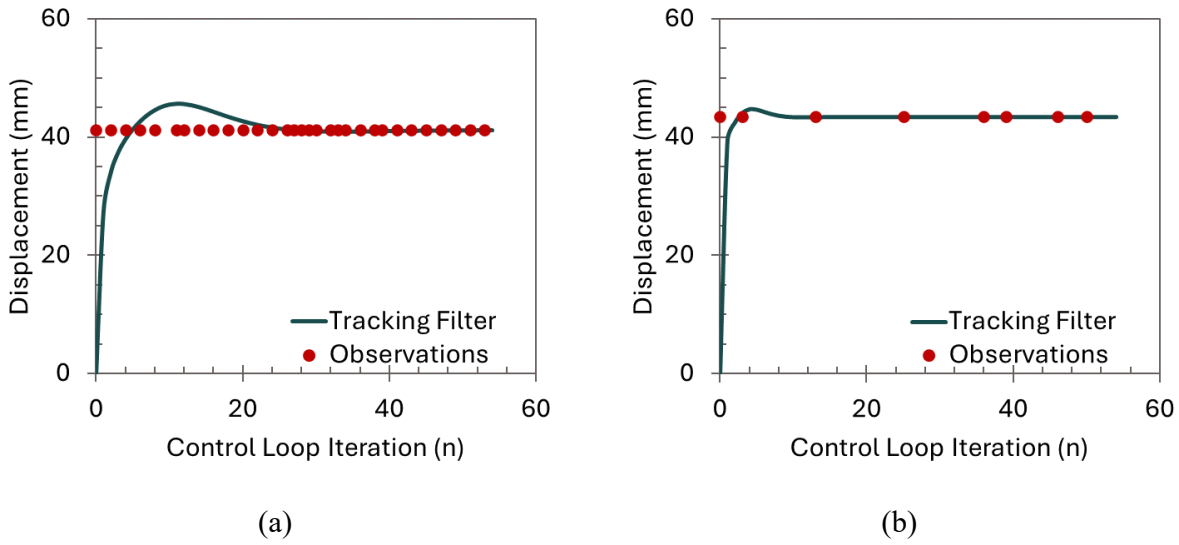

Figure 4-7: (a) Step response output with amplitude of 40 mm with T (control loop = 50 ms) ≤ 2T(visual loop = 50 to 100 ms), filter output(blue) and observations input (red dot). (b) Step response output with amplitude of 350 mm with T (control loop = 50 mm) ≤ 10 T (visual loop = 500ms). Filter output(blue) and observations input (red dot).

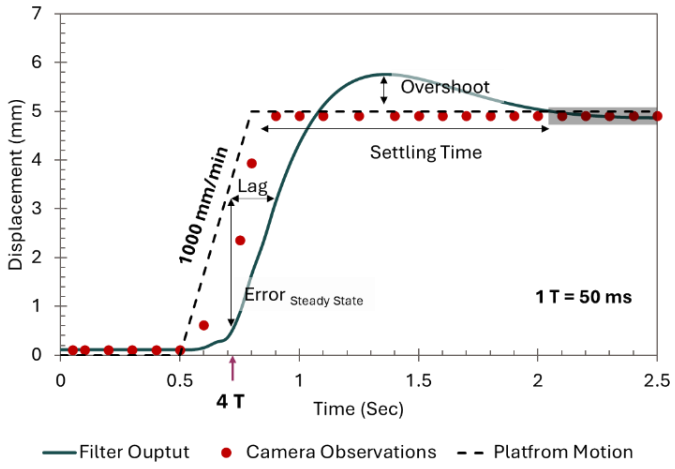

Figure 4-8: A typical response curve to ramp loading, demonstrating the system's ramp response at a platform speed of 1000 mm/min, with description of key performance metrics including lag, steady-state error, overshoot, and settling time, along with filter output and camera observations.

determined by the mean deviation from the true position, which was 0.1 mm, indicating high accuracy. Repeatability was assessed by the consistency of the robot's performance over multiple trials, with the robot consistently returning to within 0.05 mm of the target point. Both relative and absolute errors were considered to provide a comprehensive understanding of the system's performance. The error is a combination of platform localization error and relative error from tracking and robot positional error.

Figure 4-6(a), which shows the smooth output from the tracking filter in the presence of noisy measurements during a platform track. Similarly, Figure 4-6(b) shows the tracking filter performance when the platform is subject to random motion. This shows the reliable working of the software architecture presented in, satisfactory integration of hardware and ensuring accurate calibration of the printing workspace. Several calibration tests were conducted to ensure that the accurate capture of the platform movement.

The step response of the output in both cases is shown in Figure 4-7(a) and Figure 4-7(b). It can be concluded that in the first case, the model can converge and follow the target but with an abrupt step-like motion; this is due to the linear nature of the implemented Kalman filter. In the second case, this effect is reduced to produce a smooth output. As discussed, the control and visual loops are running at different loop timings due to hardware requirements. The visual loop was set to miss random measurement updates to test this system configuration and run two times slower than the control loop. Then, the visual loop was set up to run approximately at the same rate as the control loop while missing random data packets.

Platform Speed (mm/min)	Lag (s)	Steady State (mm)	Overshoot (mm)	Settling Time (s)	Positional Error (mm)
50	0.050	0.023	0.006	0.000	0.096
100	0.100	0.141	0.150	0.250	0.092
200	0.130	0.383	0.276	0.650	0.091
400	0.175	0.973	0.597	0.950	0.109
600	0.175	1.489	0.689	0.950	0.092
800	0.160	2.104	0.730	1.075	0.093
1000	0.215	2.970	0.760	1.150	0.092
1500	0.350	4.303	0.779	1.250	0.098
2000	0.350	3.595	0.750	1.250	0.095

Table 4-1: Performance metrics of bioprinting platform at varying speeds ranging from 50-2000 mm/min: lag, steady state, overshoot, settling time, and positional error analysis.

The design of bioprinter framework, which accommodates a tracking loop operating at a slower rate (100 ms) compared to the printer control loop (20 ms), presents several innovative aspects. By allowing

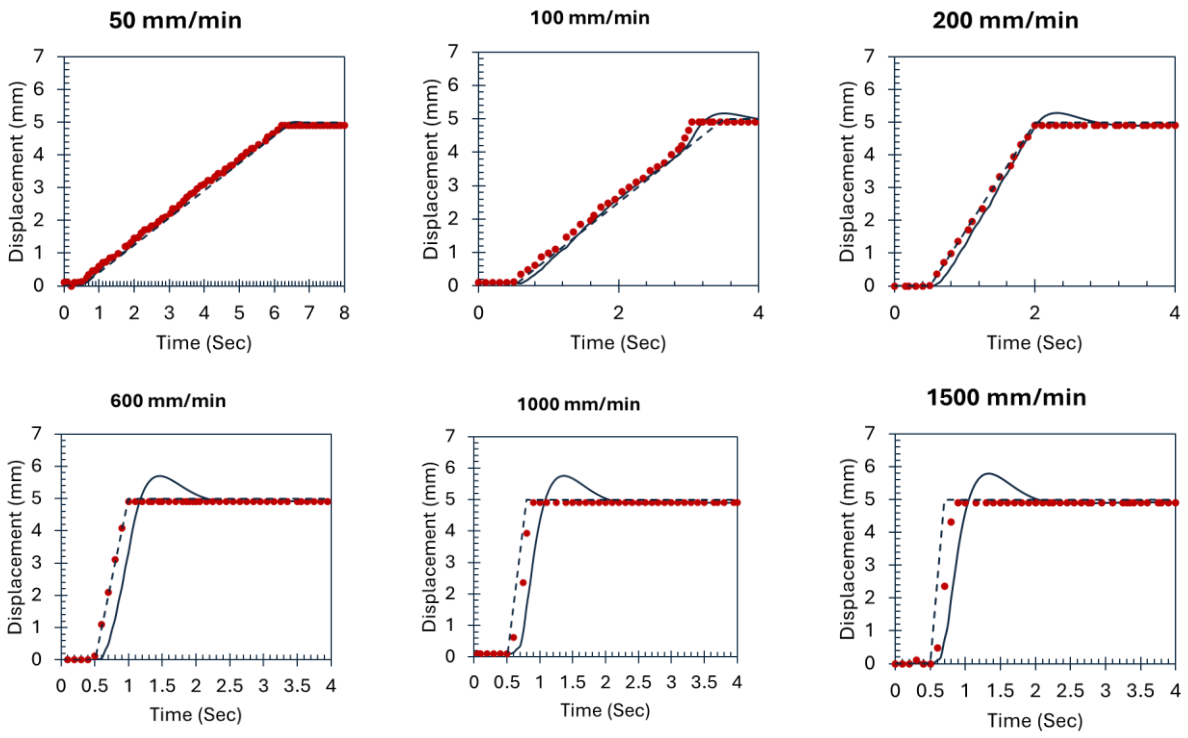

Figure 4-9: Ramp response of the control system at varying platform speeds, demonstrating the system's displacement over time. Each graph illustrates the system's response to a ramp type of loading at speeds ranging from 50 mm/min to 1500 mm/min.

these systems to operate asynchronously, the design efficiently utilizes the strengths of both the precision of slower camera tracking and the responsiveness of a faster printing control system. Despite the difference in operational speeds, the integration allows for real-time feedback between the tracking and printing processes. This can be particularly emphasized in applications where dynamic adjustments are crucial, such as printing on a moving platform or biological host. Highlighting how the printer can still react in real-time to positional changes detected by the camera at a different rate showcases the system's ability to adapt to the environment. The slower update rate in the tracking loop enables the implementation of advanced filtering algorithms, such as Kalman filters or moving averages, which can smooth out the noise by considering previous and current observations. This results in generating more stable and reliable tracking output. Meanwhile, operating at a higher frequency, the printer control loop can utilize this filtered, less noisy data to make precise and minute adjustments more frequently. This setup ensures that the bioprinting process remains stable and accurate, even in noise. Moreover, high latency can lead to a lag between the actual position of the moving target and its perceived position, resulting in inaccuracies and potential printing errors. In the developed framework, while the tracking loop operates with inherent delays, the faster printer control loop helps mitigate the impact of this

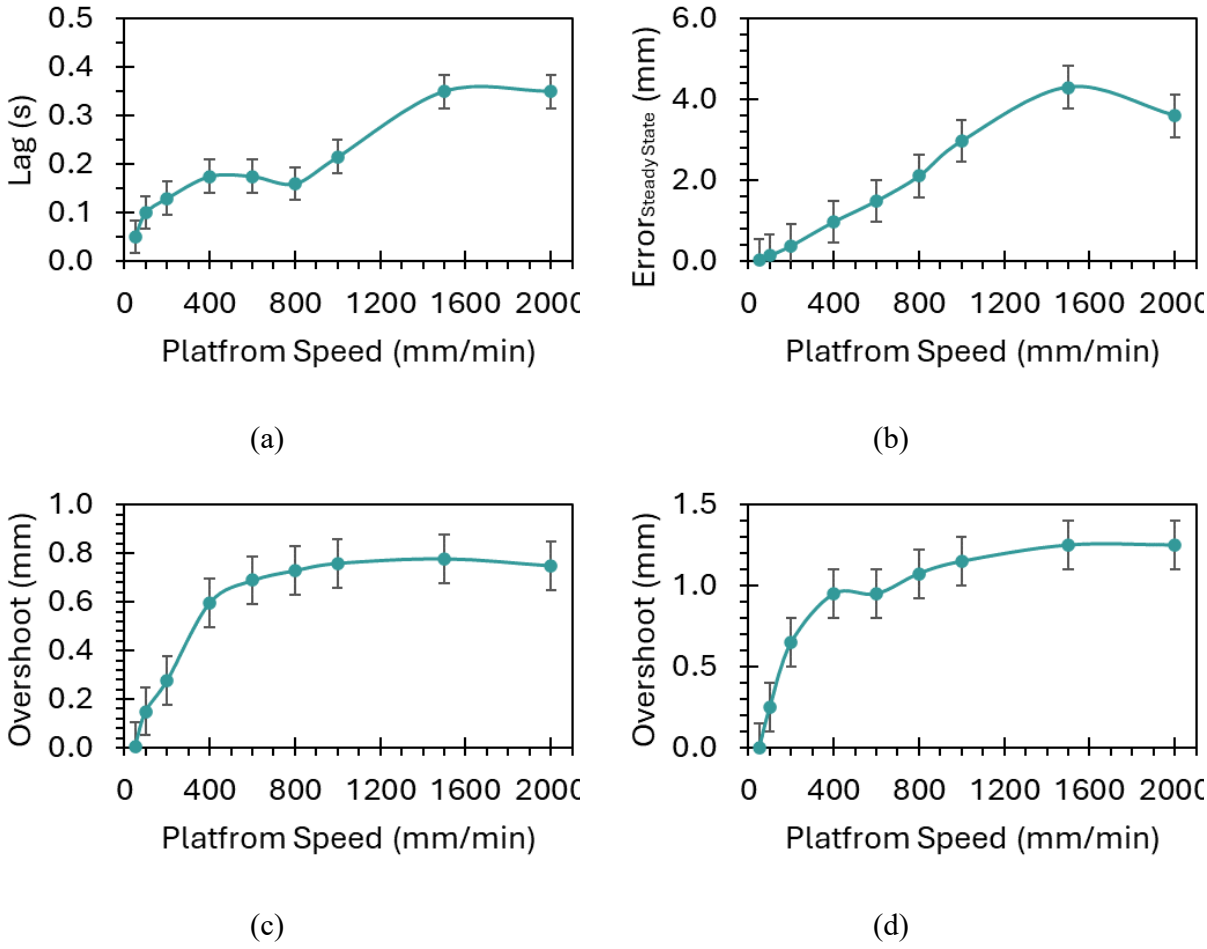

Figure 4-10: Performance analysis of bioprinting platform control at various speeds (50-100 m/min): graphical representation of (a) lag time, (b) steady state error, (c) overshoot, and (d) settling time.

latency. By continuously adjusting the bioprinter's movements based on the latest available tracking information, the control loop can effectively 'predict' and compensate for the expected movements of the target between tracking updates. This predictive adjustment is facilitated by the faster response rate of the control loop, which allows for real-time corrections and adaptations to any deviations detected by the slower tracking loop. The framework's design allows for parallel processing, with both systems running independently yet communicating effectively through internal network ports.

To assess the tracking filter's response to a ramp type of loading during the 3D printing process, the printing platform was systematically moved at varying speeds ranging from 50 to 2000 mm/min,

creating motion in two degrees relative to the robotic manipulator. The performance of the tracking filter was evaluated through a series of metrics, each highlighting different aspects of the system's dynamics (as described in Figure 4-8). The results are presented tabularly in Table 2-1 and illustrated

as plots in Figure 4-10. Delay between the platform motion and filter response (lag time), tended to increase with platform speed. Interestingly, it plateaued at around 0.350 seconds beyond a certain speed, suggesting the maximum processing capability of the system. During printing operations, the acceptable lag time was noted at 50 mm/min, which coincides with the control loop time. Above this threshold, print quality degraded, affirming that the system is optimized for lower-speed operations where lag times are minimal and do not detract from print integrity. The steady-state error is indicative of the system's ability to maintain a target position. This error grew as platform speeds increased, reflecting limitations in the feedback mechanism or control algorithm at high speeds. The system handled errors up to 4 mm, but for printing purposes, this error was limited at 0.025 mm, aligning with the fiber width and ensuring print precision. Overshoot, the extent to which the filter output exceeds the desired position, displayed non-linear patterns across different speeds. Notably, at 50 mm/min, the overshoot was minimal, signifying negligible impact on adjacent fibers during printing. This is a desirable trait as it minimizes defects and ensures the fidelity of the printed structure. Settling time, the duration for the filter output to stabilize within a specified range, lengthened as speeds rose. For high-precision printing, shorter settling times are preferred to maintain quality and operational efficiency.

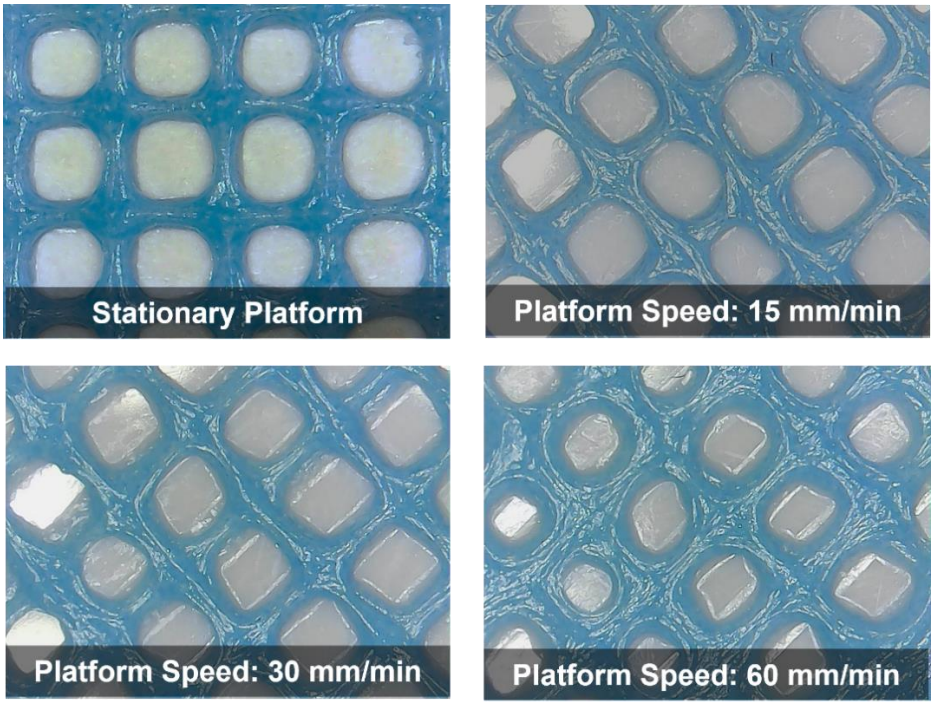

Figure 4-11: Comparative display of bioprinting results on platforms at different velocities. The top-left image showcases the uniformity achieved on a stationary platform, serving as the control. Progressing from left to right, top to bottom, the images exhibit the effects of increasing platform speeds on the print quality, with platform velocities of 15 mm/min, 30 mm/min, and 60 mm/min, respectively, illustrating the control system's precision and the impact of speed on deposition accuracy.

At lower speeds, the system showed negligible settling times, keeping the output within a 0.1 mm range of the target during which printing is conducted. Positional error remained consistently low across all tested speeds, which is within the robot hardware specifications. The ramp response of the control system at varying platform speeds is provided in Figure 4-9. Each graph illustrates the system's response to a step change in position at speeds ranging from 50 mm/min to 1500 mm/min. The solid lines represent the target displacement path, while the dashed lines with markers indicate the actual path taken by the system, capturing the dynamic behavior and response accuracy at different operational velocities.

After assessing tracking and printing limits, actual printing test on moving platform were carried out. Figure 4-11 shows the resulting print when the platform is subject to a sawtooth type of motion at three speeds (15, 30, and 60 mm/min) and an amplitude of 5 mm. The printing material is Pluronic F-127 (35 wt% in ultra-purified water) hydrogel. The visual observation confirms satisfactory printing results at 15 and 30 mm/min platform motion. A slower platform speed (50 mm/min) tends to allow for more controlled and uniform deposition of material, potentially resulting in more consistent pore sizes. As speed increases, the control system may struggle to maintain uniformity due to increased movement, leading to variability in pore size and shape. As a result, at a platform speed of 60 mm/min, the printing results are distorted but still able to produce a three-dimensional structure. This observation is in line with the ramp type analysis conducted for the tracking filter.

In summary, results indicate that while the system performs well at lower speeds, ensuring high accuracy in tracking and minimal positional error, challenges arise as speeds increase. These include managing steady-state errors, controlling overshoots, and addressing longer settling times. To optimize printing efficiency and quality at higher speeds, we may need to refine our control algorithms or enhance the responsiveness of the system. Ensuring that lag and settling times are compatible with the printing process's operational tempo is essential to achieve the desired printing performance across a range of platform speeds. The core innovation lies in the real-time synchronization of visual servo control with the printing mechanism, an innovative approach that allows for instantaneous adjustments and alignment with the platform's movements. This capability represents an advancement over traditional 3D printing methods, which are largely limited to static, planar surfaces. By addressing the challenges of printing on moving platforms through a sophisticated real-time feedback loop, our research not only enhances the precision and flexibility of 3D printing but also broadens its application spectrum to include scenarios previously deemed infeasible.

4.8 Conclusions

This chapter provides a complete methodology for developing and implementing a visual tracking filter for 3D printers. The developed novel printing process is to be able to print simple geometry on a printing platform undergoing motion. The developed methodology can be applied in applications related to in-situ fabrication, for example, in-situ bioprinting, in-situ repair, and manufacturing in remote and extreme environments such as space, etc. Because the framework is designed to work with generic commands for 3D printing, it is transferable to most commercially available 3D printers and cameras. The performance of the developed technique for non-cooperative printing has yielded validating results when printing simple linear geometry with low disturbing platform velocities. Potential applications of this autonomous functionality are not only limited to in-situ bioprinting but can open up more venues for further exploration.

Chapter 5 Development of Biomaterials for In-Situ Bioprinting of Skin

Summary: This chapter focuses on the comprehensive characterization and enhancement of Gelatin Methacryloyl (GelMA) with the addition of Cellulose Nanofibrils (CNF). The methodologies covering the selection of materials, synthesis of GelMA, and formulation of GelMA/CNF composites are presented. It examines the rheological and mechanical properties and the visible light photocrosslinking behavior of the biomaterial, providing a deep dive into its enhanced characteristics. Results and discussions elaborate on the improved mechanical properties and effective in-situ photopolymerization under light exposure, affirming the potential of GelMA/CNF in bioprinting applications. The chapter concludes with a summary of the findings, emphasizing the advancements in biomaterials for future tissue engineering and regenerative medicine.

5.1 Introduction

The development of new biomaterials holds immense potential across various biomedical domains, such as tissue regeneration [238], surgical adhesives [239], and the emerging field of in-situ bioprinting [240]. Within this array of hydrogels, Gelatin methacryloyl (GelMA) emerges as particularly noteworthy, distinguished predominantly by its exceptional thermo-responsive characteristics [241]. GelMA exhibits a favorable biocompatibility profile, minimal immunogenic reactions, and an innate propensity to foster cellular proliferation [242]. Moreover, GelMA's capacity to crosslink a three-dimensional matrix upon exposure to UV exposure in synergy with a photo-initiator is favorable to the bioprinting process [243]. What further sets GelMA apart from its contemporaries is its modifiable mechanical behavior, which can be fine-tuned through variables such as GelMA concentration, choice of photo-initiator, the frequency of crosslinking interventions, and the administered intensity dose during the photo-initiation process [244] [245].

Despite the recognized potential of GelMA-based hydrogels in regenerative medicine, there remains a scarcity of comprehensive knowledge about their behavior, particularly when synergized with additives like CNF. This gap limits the predictability and optimization of their bioprinting applications. This study aimed to investigate the rheological and visible light crosslinking properties of GelMA and GelMA/CNF bioinks, specifically focusing on the influence of CNF on the rheology and the mechanical integrity of the resulting structures. Emphasis was placed on understanding the influence

of temperature on the sol-gel transitions inherent to GelMA formulations. The resultant rheological properties of the GelMA/CNF composite were evaluated and compared against those of pure GelMA. Moreover, the photo-crosslinking behavior of the GelMA/CNF, especially when subjected to visible light exposure, was assessed, shedding light on the consequent mechanical properties of the material. These methods and results can guide researchers to perform appropriate studies on the material design for GelMA/CNF-based biomaterials.

5.2 Material Development

5.2.1 Materials Specification

Several key materials were procured for the functionalization process of the bioinks. Gelatin of Type A with a gel strength of 300 (cataloged as G2500) and phosphate-buffered saline (PBS, P3813) were sourced from Sigma-Aldrich. Furthermore, Methacrylic Anhydride, characterized by its 94% purity and inclusive of 2,000 ppm topanol A as an inhibitor (product number 276685), and Sodium Bicarbonate (NaHCO3) were also obtained from Sigma-Aldrich. In the subsequent purification and dialysis steps, a dialysis membrane tube with a molecular weight cutoff of 12 kDa, which was acquired from Ward's Science under product code ADDD0109-100, was used. Additionally, ultra-purified water from the Milli-Q IQ 7000 ultra-water purification system was utilized. For the bioink preparation phase, Eosin-Y (E4009), N-Vinylcaprolactam (stabilized at 98%, product number 415464), and Triethanolamine (90279) were sourced from Sigma-Aldrich. Complementing the aforementioned materials, Cellulose Nanofibrils Powder (CNF), with the chemical representation $(C6H16)5)_n$, was purchased from Cellulose Lab.

5.2.2 GelMA Synthesis

Visible light-based GelMA was synthesized using a specific protocol [232]. Initially, 10 g of gelatin (type A, gel strength 300) from porcine skin (G2500, Sigma-Aldrich) was dissolved in 100 ml of phosphate-buffered solution (PBS). This solution was stirred continuously, maintaining a temperature between 37-45°C to prevent thermal gelation, for approximately 90 minutes. For the functionalization of gelatin, 6 g of methacrylic anhydride was carefully added in dark conditions while stirring vigorously at 1500 rpm for a period of 3 hours. After this reaction, the mixture was centrifuged to remove any unreacted methacrylic anhydride. The supernatant was then diluted using an equal volume of preheated ultra-purified water. The diluted solution was subsequently transferred to a dialysis membrane tube (12 kDa) and underwent dialysis against ultra-purified water for seven days at 40°C.

Following dialysis, the pH of the GelMA solution was adjusted to around 7.4 using 1M $NaHCO_3$, after which it was freeze-dried for a duration of 5 days. This process is detailed in Figure 5-1.

5.2.3 GelMA/CNF Composite

To prepare the GelMA/CNF biomaterial, 1 g of freeze-dried GelMA was dissolved in 5 ml of PBS, with continuous stirring and heating at 40°C (resulting in particle size ranging between 5-50 um). Once dissolved, additions were made in the form of 0.2 g of n-vinylcaprolactum, 400 µl of triethanolamine, and 20 µl of eosin-y free acid, all under dark conditions. The final step involved crosslinking the bioink under cyan light (500 nm) at an intensity of 50 mW/cm² for 30 seconds.

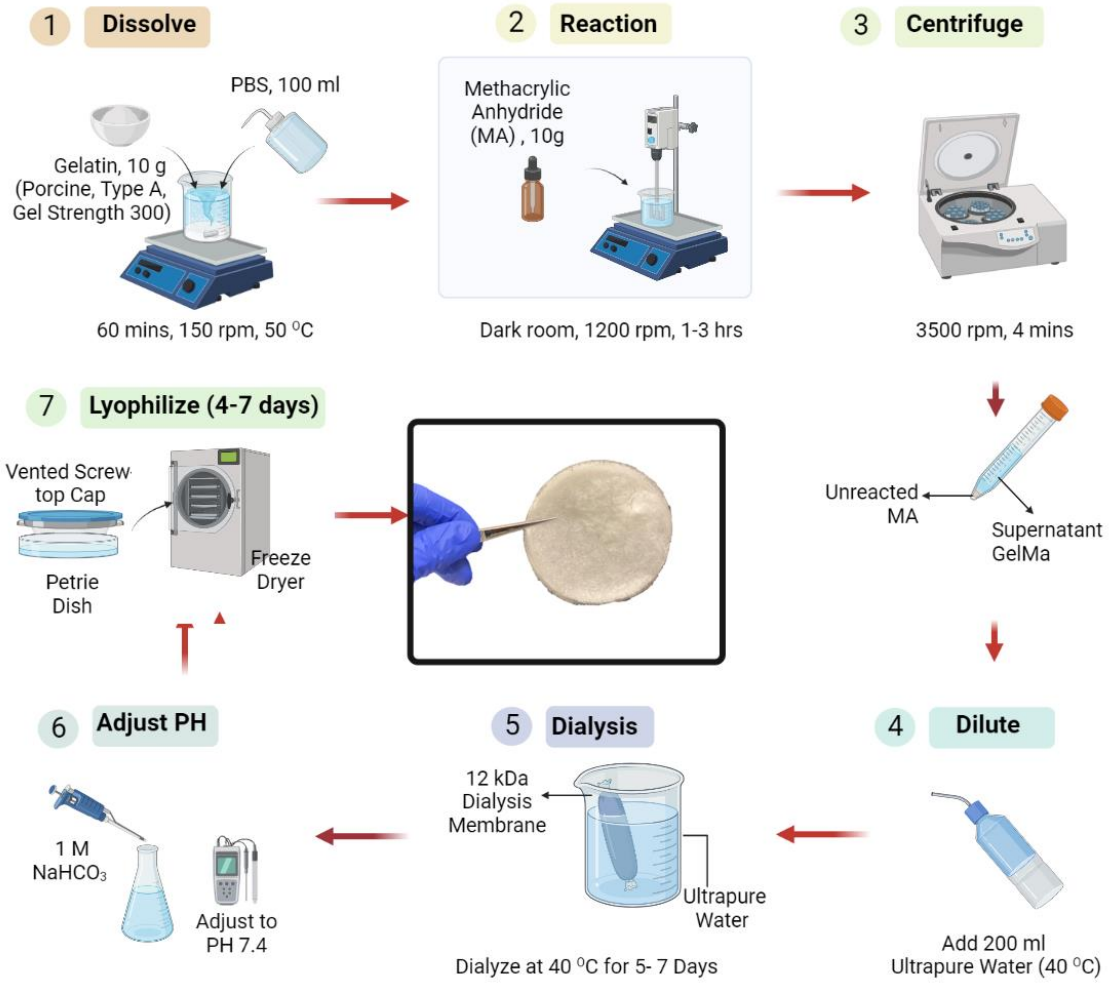

Figure 5-1: Schematic illustration of the step-by-step synthesis process of Gelatin Methacryloyl (GelMA). The flowchart depicts the sequential stages of GelMA preparation, starting from gelatin dissolution to the final biomaterial formation.

5.3 Rheological and Mechanical Evaluations

An in-depth examination of the mechanical behaviors exhibited by GelMA hydrogels was investigated by using the Texas Instrument Discovery Hybrid Rheometer (HR 30).

In the flow sweep analysis, GelMA solutions at a 10% w/v concentration were tested at a constant temperature of 25°C. Each iteration of this analysis was conducted with five distinct samples, ensuring the reliability of the results. The experimental arrangement consisted of concentric steel cylinders positioned within a Peltier environmental system, with specific features including a bob diameter of 28 mm, a bob length of 41.9 mm, and a cup diameter of 30.4 mm. An operating gap of 5.917 mm was meticulously maintained. Each cylinder was loaded with 22.6 ml of GelMA solution. After a 300-second soaking phase, a logarithmic shear rate sweep was introduced, ranging from 0.05 1/s to a peak of 150 1/s. Flow ramp tests were carried out to further deepen the insights to understand the correlation between ramp time and viscosity. This involved applying shear rates from 0.05 1/s to 150 1/s over 5, 15, 60, and 120 seconds intervals.

The oscillatory temperature ramp test focused on examining the effects of various heating and cooling rates on GelMA's phase transition behavior. This procedure utilized a Peltier concentric cylinder, each filled with 22.6 ml of GelMA. After a 600-second acclimation, the temperature was modulated in two distinct sequences. One approach involved a cooling gradient from an initial 50°C to 0°C, while the opposing regimen elevated temperatures from 0°C to 50°C. These tests adopted ramp rates of 0.1 and 1°C/min while maintaining a strain of 10% and an angular frequency of π rad/s. Each temperature profile was replicated thrice to ensure consistency.

Next, the oscillatory frequency tests were conducted at three set temperatures: 5°C, 20°C, and 25°C. This segment mirrored the geometric configurations of the flow sweep, employing concentric steel cylinders in a Peltier setting, each loaded with 22.6 ml of GelMA. After a 600-second soak, a 10% strain was enforced. This was succeeded by a logarithmic frequency sweep, commencing at 0.1 rad/s and climaxing at 150 rad/s. Finally, axial compression tests were conducted by applying compression force until failure at a cross-head speed of 0.05mm/sec.

5.4 Visible Light Photo-Crosslinking Behavior

In order to investigate the photo-crosslinking tendencies of GelMA/CNF biomaterial under visible light exposure, a specific set of oscillatory tests was performed. Throughout this examination, the sample was subjected to CYAN light (500 nm wavelength) with an intensity of approximately 100

mW/cm^2 at the sample's interface (Figure 5-2). The test configuration included a parallel plate with a diameter of 40 mm and a tightly controlled operating gap of 0.2 mm. A time sweep test was set up to observe the sol-gel transition in GelMA and GelMA/CNF samples. Oscillations were maintained at a steady rate of 25 rad/s while operating under a strain of 5%. The primary objective of this assessment was to study the required duration to crosslink the biomaterial effectively. Concurrently, evaluations were made to capture both the storage modulus (G', indicative of the material's elastic response and energy storage capabilities) and the loss modulus (G", representing the energy dissipated due to the viscous component). For the sake of robustness and reliability, this entire procedure was reiterated across three distinct samples.

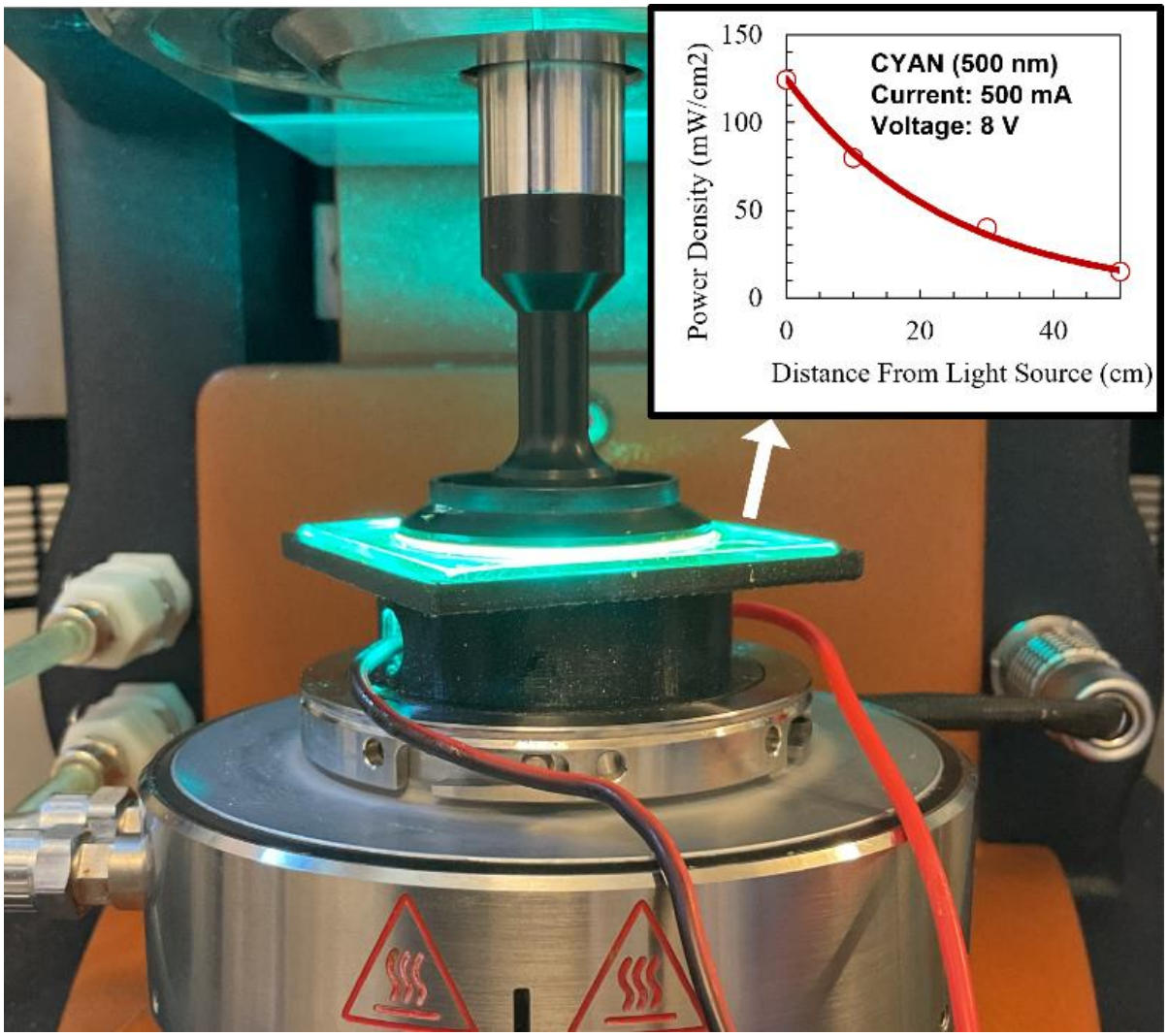

Figure 5-2: Rheological test setup for in-situ photopolymerization measurements. The system integrates a rheometer with cyan light (500 nm) exposure, facilitating real-time analysis of GelMA crosslinking under specific light conditions.

5.5 Results and Discussion

5.5.1 Mechanical Characterization

5.5.1.1 Degree of Substitution

The Degree of Substitution (DS) represents the quantity of methacryloyl substitutions per amino acid residue in the gelatin structure. To gauge the extent of methacrylamide group integration within GelMA, the DS was determined using ^{1}H-NMR spectroscopy (Advance NEO 300 MHz, Bruker, Germany). For the NMR analysis, GelMA, weighing 45 mg, was dissolved in 1 ml of deuterium oxide, and the spectrum was then acquired at ambient temperature. Essential post-processing procedures, such as phase and baseline adjustments, were implemented to refine the acquired spectral data.

The NMR spectrum revealed distinct peaks that were evaluated to measure the sample's degree of substitution (DS). The DS was determined based on the protocols detailed in [122], [246]. A notable peak around 2.90 ppm corresponded to the lysine methylene (ε-hydrogen amines) (see Figure 5-3). This peak was most pronounced in pure gelatin and showed a declining trend with increasing degrees of substitution, underscoring the role of lysine as the bonding site for methacryloyl conjugation. The observation suggests a progressive reaction of lysine groups with MAA, resulting in enhanced methacryloylation.

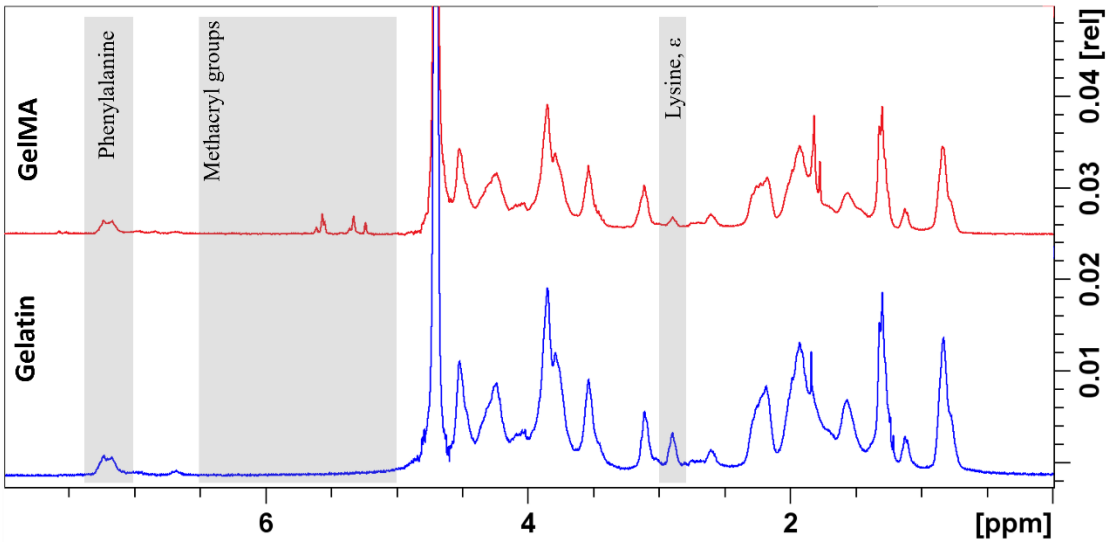

Figure 5-3: ^{1}H-NMR spectra showcasing gelatin and GelMA peaks. Distinctive methacryl group peaks are evident between 5-7.5 ppm. Specifically, the vinyl methylene hydrogen from the methacrylate groups is noticeable around 5.2-5.3 ppm, while the methacrylamide group manifests around 5.3-5.75 ppm. Phenylalanine's aromatic peaks emerge at approximately 7-7.5 ppm, and the ε-hydrogen of amines (from lysine and hydroxylysine) can be seen around 2.9-3.0 ppm.

In the GelMA samples, the spectrum showcased peaks associated with methacryl groups in the 5-6.5 ppm range [246]. Specific hydrogens of the methacrylate groups and one of the double bond hydrogens from the methacrylamide group were evident at around 5.55 and 5.60 ppm, respectively. Additionally, peaks linked to hydrogens of methacrylamide and hydroxyproline were noted at 5.22 and 5.32 ppm. Aromatic hydrogens from the tyrosine residues made their presence known at 6.8 ppm and 7.1 ppm, while phenylalanine residues had discernible peaks near 7.25 ppm [247]. An emerging peak at approximately 1.8 ppm was attributed to the methyl group (3H) of methacryloylated grafts. The prominence of this peak escalated with the DS, further emphasizing the increasing methacryloylation.

The spectral peaks and the following formula were used to calculate the degree of substitution:

$$DS = \left(\frac{\int \text{methacryloyl}_{\text{GelMA}}}{\int \text{phenylalanine}_{\text{GelMA}}}\right) \div \left(\frac{\int (\text{lysine and hydroxylysine})_{\text{Gel}}}{\int \text{phenylalanine}_{\text{Gel}}}\right) \quad 5\text{-}1$$

A degree of substitution (DOS) of 82.80% was obtained for methacrylate-modified GelMA.

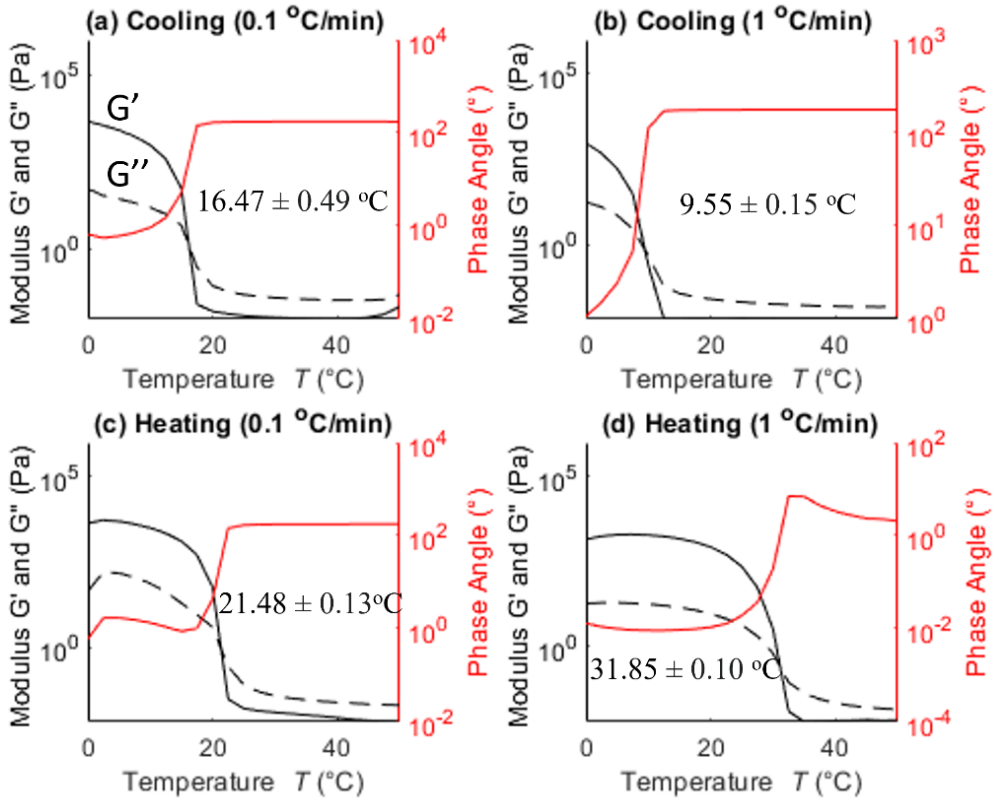

Figure 5-4: Temperature sweep tests for the physical gelation and solation of GelMA at a frequency of π rad/s and a strain of 10%, (a) Cooling from 50°C to 0°C at a rate of 0.1°C/min, (b) Cooling from 50°C to 0°C at a rate of 1°C/min, (c) Heating from 0°C to 50°C at a rate of 0.1°C/min, and (d) Heating from 0°C to 50°C at a rate of 1°C/min.

5.5.1.2 T_g Dependence on Rate of Heating and Cooling

In bioprinting, the determination of the solution to gelation transition temperature (T_g) is paramount for hydrogel screening. This is essential as the loading and extrusion processes for biomaterial must be conducted in the solution state. GelMA's T_g displays sensitivity to both cooling and heating rates [122], necessitating precise control. Above its glass transition temperature, GelMA predominates in the solution state, which is evident from a storage modulus that is considerably smaller than the loss modulus. Conversely, below the T_g, GelMA is in a gel state, demonstrating a greater energy storage mechanism compared to its energy dissipation capacity.

Distinct differences in the sol-gel transition temperature are observed during both cooling and heating, with additional variations tied to different rates of temperature change (0.1°C/min and 1°C/min) (see Figure 5-4). Notably, while [122] highlighted the influence of cooling on T_g, no such impact was identified during heating. The finding that an accelerated cooling rate reduces GelMA's T_g aligns with observations reported in [122]. During a slow cooling rate of 0.1°C/min, GelMA displays a T_g of roughly 16.47°C (see Figure 5-5). This suggests a tendency for GelMA to maintain a semi-solid state at relatively higher temperatures when cooled at this rate, which might benefit bioprinting by ensuring enhanced shape fidelity during printing. Conversely, at a faster cooling rate of 1°C/min, GelMA exhibits a T_g of 9.55°C, indicating a transition to a gel-like state at a reduced temperature. This knowledge is vital for bioprinting, hinting that for optimal extrusion, hydrogel should be kept at slightly elevated temperatures. During the heating process, a T_g of approximately 21.48°C at 0.1°C/min indicates that GelMA transitions to a fluidic state at this threshold when warmed slowly, informing the

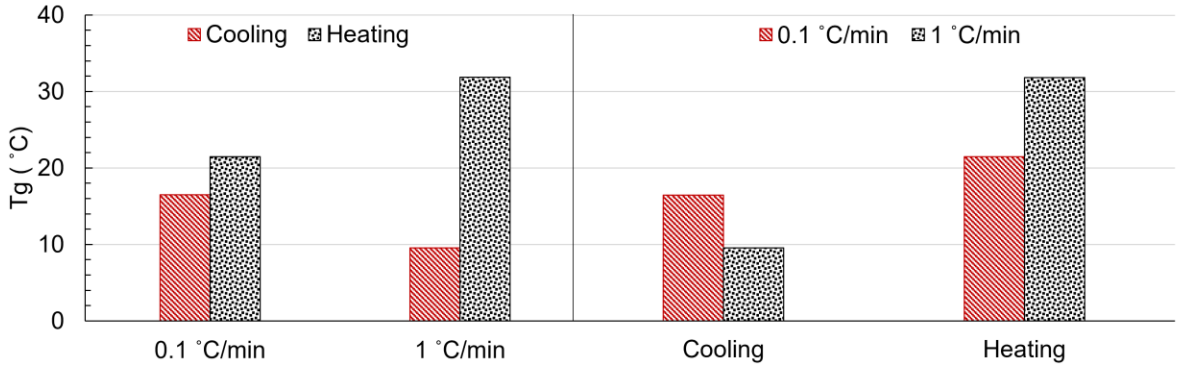

Figure 5-5: The presented data showcases results from temperature sweep tests on GelMA, which evaluates its response to varying rates of temperature changes. These tests were conducted at two distinct rates: 0.1 ˚C/min and 1 ˚C/min, encompassing both cooling and heating phases. The key metric of interest here is Tg, the temperature at which the storage modulus and the loss modulus intersect, commonly referred to as the glass transition temperature.

pre-printing preparations. Meanwhile, at a faster heating rate of 1°C/min, a T_g of 31.85°C suggests GelMA's enhanced stability at elevated temperatures.

On a molecular level, T_g represents a significant decrease in molecular mobility. Above the T_g, the polymer chains can slide past each other, giving a solution-like behavior, while below T_g, this movement is restricted, giving rise to a gel-like state. This explains why GelMA's storage modulus is higher than its loss modulus below its T_g, indicating a more solid-like behavior. The rate at which a polymer is cooled can significantly affect its T_g because of the kinetics of molecular organization. When cooled slowly, polymer chains have more time to organize into a more ordered state, increasing the temperature at which they transition to the rubbery state. Conversely, when cooled quickly, chains are trapped in a more disordered state, reducing the T_g. This is observed in the results, where the T_g of GelMA is higher when cooled at 0.1°C/min compared to 1°C/min. The rate of heating's influence on T_g is less prominent than that of cooling, which aligns with the results. This might be because, during heating, the disordered chains gain energy to move past one another, irrespective of their initial state.

In the realm of bioprinting, hydrogels need to transition from a liquid state (for smooth extrusion from the nozzle) to a semi-solid state (for shape retention post-extrusion). The temperature controls can be fine-tuned during printing to ensure the biomaterial's consistent extrusion. Understanding and controlling the T_g of a hydrogel, therefore, is crucial to optimize printability. Moreover, the T_g differences between slow and rapid rates indicate the potential for manipulating these rates post-printing to achieve desired structural properties. The identified T_g values offer vital information on the optimal temperature range for GelMA's extrusion and post-processing. With the T_g at 16.47°C when cooled slowly, GelMA is expected to exhibit a semi-solid state even at relatively higher temperatures. This behavior is invaluable during bioprinting, ensuring the printed structure doesn't collapse and maintains the desired shape. It's crucial to keep hydrogels in the right temperature range to ensure cell health. If hydrogels are maintained above their T_g during the printing process, there's a risk of cells being damaged due to shear forces. However, if kept below T_g, the hydrogel might not extrude smoothly. Therefore, knowledge of GelMA's T_g aids in defining a temperature window that ensures cell viability.

5.5.1.3 Flow Ramp Testing of GelMA at 25°C

GelMA, like other hydrogels, consists of a structure of complex network of polymer chains, often exhibiting time-dependent properties. This means that their behavior (in terms of viscosity, elasticity, etc.) can change depending on how quickly or slowly they are sheared. When shear is applied, these

chains can rearrange, stretch, or even break, depending on the magnitude and rate of the applied shear. If the shear rate increases rapidly, the chains might not have adequate time to adapt or relax, leading to different rheological responses. Flow ramp testing is a crucial technique in rheology aimed at understanding the shear behavior of materials as the shear rate increases or decreases systematically over time. Given that many biological processes and biotechnological applications (like bioprinting) involve dynamic changes in shear understanding how materials like GelMA respond to these changes is paramount.

Flow ramp testing of GelMA was systematically conducted to understand its shear-responsive behavior, with specific attention paid to its time-dependent rheological properties. As illustrated in Figure 5-6(a), the viscosity and stress responses of GelMA were observed in shear rates applied over intervals of 5, 15, and 60 seconds. A marked distinction in behavior was apparent across these durations, signifying the pronounced time-dependency of GelMA's rheology. As the shear rate surged, GelMA displayed varying viscosity profiles contingent upon the applied ramp time, underlining its dynamic response to shear rate changes over disparate time scales. The detailed stress-versus-viscosity plot from the flow ramp tests, shown in Figure 5-6, uncovers more intricate facets of this behavior. To reach a viscosity approximation of ~0.05 Pa·s, the stress requisites varied substantially: a relatively low stress of 0.25 Pa was necessary over 60 seconds, contrastingly higher at 0.85 Pa for 15 seconds, and sharply peaked

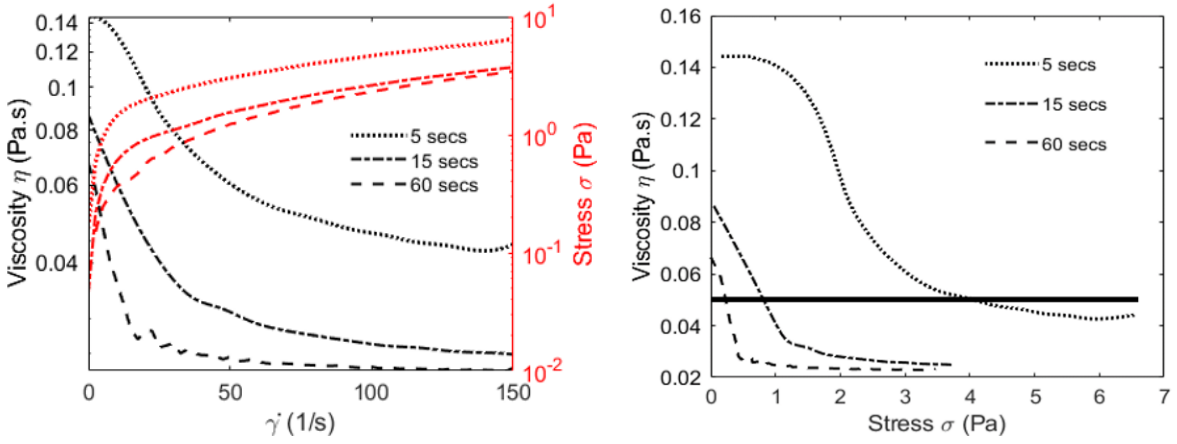

Figure 5-6: (a) Comparison of viscosity and stress responses for flow ramp tests conducted for GelMA, over 5, 15, and 60 seconds at 25 °C, illustrating the time-dependent rheological behavior of the material as shear rate increases, (b) Stress versus viscosity plot from flow ramp tests conducted over 5, 15, and 60 seconds. The stress required to achieve a viscosity of ~0.05 Pa·s varies significantly with ramp duration: 0.25 Pa for 60 seconds, 0.85 Pa for 15 seconds, and 4.2 Pa for 5 seconds, highlighting the material's sensitivity to shear rate changes over different time scales.

at 4.2 Pa for the 5-second duration. This differential in shear stress for identical viscosity values accentuates GelMA's sensitivity to rapidly changing shear environments.

This behavior suggests that GelMA's polymer chains undergo distinctive reorientations and interactions under varying shear conditions. In quicker ramp durations, the polymer matrix experiences abrupt rearrangements, leading to heightened stress responses. In contrast, longer durations allow the chains ample time for progressive alignment and interaction, reflecting in the gradually ascending stress profile. Moreover, rapid shear alterations, as in the 5-second ramp, might not furnish GelMA adequate time to break down or recover its structural integrity fully. In stark contrast, a 60-second ramp offers a more phased approach, where the gel's structural nuances are progressively revealed.

Bioprinting requires materials to be extruded through nozzles, which subjects them to shear. The shear rate can vary based on the speed of extrusion or the nozzle's geometry. For optimal bioprinting, it's crucial for the bioink to flow smoothly through the nozzle. The observed sensitivity of GelMA to changing shear rates, especially over short durations, indicates that rapid changes in printing speed could affect its flow characteristics. Once extruded, the bioink should maintain its shape (a property often related to its viscosity). The time-dependent behavior of GelMA suggests that if it's extruded rapidly (high shear rate over a short time), it might require higher stresses to achieve a certain viscosity, which could influence its ability to retain shape. The shear sensitivity could also have implications for cell viability. High shear stresses, especially over short intervals, could potentially damage cells encapsulated within the biomaterial. The differential shear stress required for GelMA to achieve specific viscosities offers an opportunity. Bioprinting parameters, like extrusion speed or nozzle design, could be tailored to exploit these rheological properties, ensuring optimal printability and post-print structural integrity.

5.5.1.4 Oscillatory Frequency Tests

Analyzing the storage modulus, a stark contrast in the behavior of GelMA is evident across the temperatures. At 5°C, the storage modulus displayed a pronounced elevation, transitioning from an almost negligible 0.01 Pa to a significant 2700 Pa, marking a 10^6-fold escalation (see Figure 5-7). Such a dramatic shift underscores the heightened propensity of GelMA to undergo gelation or solidification at this lower temperature. In contrast, at the elevated temperatures of 20°C and 25°C, the storage modulus remained invariant, suggesting the elastic attributes of GelMA retain a consistent and stable structural rigidity within this range. The considerable increase in storage modulus at 5°C can be explained by the molecular alignment and increased intermolecular interactions. As the temperature

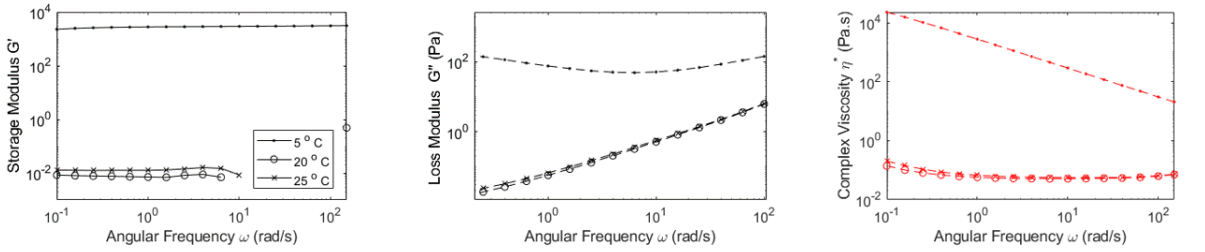

Figure 5-7: Oscillatory frequency tests conducted on GelMA at three distinct temperatures, (a) 5°C, (b) 20°C, and (c) 25°C—provide pivotal insights into its viscoelastic behavior.

reduces, GelMA's molecular chains may undergo greater hydrogen bonding or other secondary interactions, resulting in a more structured and interconnected network, evident as a gel state. This alignment becomes less ordered at temperatures of 20°C and 25°C, as suggested by the consistent storage modulus values, which indicates the presence of balanced molecular motion and interaction.

Analyzing the loss modulus reveals another layer of complexity. At 20°C and 25°C, the loss modulus remained relatively stable across most frequencies, indicating an enhanced energy loss ability at higher angular frequencies. This suggests that within this temperature window, GelMA exhibits both elastic and viscous characteristics, leaning more towards the latter as frequency escalates. Conversely, at 5°C, there's a notable 100-fold increment in the loss modulus. Interestingly, no frequency-dependent behavior in energy loss was observed at this temperature, hinting at the dominant elastic nature of GelMA at this colder condition. The behavior of the loss modulus further elaborates on the molecular interactions in GelMA. At 5°C, the absence of frequency-dependent behavior in energy loss indicates that the molecular chains of GelMA are less mobile and more restricted in their movements, primarily because of strong intermolecular forces. In contrast, the slight inclination towards viscous behavior at higher frequencies at 20°C and 25°C could suggest that at these temperatures, the molecular chains of GelMA possess more freedom and show a combination of both viscous and elastic behaviors.

At 5°C, the pronounced rise in the storage modulus reflects GelMA's ability to resist flow and deformation, essentially behaving more like a solid than a fluid. This property can be advantageous in bioprinting, ensuring that once extruded, GelMA can hold its shape effectively. On the other hand, at 20°C and 25°C, the steady storage modulus suggests that GelMA maintains a semi-solid or gel-like consistency, which provides a balance between flowability and shape retention. This is vital for the extrusion process in bioprinting, as the biomaterial needs to be easily pushed out of the nozzle yet maintain its shape once deposited. The observations on the loss modulus offer further insights into

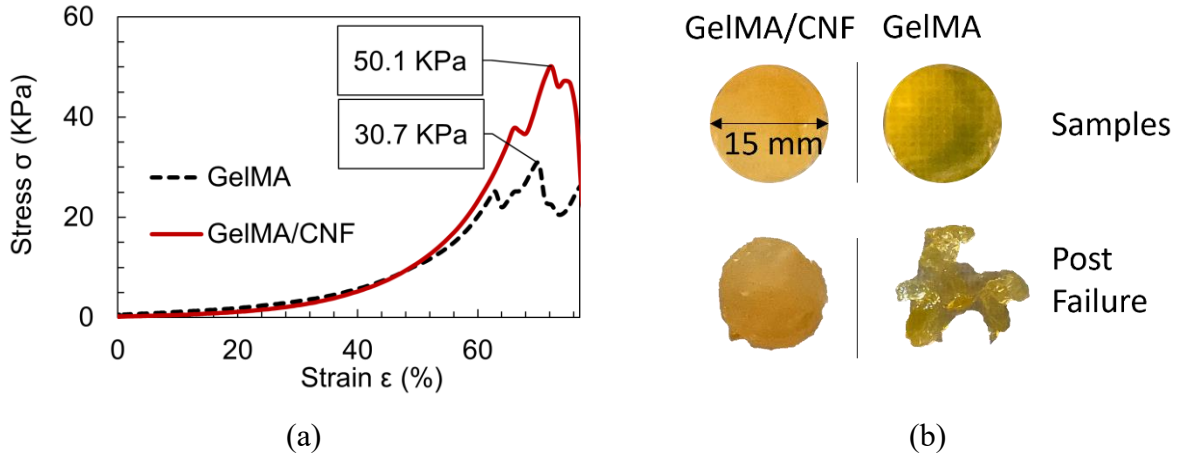

Figure 5-8: (a) Axial compression test results comparing the mechanical properties of pure GelMA and GelMA incorporated with CNF. The graph showcases the yield points and initial elastic moduli of both samples (b) Post-failure visual comparisons of GelMA and GelMA-CNF samples following axial compression tests. The images highlight the disintegration of pure GelMA into gel-like fragments, while the GelMA-CNF composite exhibits localized fractures with an overall intact structure.

GelMA's flow dynamics. At 20°C and 25°C, the increase in energy loss at higher angular frequencies signifies that GelMA exhibits shear-thinning behavior within this temperature range. This is a crucial attribute for biomaterials, as shear-thinning materials flow more easily under high shear rates (like during extrusion) and solidify or gel quickly once the shear is removed, ensuring structural integrity.

From a bioprinting perspective, the quick gelation of GelMA at 5°C signals its capacity to rapidly solidify post-extrusion, ensuring that the printed structure remains intact. This rapid transition from a near-liquid to a gel-like consistency is favorable, facilitating the retention of the desired printed form. Simultaneously, the consistent behavior of GelMA at 20°C and 25°C highlights its suitability to maintain printed structures post-extrusion, aiding subsequent cellular integration and tissue maturation.

5.5.1.5 Axial Compression Test

Axial compression tests have further expanded our understanding of the mechanical properties of GelMA and its composite with cellulose nanofibers (CNF). The tests were performed up to the failure point, and the samples were observed after failure. The yield point of pure GelMA was found to be 30.7 KPa, while the GelMA incorporated with CNF exhibited a yield point of 50.1 KPa, marking a significant increase of 63.2 percent (see Figure 5-8(a)). This pronounced difference underscores the substantial impact of CNF on the mechanical resilience of GelMA. Furthermore, the initial elastic modulus, a measure of a material's inherent stiffness, was observed to decrease (up to 20% strain) in the CNF-added GelMA samples. The decrease in the elastic modulus suggests that the CNF

incorporation imparts a more compliant nature to the GelMA matrix, potentially enhancing its adaptability to mechanical stresses.

Pure GelMA's lower yield point of 30.7 KPa, compared to the 50.1 KPa of the GelMA-CNF composite, suggests a difference in the molecular interactions within the two materials. GelMA, being derived from gelatin, possesses a network of triple-helical structures. These helical domains provide GelMA with its inherent mechanical strength. When subjected to compression, these helices resist deformation up to a certain point, after which they start to unravel, leading to the observed yield point. The introduction of CNF into GelMA appears to modify these molecular interactions. CNFs, with their high aspect ratio and surface area, can interact with the GelMA matrix, potentially disrupting the regularity of the helical domains. This could explain the increased yield point in the GelMA-CNF composite. The decrease in the initial elastic modulus further supports this notion, indicating a more compliant or flexible molecular structure in the presence of CNF.

Visual observations post-failure provided additional insights (see Figure 5-8(b)). While the pure GelMA samples disintegrated into smaller gel-like fragments, reminiscent of typical gel behavior, the CNF-incorporated samples told a different story. Despite fractures, the overall structure of the CNF samples remained largely intact, with only a few cracks manifesting. This behavior suggests that CNF affects not only the rheological and mechanical properties of GelMA but also its failure mechanisms. The presence of CNF seems to provide a supportive scaffold, enhancing the structural integrity of the hydrogel even after failure.

Post-failure observations provide additional molecular insights. The disintegration of pure GelMA samples into smaller gel-like fragments suggests a failure primarily at the molecular junctions between the helical domains. In contrast, the CNF-incorporated samples, despite fractures, maintained their overall structure. This behavior implies that CNFs might be acting as a reinforcing agent at the molecular level. While they might disrupt the regular helical network, they seem to provide alternative structural support, preventing complete disintegration and instead leading to localized cracks.

5.5.2 In-Situ Photopolymerization Behavior of GelMA/CNF Under Light Exposure

The in-situ polymerization behavior of GelMA, both standalone and when integrated with cellulose nanofibers (CNF), was analyzed during a light exposure duration of 300 seconds (see Figure 5-9). This involved an oscillatory time sweep test, capturing dynamic shifts in both the storage and loss modulus across these formulations.

For variances between GelMA and its CNF-incorporated variant using the F-test, a p-value of 0.094 was deduced. Falling below the confidence alpha level of 0.10, this pointedly led to rejecting the null hypothesis, indicating unequal variances across the two groups. Then, a two-tailed t-test was employed to identify potential deviations in the storage modulus means of the two samples. The null hypothesis was accepted, with the resulting t-value being 0.149 and staying within the alpha level of 0.10. This indicates that there is no substantial distinction in the storage modulus between GelMA in isolation and when added with CNF. On exploring the variance in the loss modulus data through an F-test, an extremely significant p-value of 1.3e-9 was observed. This outcome, being well below the accepted confidence alpha threshold of 0.10, results in rejecting the null hypothesis, corroborating unequal variances between the groups. Further, the two-tailed t-test resulted in a t-value of 1.53e-5, which is considerably below the alpha cutoff of 0.10. Therefore, the null hypothesis was rejected, indicating the presence of a significant statistical difference in the loss modulus when comparing standalone GelMA and GelMA infused with CNF.

Bioprinting's success hinges on the understanding and manipulation of hydrogel properties. The in-situ polymerization, a critical phase during the printing process, can influence the final properties of the printed structures. Our results shed light on the rheological behavior of GelMA, a widely used bioink, during this phase. The incorporation of CNF, while not significantly altering the storage modulus, had a pronounced effect on the loss modulus. This divergence in behavior underscores the multifaceted impact of additives like CNF. A higher loss modulus, as observed in the CNF-incorporated bioink, represents a more liquid-like behavior, which might influence the printability and shape fidelity of the

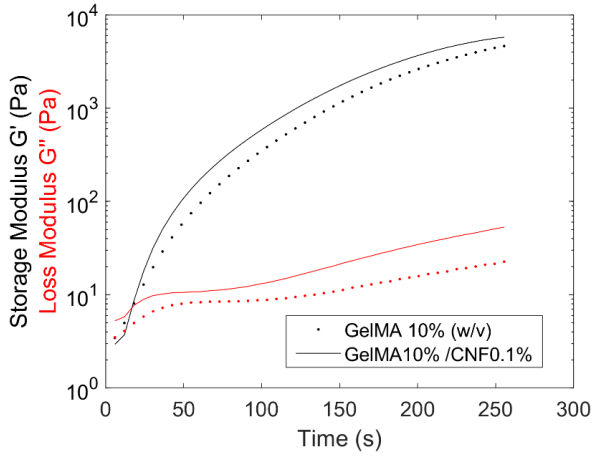

Figure 5-9: Rheological changes of GelMA and GelMA incorporated with cellulose nanofibers (CNF) during in-situ polymerization under light exposure for 300 seconds (mean of 3 samples). The storage and loss moduli were recorded using an oscillatory time sweep test. The variance and t-test analyses indicate significant differences in the behaviors of GelMA and GelMA with CNF, especially in their loss modulus during polymerization.

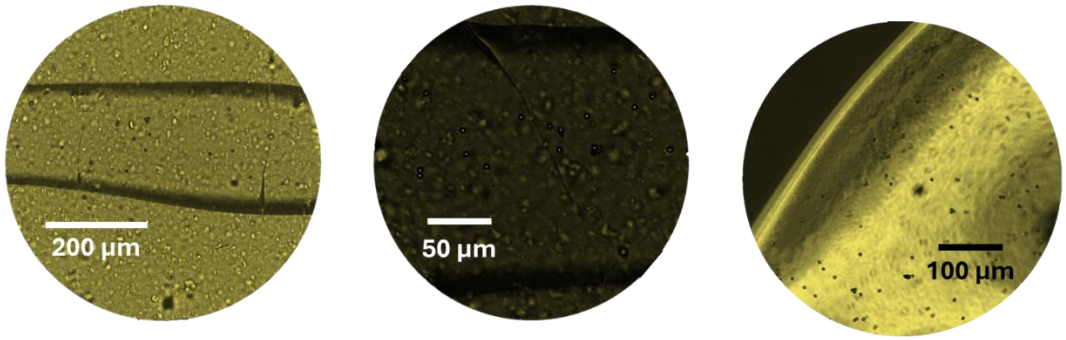

Figure 5-10: Microscopic image of a hydrogel fiber with uniformly dispersed 10 µm FluoSpheres™ polystyrene particles, illustrating the homogeneity achievable in bio-ink formulations. Such dispersion is indicative of the hydrogel's potential for consistent printing performance.

structures. As bioprinting applications diversify, tailoring hydrogels to exhibit desired rheological properties during in-situ polymerization will be paramount.

5.5.3 Cellular Dispersion and Perfusion in Hydrogel

The successful in situ bioprinting of skin relies heavily on the precise deposition of bio-inks that encourage cellular viability and function. An integral aspect of the bio-ink formulation is the consistent dispersion of functional components – cells, signaling molecules, and agents encapsulated within carrier particles.

Microscopic analysis of the developed hydrogel laden with fluorescent polystyrene particles simulates the expected dispersion of cellular components within a bio-ink. As illustrated in Figure 5-10, the 10 µm FluoSpheres™ particles (by Invitrogen, Thermo Fisher Scientific) are evenly distributed throughout the printed fiber (mean diameter 200 µm). This uniformity is critical for ensuring that each printed layer contributes equally to the overall function of the tissue construct, e.g., nutrient transport, cellular signaling, or mechanical support.

The rheological properties of bio-inks dictate their printability – the ability to be extruded through a printing nozzle and maintain structure post-deposition. The observed particle dispersion implies the hydrogel's favorable viscosity and shear-thinning behavior, essential for extrusion-based bioprinting. Furthermore, the absence of significant particle agglomeration suggests that the hydrogel can be

printed without clogging the nozzle or causing irregularities in flow, which are common challenges in printing with cell-laden bio-inks.

The term perfusion here refers to the hydrodynamic potential flow of nutrients and signaling molecules through the interstitial spaces between the embedded particles. The even spacing of the particles suggests that post-printing, the hydrogel will permit a homogenous flow of biological fluids, closely mimicking the capillary network within native tissues. Such flow is crucial for delivering nutrients and oxygen to embedded cells.

In-situ bioprinting directly on a patient involves depositing layers of bio-ink to build up tissue structures according to the complex, non-linear topographies of the wound or defect site. The developed hydrogel's demonstrated printability and potential for uniform cellular distribution position it as a promising candidate for future applications.

5.6 Conclusions

In this chapter, the development of GelMA enhanced with CNF is discussed, and its properties, both in its original and CNF-enhanced forms, are thoroughly examined. Our findings highlight GelMA's adaptability for bioprinting, especially its shear sensitivity during flow ramp tests. This sensitivity emphasizes the need for precise calibration in bioprinting to ensure printability, shape retention, and cell health. Oscillatory tests revealed the critical role of temperature and frequency in determining GelMA's viscoelastic behavior. This knowledge is essential for improving the quality of 3D-printed structures and emphasizes the importance of temperature control during the entire printing process. The addition of CNF to GelMA significantly altered its mechanical properties, as seen in axial compression tests. CNF strengthens GelMA, making it more suitable for bioprinting applications that require durable post-printing structures. Furthermore, our in-situ photopolymerization tests showed differences in pure GelMA and CNF-integrated GelMA behavior, particularly in their loss moduli. This indicates CNF's transformative effect on GelMA during light-mediated polymerization, underscoring the need to understand CNF's influence better. An in-depth exploration of GelMA, with and without CNF, provides valuable insights for the bioprinting community. While CNF enhances GelMA's properties, it also introduces complexities that require a deeper understanding. As bioprinting continues to evolve, this knowledge will be crucial for optimizing biomaterials to meet the diverse needs of advanced tissue engineering and regenerative medicine.

Chapter 6 System Integration for In-situ Bioprinting

Summary: This chapter provides an in-depth look at the integration of the developed technologies into a single bioprinting system, highlighting the potential for advancing in-situ applications. The integration process is thoroughly examined, detailing the technical framework developed to integrate the software and hardware elements. The chapter also discusses the setup and calibration of the bioprinting system, emphasizing the importance of synchronization between the visual tracking and the robotic control algorithms. This integrated approach aimed to facilitate seamless operation, enabling bioprinting capabilities on non-planar and moving surfaces that are representative of actual hosts.

6.1 Introduction

In advanced bioprinting technologies, the convergence of software and hardware technologies forms the backbone of innovative solutions. The individual components developed for Objectives I, II, and III have demonstrated standalone capabilities, laying the groundwork for applications in bioprinting. However, the true potential of these advancements can only be harnessed through effective integration, as outlined in Objective IV. This chapter integrates these distinct elements into an interconnected bioprinting system, a critical step towards realizing the practical application of in-situ bioprinting on moving, non-planar biological platforms.

The preceding chapters laid the foundation for this integration. Chapter 3, dedicated to Objective I, introduced an innovative slicing algorithm capable of adapting any 3D model to accommodate free-form surfaces. This advancement is noteworthy for enabling bioprinting on non-planar surfaces, which is essential when operating on biological hosts where the deposition platform defies traditional planarity. The surface-slicing approach ensures that implants are crafted with precision, accommodating the unique contours of the target site. Chapter 4, dedicated to Objective II, presented a novel visually guided 3D printing process. This process is instrumental in enabling the deposition of biomaterials onto moving platforms, edging closer to the goal of bioprinting directly on live hosts. This capability is crucial, as it accommodates the inherent physiological or incidental motions encountered during the bioprinting process, ensuring fidelity and accuracy in material deposition. Chapter 5, addressing Objective III, presented the development of a composite hydrogel incorporating Cellulose

Nanofibrils (CNF) within Gelatin Methacryloyl (GelMA). This formulation resulted in an enhanced rheological and mechanical properties optimized for extrusion printing. Crucially, this bioink's compatibility with green light crosslinking presents a safer alternative to traditional UV light methods, aligning with the health-centric focus of in-situ bioprinting.

The developed system integrates various disciplines, such as computer vision, robotics, control theory, and bioprinting technology. By combining these areas, it aims to address the challenges of bioprinting on non-static or irregular surfaces, which is a step forward in bioprinting. The algorithm's core lies in its ability to adapt to the platform's real-time position changes. Through camera systems and image processing techniques, the system can detect minute shifts in the position of the printing surface, allowing for precise adjustments to be made to the printing process. The algorithm bridges the gap between the lab and future clinical applications by addressing the real-world challenges of bioprinting, such as motion and irregular surfaces. It also underscores the importance of integrating feedback systems into bioprinting workflows to account for unpredicted variables.

This chapter aims to capture the integration of these multifaceted systems into a single, streamlined bioprinting apparatus. The primary goal is to simulate an in-situ bioprinting scenario and identify integration hurdles. It outlines the robotic bioprinting framework, which can execute complex printing tasks on models positioned on non-static platforms.

6.2 Bioprinting Hardware System

Robotic Manipulator

The core of the bioprinting hardware setup is a 4-degree-of-freedom (DoF) robotic arm operating on the Marlin open-source 3D printing firmware, which is typically utilized in additive manufacturing machines (see Figure 6-1). Specifically, the setup employed a Dobot Magician, a widely accessible and economic 4-axis robotic manipulator noted for its adaptability and customization options. The Dobot Magician has an exceptional repeat position accuracy of ±0.2 mm, ensuring the precision required for 3D printing processes. It supports a payload of up to 500 grams, which accommodates the weight of different extrusion systems and the installation of LED lamps. The arm's length measures 320 mm, providing a working range covering various printing scales. Additionally, its design allows for a rapid movement speed, reaching up to 800 mm/s in a straight line.

Material Support

Integrating the robotic arm with dual extrusion systems is an added capability for the system, broadening the range of materials that can be tested. The polymer-based extrusion system is equipped

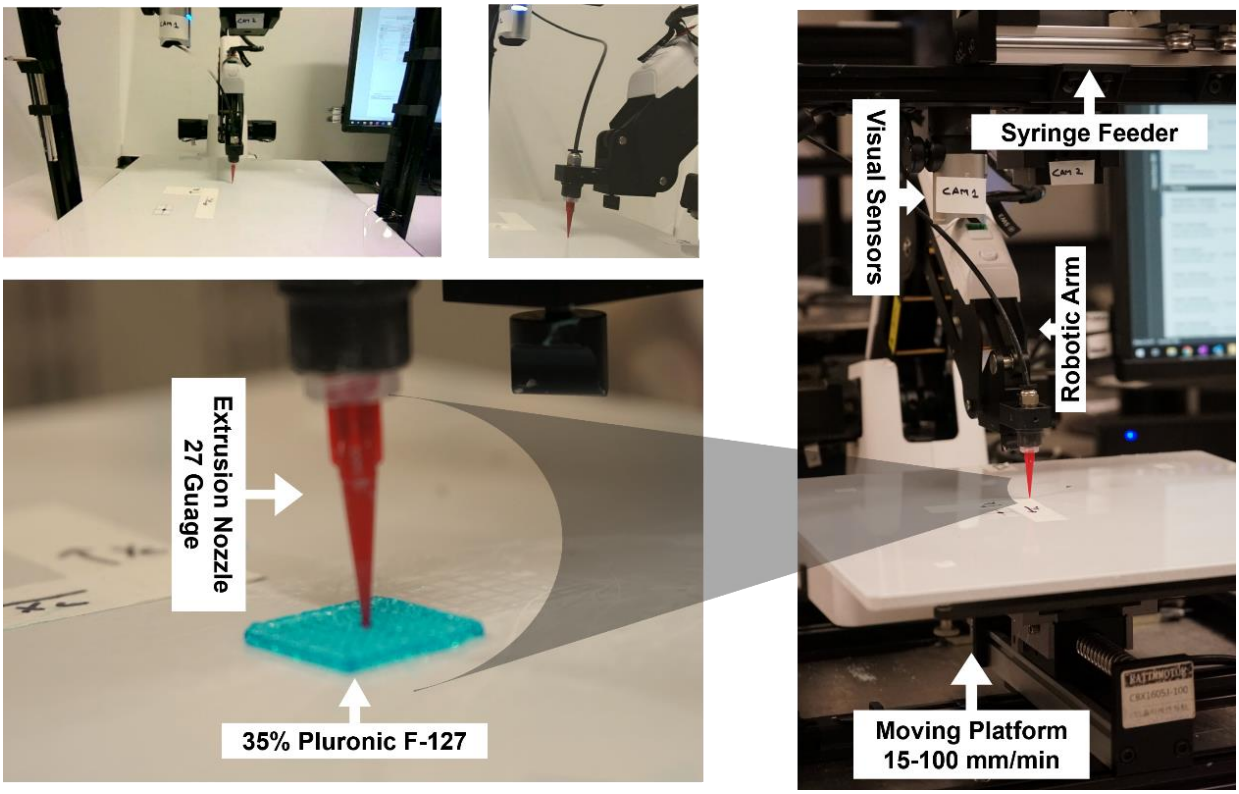

Figure 6-1: Experimental setup, robotic arm-based bioprinter with integrated visual sensor and a fully tracked platform.

with a heated 0.4 mm nozzle, a thermocouple, a heating block, and a cooling fan to maintain optimal printing conditions. This setup has been tested and proven to effectively print a variety of materials, including polylactic acid (PLA), polycaprolactone (PCL), and acrylonitrile butadiene styrene (ABS). The precision and quality provided by this system ensured high-quality prints suitable for preliminary testing of the surface slicing algorithm.

A hydrogel extrusion system was also developed and integrated to the robotic system to simulate the bioprinting process. This system is driven by a NEMA23 stepper motor on a linear stage and 3D-printed fittings that secure a 10 ml syringe. The 100 mm long linear stage could not be mounted directly onto the robotic arm due to its significant weight (1.78 kg). Protective sleeves were fabricated and coupled with the syringe to safeguard the light-sensitive hydrogel. The syringe attaches to a 250 mm long black Teflon tube that connects to the nozzle holder affixed to the robotic arm. Nozzle tips, accommodating sizes from 20-27G, were coated with black paint to mitigate light exposure before use. This design ensures the hydrogel remains unaffected by external light sources during extrusion. In the adopted design, the flow of hydrogel through a narrow conduit like a Teflon tube leads to increased shear stress on the material. While alternative pressure-driven dispensing systems were explored, the

mechanical motor's superior precision in material extrusion, as dictated by the G-code's volume specifications, was ultimately preferred. This setup streamlines the bioprinting workflow, ensuring accurate and consistent hydrogel deposition.

To enable visible light-assisted crosslinking, an array of 100 W LEDs was integrated beneath the printing platform, with printing conducted above a transparent glass plate during the initial design phase to evaluate light-sensitive curing. The LED setup, operating between wavelengths of 450 – 500 nm, offered an intensity range of 2000 - 6000 lumens with a total power of 50 W. However, this configuration of directing crosslinking light from beneath the nozzle led to increased material clogging, particularly at lower printing speeds.

In subsequent design iterations, the source of light energy was repositioned above the printing area. This involved using several 10 W LED lamps, emitting light between 495 to 500 nm wavelengths and powered at 10 volts. These LEDs were selected for their narrow emission spectrum, primarily focused on the wavelength range effective for crosslinking the GelMA hydrogel in the Eosin-Y system, as detailed in Chapter 5. A specially designed holder attached to the robotic arm positions the LEDs to overlook the nozzle, angling them to maximize illumination and ensure uniform exposure around the extruding material. This above-nozzle lighting approach notably reduced nozzle clogging. The LEDs' power supply is managed via an adjustable power source.

Testing Platform

The testing platform of the bioprinter consists of a 200 mm polycarbonate square sheet, providing a stable base to place the in-situ models. This sheet is mounted on top of a linear stage, like the one utilized in the extrusion system. The stage's motor receives commands from a Duet 3D printing control board, which is interfaced with a separate computer system. The platform is tilted at a 15-degree angle, granting it two degrees of freedom relative to the robot's frame of reference. This orientation requires the robotic arm to execute precise x and y-axis motion commands to counterbalance the platform's single-direction motion effectively. To simulate in-situ bioprinting conditions, a three-dimensional model of a biological host is strategically placed on the platform to perform in-situ printing operations. This setup serves as a test bed for evaluating the bioprinter's performance in non-stationary scenarios and also aids in refining the robotic system's response to variable printing surfaces, which is crucial for further application.

Visual Feedback

The system design incorporates a visual feedback system consisting of two cameras to observe the printing platform. The first, a Microsoft LifeCam, operates at a 1920 x 1080 pixels resolution, capturing images at a frame rate of 30 frames per second (fps). The second, an ELP 16 MP camera, offers even greater detail with a resolution of 3840 x 2160 pixels and a frame rate of 30 fps. Placing these cameras in varying orientations ensures occlusion-free tracking of platform markers. The dual-camera setup not only provides redundancy but also enhances the accuracy of the tracking process. By integrating measurements from both cameras, the system can more effectively counteract the inherent noise in each individual sensor, resulting in a more reliable and precise visual feedback mechanism for the bioprinting process.

Structural Integration

The entire bioprinting system is constructed within a sturdy structure composed of 2020 aluminum extrusion profiles. The robotic arm is securely mounted onto the frame in a stationary position and calibrated in alignment with each camera affixed to the frame. A calibration grid is fastened to the printing platform, with one specifically designated circular dot as the pivotal point of reference—the Image Frame (IF) origin. In a subsequent alignment procedure, the printing nozzle is precisely positioned over this same reference point, establishing a consistent origin for the Object Frame (^{O}F), representing the starting point for the tracked object. This critical setup, as detailed in Section 4.2, is fundamental to maintaining consistent and accurate alignment of the in-situ platform with the robot workspace.

6.3 Software System

This section outlines the integration of developed algorithms with the bioprinting hardware system, detailing the software development across three primary components: calibration, tracking algorithm, and printer control algorithm.

6.3.1 Calibration

This initial phase involves setting up the system to ensure the hardware and software align accurately. It encompasses the calibration of cameras and the robotic arm to establish a common reference frame. This step is crucial to ascertain that the printed materials are deposited precisely on the target area, considering the platform's orientation and the extrusion nozzle's positioning.

Camera calibration employing homography estimation is a common method for precisely correlating pixel coordinates with their respective real-world counterparts. Within this methodological framework, the homography matrix transposes points on a plane from global world coordinates to image coordinates. It is important to note that the designated points for mapping maintain coplanarity. The composition of the homography matrix derives from two distinct matrices: the intrinsic camera matrix and the camera's extrinsic parameters, as described previously in Section 4.3. The homography matrix, denoted as H, is a 3x3 matrix containing elements h_{11}, h_{12}, h_{13}, h_{21},..., h_{33}, as detailed in Equation 6-1.

$$\begin{bmatrix} u \\ v \\ w \end{bmatrix} = \begin{bmatrix} f_x & 0 & c_x & 0 \\ 0 & f_y & c_y & 0 \\ 0 & 0 & 1 & 0 \end{bmatrix} \begin{bmatrix} r_{11} & r_{12} & r_{13} & t_1 \\ r_{21} & r_{22} & r_{23} & t_2 \\ r_{31} & r_{32} & r_{33} & t_3 \\ 0 & 0 & 0 & 1 \end{bmatrix} \begin{bmatrix} X \\ Y \\ Z \\ 1 \end{bmatrix}$$

$$\begin{bmatrix} u \\ v \\ w \end{bmatrix} = \begin{bmatrix} C_{11} & C_{12} & C_{13} & C_{14} \\ C_{21} & C_{22} & C_{23} & C_{24} \\ C_{31} & C_{32} & C_{33} & C_{34} \end{bmatrix} \begin{bmatrix} X \\ Y \\ Z \\ 1 \end{bmatrix}$$

$$\begin{bmatrix} u \\ v \\ w \end{bmatrix} = \begin{bmatrix} C_{11} & C_{12} & C_{14} \\ C_{21} & C_{22} & C_{24} \\ C_{31} & C_{32} & C_{34} \end{bmatrix} \begin{bmatrix} X \\ Y \\ 1 \end{bmatrix} = H \begin{bmatrix} X \\ Y \\ 1 \end{bmatrix} = \begin{bmatrix} h_{11} & h_{12} & h_{13} \\ h_{21} & h_{22} & h_{23} \\ h_{31} & h_{32} & 1 \end{bmatrix} \quad \text{6-1}$$

The inverse of the homography matrix, denoted as H^{-1} is needed to map coordinates from the image frame back to the world frame. For instance, consider having world coordinates for four points (p_1, p_2, p_3, p_4) alongside their respective mappings (p'_1, p'_2, p'_3, p'_4) within the image coordinate framework, where $p_i = (x_i, y_i)$ and $p'_i = (x'_i, y'_i)$. Utilizing these point pairs, we can establish a linear system composed of eight equations and eight unknowns, defining the parameters h_{11}, …, h_{32}, while standardizing the final parameter by setting h_{33}=1. For these four points, algebraic relations are employed to formulate a system of linear equations (Equation 6-1). This system represents a homogeneous linear problem where the optimal solution can be derived using singular value decomposition.

$$\begin{pmatrix} -x_1 & -y_1 & -1 & 0 & 0 & 0 & x_1x'_1 & y_1x'_1 & x'_1 \\ 0 & 0 & 0 & -x_1 & -y_1 & -1 & x_1y'_1 & y_1y'_1 & y'_1 \\ -x_2 & -y_2 & -1 & 0 & 0 & 0 & x_2x'_2 & y_2x'_2 & x'_2 \\ 0 & 0 & 0 & -x_2 & -y_2 & -1 & x_2y'_2 & y_2y'_2 & y'_2 \\ -x_3 & -y_3 & -1 & 0 & 0 & 0 & x_3x'_3 & y_3x'_3 & x'_3 \\ 0 & 0 & 0 & -x_3 & -y_3 & -1 & x_3y'_3 & y_3y'_3 & y'_3 \\ -x_4 & -y_4 & -1 & 0 & 0 & 0 & x_4x'_4 & y_4x'_4 & x'_4 \\ 0 & 0 & 0 & -x_4 & -y_4 & -1 & x_4y'_4 & y_4y'_4 & y'_4 \\ 0 & 0 & 0 & 0 & 0 & 0 & 0 & 0 & 1 \end{pmatrix} \begin{pmatrix} h_{11} \\ h_{12} \\ h_{13} \\ h_{21} \\ h_{22} \\ h_{23} \\ h_{31} \\ h_{32} \\ h_{33} \end{pmatrix} = 0 \quad \text{6-2}$$

During the calibration process (as illustrated in Figure 6-2), a grid comprising circles spaced 10 mm apart is positioned on the platform, covering a significant portion of the image field. This grid facilitates the computation of the system of equations detailed in Equation 6-2. The calibration sequence is executed as follows: initially, the image undergoes a conversion to an unsigned 16-bit integer format, followed by thresholding. Utilizing the Niblack local thresholding algorithm, the threshold at each pixel is dynamically adjusted based on the local mean and standard deviation. Specifically, the threshold for each pixel is determined by adding the neighborhood's mean to the product of its standard deviation and a predefined constant, k, centered around an '$n \times n$' neighborhood for local threshold determination.

Subsequent to thresholding, a filtering process is employed, wherein a particle filter is applied to identify and analyze connected pixel clusters or regions within the image. These identified regions, often referred to as particles, enable the extraction of statistical data, such as the detection, count, size, and location of particles. For this purpose, the particle analysis function in LabView is utilized, offering detailed insights into the characteristics of the observed particles. Next, known as target-to-point mapping, each detected circle within the image is allocated a corresponding point in the world frame (^{W}F) coordinate system, assigning real-world spatial context to the detected image features. A set of equations derived from multiple pairs of corresponding object points and image points. For each pair, two equations exist (due to the u and v coordinates), which are compiled into matrix form and solved by Singular Value Decomposition (SVD). This process involves solving the equations for all points into a comprehensive system and resolving for the homography matrix H, which facilitates the mapping from object points to image points, as described above. The decomposition of the homography matrix H enables the extraction of rotation and translation matrices.

The intrinsic and extrinsic parameters refinement is performed by minimizing the reprojection error - the discrepancy between actual image point locations and those predicted by the estimated camera parameters. This process is accomplished using non-linear least squares methods such as the Levenberg-Marquardt algorithm, where reprojection error is defined as the Euclidean distance between observed and predicted point locations in the image, typically measured in pixels. For a dataset comprising N points, the total reprojection error is calculated as the mean of all individual discrepancies, where $e_i = \frac{1}{N}\sum_{i=1}^{N}\sqrt{(u_i - \hat{u}_i)^2 + (v_i - \hat{v}_i)^2}$, with u_i, v_i representing observed coordinates and $\hat{u}_i$, $\hat{v}_i$, denoting predicted coordinates based on the camera model. A lower reprojection error signifies a closer alignment between the model predictions and observed data, indicating an

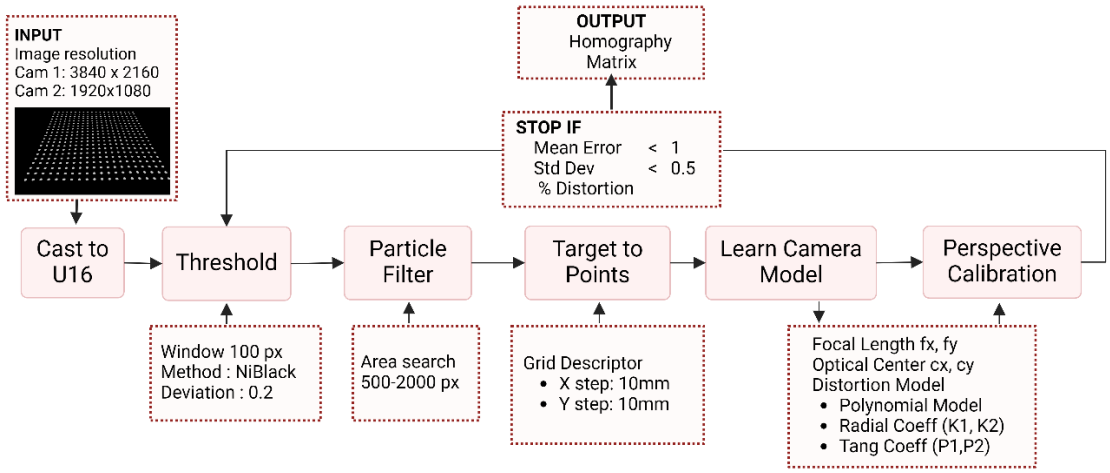

Figure 6-2: Workflow for camera calibration process. Outline of the steps from image acquisition through calibration to final perspective correction, detailing input parameters, processing techniques, and output criteria.

accurate calibration of the camera's intrinsic and extrinsic parameters. Conversely, high reprojection errors suggest potential calibration inaccuracies attributable to factors such as suboptimal calibration patterns, limited variation in calibration images, errors in detecting image points, or unsuitable calibration methods. In our setup, reprojection errors below one pixel are considered satisfactory.

6.3.2 Tracking Algorithm

This algorithm uses camera systems to track the position of the printing surface in real time. It identifies and monitors specific markers or features on the substrate, adapting to any movements or changes during the printing process. The visual tracking information is continuously fed into the bioprinting control system. By knowing exactly where the surface is and how it's moving, the system can adjust the printhead's actions based on the slicing algorithm’s data. This ensures that the biomaterial is applied precisely where intended, even if the substrate shifts.

The process begins with capturing an image, typically from a camera mounted on the bioprinter or positioned to observe the printing area (as illustrated in Figure 6-3). The captured image is converted to an 8-bit unsigned integer format. This standardizes the pixel intensity values to a 0-255 range, simplifying subsequent processing steps. This conversion is essential for compatibility with most image processing functions, especially in libraries like LabView and OpenCV. Calibration information, including the homography matrix and details about the reference frame, is set. The homography matrix transforms the camera's view (image frame) and the actual print surface (world frame). Calibration

information also involves aligning the camera's field of view with the printer's coordinate system to ensure precise tracking and printing.

Template-based matching is a method used to find areas in the image that match a provided template. The grayscale value pyramid method improves this process by creating a pyramid of downscaled images (i.e., progressively lower resolution). This allows the algorithm to first search for matches in a smaller, less detailed context, which is faster and less resource-intensive, and then refine the search in higher-resolution levels of the pyramid. This approach improves the speed and accuracy of pattern matching, which is especially useful in dynamic or variable conditions. After a match is found, its coordinates are initially in the pixel frame (i.e., relative to the image dimensions). These coordinates are then converted to the image frame using calibration information. This step translates pixel coordinates into a real-world context within the camera's view. The coordinates in the image frame are now transformed into the camera frame using the homography matrix. This transformation aligns the coordinates with the camera's perspective, considering angles, distance, and lens distortion. The coordinates in the camera frame are then converted into the robot world frame. This is crucial for the bioprinting process, as it translates the tracked object's position (e.g., a part of the body or a moving platform) into coordinates that the robotic printer can understand and act upon. Finally, the translated coordinates are sent to the printer control program, which uses this information to adjust the movements of the bioprinter accordingly. This ensures that the printing material is deposited precisely where it is intended, even if the target surface is moving.

This tracking algorithm given in Figure 6-3 allows for precise, real-time adjustments during the bioprinting process, accommodating movements and ensuring accurate material deposition on dynamic or uneven surfaces.

6.3.3 Printer Control Software

The process chart in Figure 6-3 describes the control algorithm for a bioprinting system incorporating both tracking and printing functionalities integrated through a loop with a cycle time of 20 milliseconds. Following is the breakdown of each segment:

The system starts by reading the G-code command, which includes coordinates (X_c) where the printing or tracking action is supposed to occur. These are typically the planned positions from the bioprinting file. The camera makes an observation and checks if the data (e.g., images or positions) is valid.

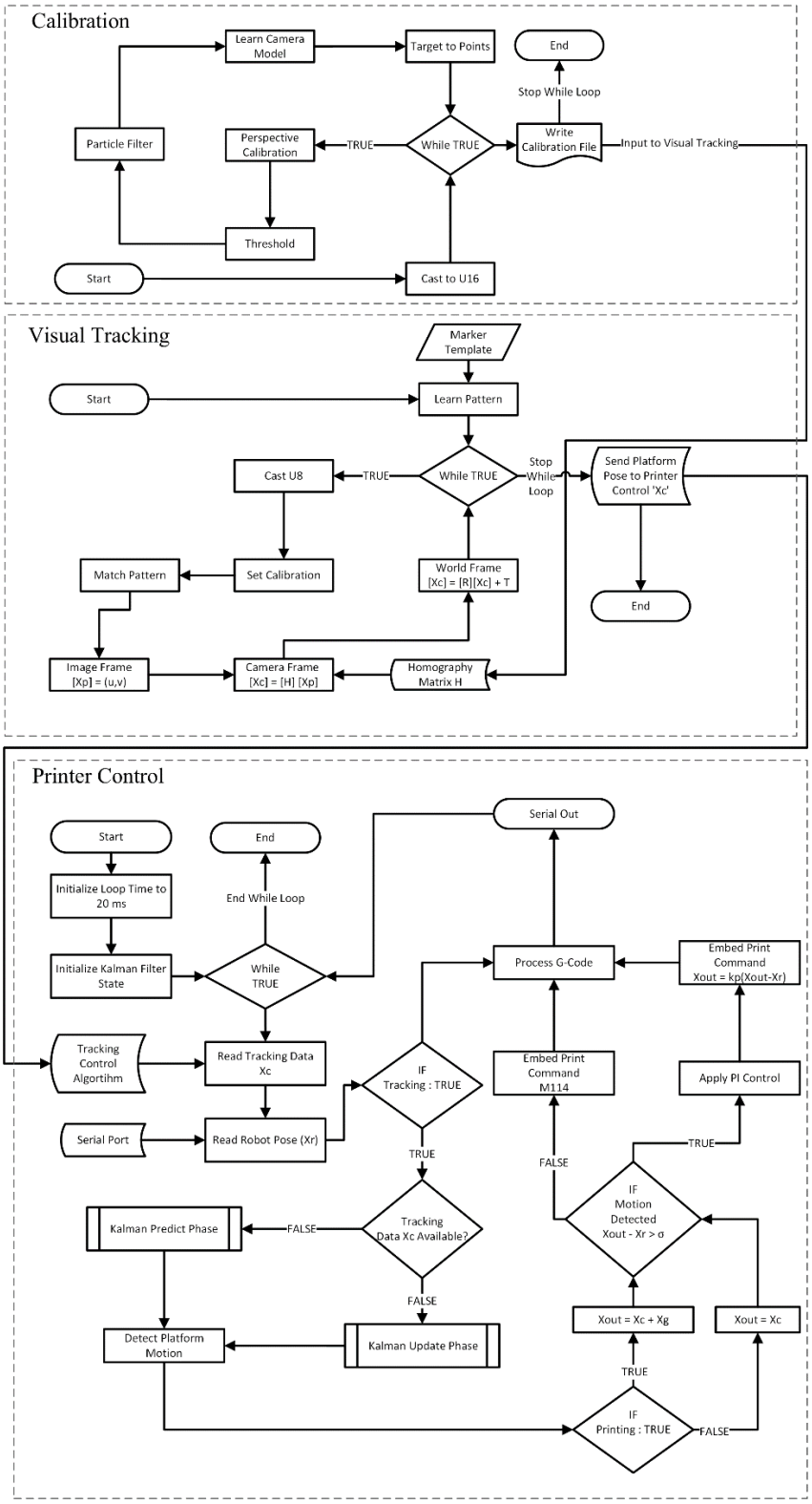

Figure 6-3: Flowchart depicting the integrated process of calibration, tracking, and control in the robotic bioprinting system.

If valid, it proceeds; if not, it skips to prediction. Based on the camera data validation, the process branches into two paths: If the data is valid, the system uses it to update the Kalman filter's state estimate ($\overline{X_c}$). The filter integrates the actual position of the camera with the previous state to produce a more accurate estimation. If the data is not valid (or in parallel), the Kalman filter predicts the next state ($\overline{X_c}$).) based on the previous states, to maintain continuity even without new camera data.

The system decides whether it is currently tracking and printing or just tracking. If tracking and printing, the output position (X_{out}) is calculated by adding the current position set by G-code (X_G) and the estimated position from the Kalman filter ($\overline{X_c}$). If only tracking, X_{out} is set equal to the position estimated by the Kalman filter (X_c). The system checks if there's any motion detected by comparing the output position (X_{out}) with a current robot position obtained through kinematics transformation of joint positions (X_R), making it an endpoint open loop type visual servo system as described in Section 4.4. The control logic is activated if motion is detected and the output position exceeds this threshold.

For both tracking and printing modes, if motion is detected, the printer's control system adjusts the output coordinates (X_{out}) using a control gain (k_p) multiplied by the difference between desired and actual positions (output vs. robot's current position). The final output position (X_{out}) is fed into the printer control, which modifies the printer's movements according to the calculated positions to align with the target path, adjusting for any detected movement or deviation. The adjusted position coordinates are then sent to the printer hardware through a serial interface, updating the G-code commands in real time. The serial outputs are different commands sent to the printer to move to the new location in X, Y, and Z directions (G1 commands) or perform specific functions like updating the robot status.

This control software integrates real-time tracking data with the printing process, allowing the bioprinter to adapt to dynamic changes or movements on the printing surface, ensuring that the material deposition is precise and consistent with the planned design.

6.3.4 Asynchronous Adaptive Tracking and Printer Control (AATPC) System

The design of bioprinter framework, which accommodates a tracking loop operating at a slower rate (100 ms) compared to the printer control loop (20 ms), presents several innovative aspects. By allowing these systems to operate asynchronously, the design efficiently utilizes the strengths of both the precision of slower camera tracking and the responsiveness of a faster printing control system. Despite the difference in operational speeds, the integration allows for real-time feedback between the tracking and printing processes. This can be particularly emphasized in applications where dynamic adjustments

are crucial, such as printing on a moving platform or biological host. Highlighting how the printer can still react in real-time to positional changes detected by the camera at a different rate showcases the system's ability to adapt to the environment.

The slower update rate in the tracking loop enables the implementation of advanced filtering algorithms, such as Kalman filters or moving averages, which can smooth out the noise by considering previous and current observations. This results in more stable and reliable tracking data. Meanwhile, operating at a higher frequency, the printer control loop can utilize this filtered, less noisy data to make precise and minute adjustments more frequently. This setup ensures that the bioprinting process remains stable and accurate, even in noise. Moreover, high latency can lead to a lag between the actual position of the moving target and its perceived position, resulting in inaccuracies and potential printing errors. In the developed framework, while the tracking loop operates with inherent delays, the faster printer control loop helps mitigate the impact of this latency.

By continuously adjusting the bioprinter's movements based on the latest available tracking information, the control loop can effectively 'predict' and compensate for the expected movements of the target between tracking updates. This predictive adjustment is facilitated by the faster response rate of the control loop, which allows for real-time corrections and adaptations to any deviations detected by the slower tracking loop. The framework’s design allows for parallel processing, with both systems running independently yet communicating effectively through internal network ports.

6.4 Integration Framework

The integration of slicing non-planar surfaces, visual tracking, and hydrogel optimization – forms a comprehensive bioprinting system. Figure 6-4 shows how all these components are interconnected. The bioprinting process starts with the CAD models, moves through the slicing algorithm to generate print instructions, and proceeds through calibration and tracking to ensure precise print alignment. The tracking directly influences the platform's control, ensuring that the movements are accounted for during the printing process. Finally, the printing control algorithm manages the actual material deposition, adjusting in real time based on feedback from the tracking system. Following is a description of how these systems together facilitate advanced and adaptive in-situ bioprinting:

Inputs and Preparation

(i) The computer-aided design (CAD) model of the object to be printed, usually representing the final desired structure, (ii) Specifically refers to the CAD model of a medical implant, if applicable, detailing

its precise geometry, and (iii) the surface model on which the bioprinting is to occur, which can be non-planar (illustrated in Figure 6-4).

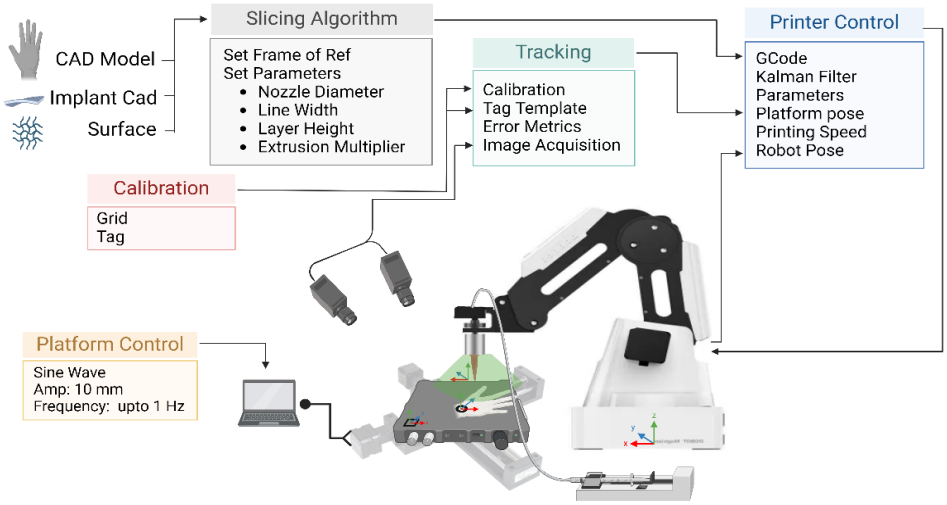

(a)

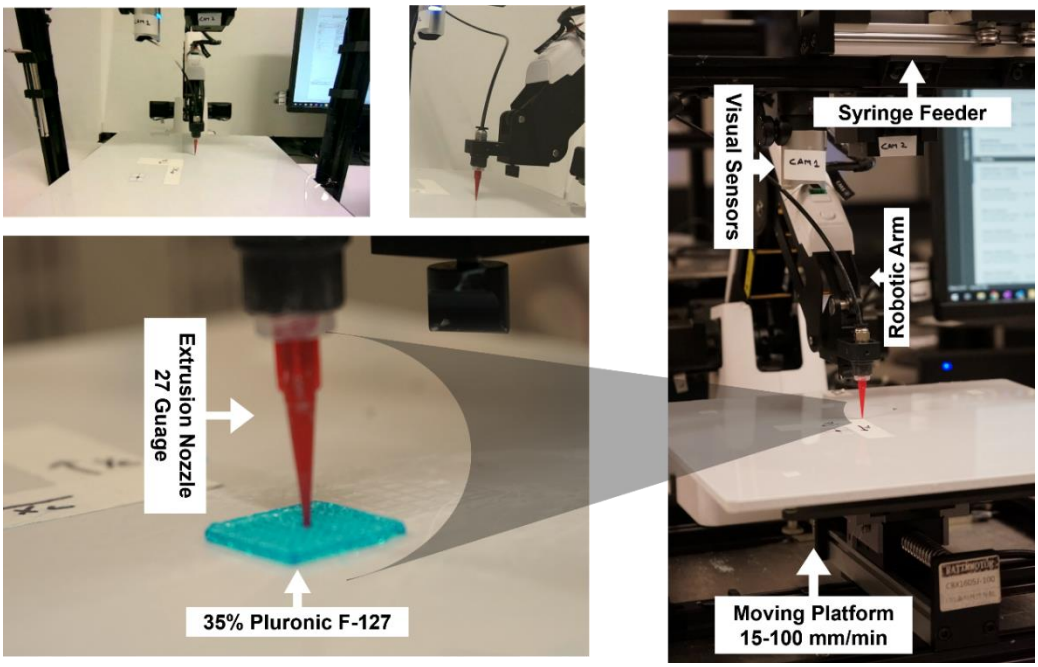

(b)

Figure 6-4 (a) Illustrates the integration and workflow of a robotic bioprinting system designed for printing on moving surfaces. (b) Experimental setup, robotic arm-based bioprinter with integrated visual sensor and a fully tracked platform.

Pre-printing

- The slicing algorithm processes the 3D model based on the target surface's geometry, producing a series of instructions for layer-by- This module processes the CAD model(s) to generate layer-by-layer instructions (slices) for the printing process. The algorithm sets various printing parameters relative to the model's geometry: nozzle diameter, line width, layer height, and extrusion multiplier, all tailored to match the bioprinter's capabilities and the material's properties.
- Calibration involves setting up the bioprinting system to accurately map between the model's virtual space and the real-world print surface. It uses grid tags (presumably fiducial markers) for spatial calibration, enabling the system to understand its position relative to the printing surface.

Printing Phase

- The tracking algorithm monitors the position and orientation of the printing surface, adjusting the bioprinting process in real time. As printing commences, the visual tracking algorithm provides real-time feedback on the substrate's position and movement. This information allows the control system to make continuous adjustments to the printing path, ensuring the nozzle follows the precise trajectories generated by the slicing algorithm despite any motion of the substrate. Utilizes calibration data, a tag template for identifying specific points on the print surface, and error metrics to maintain accurate tracking.
- The printer control program manages the actual deposition of material based on the sliced model and the real-time tracking information. Inputs include the G-code (a language that controls the movement and operation of the printer), parameters from the Kalman Filter (to predict and correct the position based on tracking data), connection details for integrating tracking data, and the printing speed.
- Platform control manages the movement of the printing platform, which in this context appears capable of moving dynamically (as indicated by the sine wave, suggesting oscillation up to 10 mm and up to 1 Hz). It ensures the platform can move according to predefined patterns or in response to live tracking, facilitating the printing on dynamic surfaces.

Through the seamless integration of these algorithms, the bioprinting system can precisely deposit hydrogels onto complex and moving surfaces, addressing key challenges in in-situ fabrication. This integration represents advancement in making in-situ bioprinting more applicable to real-world scenarios.

6.5 Autonomous System

The bioprinting system developed as part of this thesis research demonstrates autonomy levels, especially within robotic calibration, tracking, and control mechanisms. This system can autonomously calibrate camera settings and track dynamic objects, indicative of partial to conditional autonomy. The ability to execute printing tasks based on real-time tracking data without human intervention aligns with conditional autonomy. However, while the system performs satisfactorily within its programmed parameters and responds effectively to predefined conditions, it does not exhibit full autonomy, as it requires human input for initial setup and may need manual oversight for unexpected scenarios. Therefore, it can be positioned between partial (3) and conditional (4) autonomy in the spectrum of robotic independence. The bioprinting system's current state reflects substantial progress in autonomous bioprinting technologies but also underscores the need for further development to achieve higher levels of operational autonomy.

6.6 Conclusions

This chapter detailed the integration of advanced algorithms, autonomous systems, and enhanced biomaterials for in-situ bioprinting, specifically targeting the fabrication of skin tissues on dynamic surfaces. The developed bioprinting system proved its ability to maintain the structural integrity of implants in case of unforeseen motion up to 50 mm/min. This achievement underscores the system's robustness and adaptability in dynamic printing environments. The multidisciplinary approach adopted underscores the importance of collaborative effort in addressing complex biomedical challenges. It exemplifies how technological advancements can push the boundaries of what is possible in medical science and patient care. This collaborative effort drives the innovation forward and ensures that the solutions are practical and meet the specific needs of bioprinting applications.

Chapter 7 Conclusions and Future Works

Summary: This chapter concludes this thesis's research and development efforts on developing advanced in-situ bioprinting technologies. It consolidates the integration of research and innovations outlined throughout this thesis, (i) developing an innovative non-planar bioprinting algorithm, (ii) integrating autonomous functionalities within a robotic bioprinting framework, (iii) enhancing GelMA biomaterial formula with cellulose nanofibrils, which demonstrates mechanical and rheological improvements, and (iv) demonstrating the effective system integration of these components into a user-friendly in-situ bioprinting testing platform. This concluding chapter provides essential findings on the research's limitations and highlights the unique contributions of this thesis to the bioprinting domain, particularly the technological and material developments. Finally, the chapter concludes by outlining the future research directions.

7.1 Introduction

This study is dedicated to the challenges within the realm of in-situ bioprinting of skin. Developing bioprinting techniques for non-planar surfaces represents a leap toward replicating complex anatomical structures. This approach overcomes traditional flat-surface limitations, offering a pathway to more accurate and personalized tissue constructs, thus meeting the urgent need for more effective and patient-specific medical treatments. Integrating robotic systems equipped with visual servo control mechanisms into bioprinting processes addresses the dynamic nature of living tissues. This adaptation marks a critical advancement towards the practical application of bioprinting in real-time, dynamic environments such as surgical settings. Furthermore, the characterization and enhancement of GelMA hydrogel with Cellulose Nanofibrils (CNF) contribute to the ongoing evolution of bioink formulations. By improving the mechanical properties and photopolymerization behavior of GelMA, this study addresses existing limitations while opening new avenues for developing robust and functional tissue constructs.

This thesis addresses critical challenges within the bioprinting field and introduces an interdisciplinary approach with wide-ranging implications in the field of skin bioprinting.

7.2 Research Contributions

The research objectives outlined in this study introduce novel approaches and solutions within the bioprinting domain. Following is an objective-based summary of the contributions made during the course of this study:

7.2.1 Development of a Free-Form Toolpath Generation for Skin Implant

Chapter 3 of the dissertation, titled "Bioprinting on Non-Planar Surfaces," deals with the challenge in adapting bioprinting techniques for non-planar and non-traditional environments. This chapter bridges traditional bioprinting approaches with methodologies that cater to the complexities of printing directly onto foreign platforms e.g., the human body in a wound healing scenario. The transition from planar to 3D surface bioprinting necessitated thoroughly exploring software and hardware developments.

To achieve objective I, a novel slicing design and tool path generation algorithm for skin implants was developed [248]. This approach leverages free-form surface slicing to avoid the limitations posed by traditional planar methods, such as the stair-casing effect, enabling the creation of implants with enhanced geometric fit. Furthermore, the construction and implementation of in-situ bioprinting hardware have been realized, featuring capabilities for the precise registration and localization of target printing platforms. This directly addresses the first objective by offering a solution to the limitations of traditional printing approaches.

7.2.1.1 Novelty

The traditional approach to bioprinting primarily involves printing on flat, static surfaces that do not align with the natural contours of the human body. The development of new bioprinting techniques enables depositing biomaterials on non-planar surfaces. This approach aligns more closely with the real-world application of tissue engineering, particularly for skin and other organ surfaces.

7.2.1.2 Limitations of Work

The research under Objective I faced several limitations in advancing bioprinting techniques for non-planar surfaces.

- One issue was the compatibility of materials, particularly when biomaterial was required to adhere to curved or inclined surfaces. The exploration of different biomaterial formulations and additives could provide a solution, enhancing adhesion properties to accommodate complex geometrical shapes.

- The accessibility of printing surfaces was limited by the robotic arms' current design and degrees of freedom. Employing these techniques in robotic arms with an extended range of motion could enhance the applicability of bioprinting technologies, allowing for a wider range of bioprinting applications on various surface geometries.
- The geometry of the printhead, especially in the hydrogel extrusion system, played a crucial role. The study utilized a long conical-shaped nozzle, which, while effective up to a certain extent, restricted the maximum printing depth and surface angle adaptability. A long, conical-shaped nozzle (5 mm in radius and 20 mm in length) restricted the printing depth to a maximum of 15 mm. The nozzle's clearance angle stood at roughly 70°, augmented by an additional clearance of 20°, optimizing it for surfaces inclined up to 30 degrees. However, this configuration limits the effectiveness of the polymer printing head to a depth of merely 5 mm.

7.2.1.3 Publications Related to Bioprinting on Non-Planar Platform

1. M. S. Chaudhry and A. Czekanski, "Surface Slicing and Toolpath Planning for in situ Bioprinting of Skin Implants", in Biofabrication, 16(2), 2024.
2. M. S. Chaudhry and A. Czekanski, "Slicing Procedure for Non-Planar Fused Filament Fabrication," in Progress in Canadian Mechanical Engineering, 4, 2021.
3. M. S. Chaudhry and A. Czekanski, "Tool Path Generation for Free-form Surface Slicing in Additive Manufacturing/Fused Filament Fabrication," in Progress in Canadian Mechanical Engineering, 2B: Advanced Manufacturing, 2021.

7.2.2 Development of Autonomous Robotic Bioprinting System for Moving Surfaces

Chapter 4 focused on the development of robotic systems with visual feedback control for printing on moving surfaces. This approach addresses the limitations of traditional 3D printing by allowing for precise material deposition on moving platforms, a step forward from the constraints of static, planar surfaces common in existing methodologies. Through the development and integration of camera models for real-time tracking and visual servo control mechanisms, the outlines outline a framework for enabling a robotic printer to adapt and compensate for the movements of a non-stationary printing platform.

To achieve objective II, a robotic bioprinting system capable of tracking and adapting to non-cooperative and non-stationary platforms is developed [249]. Implementing the Kalman filter enhanced the predictability and responsiveness of the system to environmental changes, facilitating real-time adjustments during the printing process. An experimental setup validated the effectiveness of the

tracking algorithm and the overall system in maintaining printing quality on moving platforms. The robotic autonomy of the developed system can be positioned between the levels of partial (3) and conditional (4) autonomy in the spectrum of robotic independence. This system's ability to track and adjust to moving platforms in real-time represents a contribution to in-situ bioprinting, particularly for live hosts or environments where stability cannot be assured. The core innovation lies in the real-time parallel synchronization of a very slow image detection module with a high-speed tracking printing control algorithm. This approach allows for instantaneous adjustments and alignment with the platform's movements.

7.2.2.1 Novelty

Integrating robotic systems with visual servo control mechanisms into bioprinting represents a new approach in the field of 3D printing. Unlike static bioprinting, this technology accounts for the movements and changes in the printing base, offering a real-time adaptive printing process. This is particularly relevant for in-situ bioprinting, where the target surface may not be stationary, e.g., for a live biological host.

7.2.2.2 Limitations of Work

The limitations encountered in Objective II primarily revolved around the adaptability of the printing system to moving surfaces.

- The research developed a non-stationary printing approach but was only tested in two degrees of freedom (2D) due to hardware constraints. Developing advanced triangulation techniques is necessary to achieve comprehensive three-dimensional (3D) tracking and printing. However, the study faced challenges with triangulation techniques for full 3D tracking, as errors in the z-coordinate and orientation pose led to unsuccessful prints. These challenges underline the necessity for more refined and precise triangulation methods to enable effective full-motion 3D printing.
- Moreover, compensating fully for all degrees of freedom requires a specialized six degrees of freedom (6D) robotic arm. Although the slicing algorithm developed generates a toolpath in six degrees of freedom, the experimental setup was limited to a four-degree-of-freedom robot, which could only interpret the position parameters of the nozzle. This limitation suggests that while the groundwork has been laid, further advancements in hardware are required to exploit the capabilities of the developed algorithms fully.

- Additionally, controlling and adapting the extrusion rates for different bioinks posed another challenge due to the diversity in bioink properties such as viscosity, flow stress, and temperature sensitivity. An alternative approach, from motor-driven to pneumatic extrusion, could offer a solution by providing more consistent extrusion rates that are suitable for various bioinks.

7.2.2.3 Publications Related to Autonomous Bioprinting on Moving Platform

1. M. S. Chaudhry and A. Czekanski, "Visual Control for Robotic 3D Printing on a Moving Platform," (*accepted*) Mechatronics, 2024
2. M. S. Chaudhry and A. Czekanski, "Visual Control of a Robotic Manipulator for Tracking of an Uncooperative Platform," in Progress in Canadian Mechanical Engineering, 5, 2022.

7.2.3 Development of Bioprinting Material Suitable for In-Situ Bioprinting of Skin

Chapter 5 is dedicated to the characterization and enhancement of GelMA hydrogel with Cellulose Nanofibrils (CNF) and provides an overview of the research conducted to improve the properties of GelMA for bioprinting applications. The addition of CNF to GelMA improved its mechanical and rheological properties, making it suitable for in-situ bioprinting, particularly for skin tissue engineering. Enhanced photopolymerization under visible light indicates potential for more efficient curing processes in bioprinting applications.

To achieve objective III, visible light-based GelMA/CNF composite was developed and characterized [250]. Investigations were made into the enhanced biomaterial's rheological behavior, mechanical integrity, and photo-crosslinking characteristics. This research provided a deeper understanding of GelMA's properties and improved its performance by integrating CNF. The findings confirmed that incorporating CNF into GelMA improved its physical properties and adapted it for bioprinting applications. Moreover, an extensive literature review was conducted, integrating critical insights and current knowledge necessary to advance in-situ skin bioprinting [240].

7.2.3.1 Novelty

The comprehensive characterization and subsequent enhancement of GelMA with CNF present a novel contribution to bioink development. While GelMA is a well-known base for bioinks, its properties have limitations when used in pure form. By systematically studying and then integrating CNF, the research enhances the mechanical properties and photopolymerization behaviors of GelMA, addressing previously identified challenges.

7.2.3.2 Publications Related to Biomaterial Development

1. M. S. Chaudhry and A. Czekanski, "In situ bioprinting of skin - A review," Bioprinting, 31, p. e00271, June 2023.
2. M. S. Chaudhry and A. Czekanski, "Rheological and Mechanical Transformations of Gelatin Methacrylol (GelMA) with Cellulose Nanofibrils," (*under review*) 2024.
3. M. S. Chaudhry, D. M. Solis and A. Czekanski, "Characterization of Visible Light Crosslinked Gelatin Methacryloyl (GelMA)/ Cellulose Nanofibrils (CNF) Bio-printed Constructs," in Biofabrication Society, 2023.

7.2.3.3 Limitations of Work

The limitations encountered in Objective III primarily revolved around the adaptability of the printing system to moving surfaces.

- Objective 3 faced limitations concerning the light sensitivity of GelMA and the photopolymerization process. Minor changes in the manufacturing protocol impacted GelMA's photopolymerization properties. While visible light-induced photopolymerization presents advantages over UV-based methods, especially concerning host cell effects, the proposed method resulted in longer curing times. Therefore, optimizing the crosslinking method to achieve faster curing times is imperative, which is crucial for in-situ bioprinting applications like skin printing.
- Environmental conditions, particularly room temperature, also affect GelMA's printing quality. Strategies to minimize temperature fluctuations were employed, but variations in ambient temperature still impacted print quality. This finding indicates the need for more controlled printing environments to ensure consistent biomaterials behavior.
- Lastly, the study did not extend to verifying cellular viability and regeneration processes using the enhanced GelMA/CNF biomaterial. While the addition of CNF improved the mechanical properties and printability of the biomaterial, the impact on cellular attachment and viability remains unexplored. This gap highlights the importance of conducting comprehensive biological assessments to ensure that the enhanced bioink effectively supports cell growth and tissue regeneration.

7.2.4 System Integration and In-Situ Bioprinting Implementation

Chapter 6, titled "System Integration and Advancements in In-Situ Bioprinting," explores the finalization of the dissertation's goals by showcasing the integration of software and hardware components into an in-situ bioprinting test platform. This chapter highlights the importance of merging the individual technological advancements detailed in the preceding chapters to create an interconnected bioprinting workflow capable of executing complex in-situ printing tasks.

To achieve objective IV, the research combined the non-planar slicing algorithm, autonomous robotic system, and enhanced GelMA/CNF biomaterial into a singular operational framework. This integrated system facilitates precise and adaptive printing on moving, non-planar surfaces, simulating realistic conditions. The developed components highlight the system's potential to advance the capabilities of current bioprinting technologies.

7.2.4.1 Novelty

Traditional bioprinting processes have been confined to laboratory settings, limiting their applicability in real-world medical scenarios. The successful integration of an advanced non-planar bioprinting algorithm with autonomous robotic mechanisms and biomaterial formulations represents a step towards operational in-situ bioprinting. This system exceeds the capabilities of conventional bioprinting systems, offering new opportunities for direct tissue printing on living organisms.

7.2.4.2 Limitations of Work

The research under Objective IV encountered several limitations in the comprehensive integration and autonomous operation of the bioprinting system:

- A key challenge was synchronizing the software and hardware components to operate seamlessly in real-time. Due to different operating frequencies, the asynchronous nature of the tracking and printing systems occasionally led to discrepancies between the planned and actual deposition of biomaterial. Improved synchronization strategies and real-time communication protocols could enhance the coherence between different subsystems.
- While the system demonstrated automated tracking and printing capabilities, its decision-making process in response to unexpected scenarios was limited. The current framework requires predefined parameters and lacks the ability to adapt to unforeseen conditions during the bioprinting process autonomously. Developing advanced algorithms that enable real-time decision-making and adaptive responses could advance the system's autonomy.

- The integration faced limitations due to the physical constraints and scalability of the current hardware setup. The size and design of the robotic arm and printing platform restricted the range and complexity of bioprinting tasks that could be performed. The existing hardware design also constrained the system's scalability to larger or more complex bioprinting projects.

7.2.5 Summary of Contributions

The main contribution of this work are as follows:

(i) Developed a novel slicing algorithm for skin implant modeling, overcoming traditional planar limitations.
(ii) Develop an autonomous bioprinting system using visual servo control to adapt to movement and maintain print quality on non-static surfaces.
(iii) Developed a composite hydrogel integrating cellulose nanofibrils (CNF), optimized for photopolymerization, and adapted for extrusion printing, enhancing its suitability for potential skin bioprinting applications.
(iv) Developed an integrated in-situ bioprinting system to simulate practical skin implant fabrication.

7.3 Future Work

By advancing beyond flat surface bioprinting to accommodate complex anatomical structures, integrating adaptive robotic systems for dynamic environments, and enhancing biomaterial properties for improved performance, the research contributes novel solutions that could impact the field of in-situ bioprinting.

Objective I: Bioprinting on Non-Planar Surfaces

- Future research should focus on developing and testing a variety of biomaterial formulations and additives specifically designed to enhance adhesion on curved and inclined surfaces. This could involve synthesizing new materials or modifying existing ones to ensure compatibility with complex anatomical structures.
- The implementation of more sophisticated algorithms for path planning and collision avoidance is recommended. This will enable the creation of more intricate and precise bioprinting pathways, overcoming current limitations in printing complex structures.

- There is a pressing need to design robotic arms with an extended range of motion and revisit printhead geometry, particularly for hydrogel extrusion systems. Future designs should aim for greater flexibility, allowing deeper and more adaptable printing on variably inclined surfaces.
- Enhancing the localization and alignment strategies for bioprinting on non-planar surfaces is critical. This could involve integrating advanced visual feedback systems to reduce manual positioning errors and improve the accuracy of pose transformations.

Objective II: Bioprinting on Moving Surfaces

- The development of advanced triangulation methods is necessary to enable accurate 3D tracking and printing. Future work should address stabilizing z-coordinate and orientation measurements to facilitate successful full-motion 3D printing.
- The acquisition or development of a specialized 6D robotic arm is crucial. This will allow full utilization of the developed slicing algorithms and enable printing with all six degrees of freedom, enhancing the versatility of surface bioprinting.
- Investigating alternative extrusion mechanisms, such as pneumatic systems, could provide more consistent and adaptable extrusion rates for various biomaterials. This would address the current challenges in extrusion rate control due to diverse biomaterial properties.
- Integrate a tactile sensor to dynamically adjust the printing nozzle's force on biological substrates through real-time feedback.

Objective III: Enhancement of GelMA Biomaterial with CNF

- There is a need to optimize the light-induced photopolymerization process to reduce curing times while maintaining or enhancing the hydrogel's structural integrity. This optimization is crucial for efficient in-situ bioprinting applications, particularly for skin printing.
- Future studies should explore more controlled and stable printing environments to mitigate the effects of ambient temperature fluctuations on biomaterial behavior. This could involve the development of specialized printing chambers or environmental controls.
- Comprehensive biological assessments of the enhanced GelMA/CNF are necessary to verify its suitability for supporting cell growth, tissue regeneration, and long-term biodegradability. Future work should evaluate cellular viability, attachment, and proliferation within the hydrogel matrix to ensure its effectiveness for regenerative medicine applications.
- Future research should focus on expanding the in-vivo studies to assess the GelMA/CNF composite's performance in actual biological environments, including its interaction with different cell types and its long-term biodegradability.

- Additionally, studies should aim to understand the molecular mechanisms underlying the improved properties of GelMA/CNF composites to enable the design of even more effective materials for bioprinting applications.

Objective IV: System Integration and Autonomous Robotic Bioprinting

- Future research should aim to develop advanced synchronization mechanisms between the tracking and printing systems. Implementing real-time adaptive algorithms that can dynamically adjust to changes in tracking data could improve the coherence between the camera feedback and printer actions. This includes exploring real-time operating systems (RTOS) for tighter control loops and integrating predictive models to pre-emptively adjust printing parameters based on anticipated movements.
- Developing higher-level autonomous functionalities within the bioprinting system could be an area of future work. This involves integrating machine learning and artificial intelligence algorithms to enable the system to make real-time decisions and adapt to unexpected conditions during the bioprinting process. This could include the development of algorithms for automatic error detection and correction, material flow optimization, and adaptive path planning based on the immediate bioprinting environment.
- Future efforts should focus on designing a more modular and scalable bioprinting system. This could involve creating interchangeable parts, such as printheads with different functionalities, and developing a more flexible robotic arm design to accommodate a wider range of motions and applications.

References

[1] P. Nayyeri, K. Zareinia and H. Bougherara, "Planar and nonplanar slicing algorithms for fused deposition modeling technology: a critical review," *The International Journal of Advanced Manufacturing Technology,* vol. 119, p. 2785–2810, January 2022.

[2] D. Stanco, P. Urban, S. Tirendi, G. Ciardelli and J. Barrero, "3D bioprinting for orthopaedic applications: Current advances, challenges and regulatory considerations," *Bioprinting (Amsterdam, Netherlands),* vol. 20, pp. None - None, 2020.

[3] S. Murphy, P. de Coppi and A. Atala, "Opportunities and challenges of translational 3D bioprinting," *Nature Biomedical Engineering,* vol. 4, pp. 370-380, 2019.

[4] W.-x. Zhou, Z. Qiao, E. N. Zare, J.-f. Huang, X.-Q. Zheng, X. Sun, M. Shao, H. Wang, X. Wang, D. Chen, J. Zheng, S. Fang, Y. Li, X. Zhang, L. Yang, P. Makvandi and A. Wu, "4 D-Printed Dynamic Materials in Biomedical Applications: Chemistry, Challenges, and Their Future Perspectives in the Clinical Sector.," *Journal of medicinal chemistry,* 2020.

[5] D. Song, Y. Xu, S. Liu, L. Wen and X. Wang, "Progress of 3D Bioprinting in Organ Manufacturing," *Polymers,* vol. 13, 2021.

[6] E. M. Tottoli, R. Dorati, I. Genta, E. Chiesa, S. Pisani and B. Conti, "Skin Wound Healing Process and New Emerging Technologies for Skin Wound Care and Regeneration," *Pharmaceutics,* vol. 12, 2020.

[7] A. J. MacAdam, E. Chaudry, C. D. McTiernan, D. Cortes, E. Suuronen and E. Alarcon, "Development of in situ bioprinting: A mini review," *Frontiers in Bioengineering and Biotechnology,* vol. 10, 2022.

[8] A. Kengelbach-Weigand, C. Thielen, T. Bäuerle, R. Götzl, T. Gerber, C. Körner, J. Beier, R. Horch and A. Boos, "Personalized medicine for reconstruction of critical-size bone defects – a translational approach with customizable vascularized bone tissue," *NPJ Regenerative Medicine,* vol. 6, 2021.

[9] L. Bertassoni, "Bioprinting of Complex Multicellular Organs with Advanced Functionality—Recent Progress and Challenges Ahead," *Advanced Materials,* vol. 34, 2021.

[10] H. Dong, B. Hu, W. Zhang, W. Xie, J. Mo, H. Sun and J. Shang, "Robotic-assisted automated in situ bioprinting," *International Journal of Bioprinting,* vol. 9, 2022.

[11] I. Matai, G. Kaur, A. Seyedsalehi, A. McClinton and C. Laurencin, "Progress in 3D bioprinting technology for tissue/organ regenerative engineering.," *Biomaterials,* vol. 226, p. 119536 , 2020.

[12] L. Bertassoni, "Bioprinting of Complex Multicellular Organs with Advanced Functionality—Recent Progress and Challenges Ahead," *Advanced Materials,* vol. 34, 2021.

[13] C. Gao, C. Lu, Z. Jian, T. Zhang, Z. Chen, Q. Zhu, Z. Tai and Y. Liu, "3D bioprinting for fabricating artificial skin tissue.," *Colloids and surfaces. B, Biointerfaces,* vol. 208, p. 112041 , 2021.

[14] D. Choudhury, S. Anand and M. Naing, "The arrival of commercial bioprinters–towards 3D bioprinting revolution," *Int. J. Bioprinting,* vol. 4, no. 2, p. 139, 2018.

[15] J. Gopinathan and I. Noh, "Recent trends in bioinks for 3D printing," *Biomaterial Research,* vol. 22, no. 1, pp. 1-15, 2018.

[16] N. Ashammakhi, S. Ahadian, I. Pountos, S.-K. Hu, N. Tellisi, P. Bandaru, S. Ostrovidov, M. R. Dokmeci and A. Khademhosseini, "In situ three-dimensional printing for reparative and regenerative therapy," *Biomedical Microdevices,* vol. 21, April 2019.

[17] S. Murphy and A. Atala, "3D bioprinting of tissues and organs," *Nature Biotechnology,* vol. 32, pp. 773-785, 2014.

[18] N. Hakimi, R. Cheng, L. Leng, M. Sotoudehfar, P. Q. Ba, N. Bakhtyar, S. Amini-Nik, M. G. Jeschke and A. Günther, "Handheld skin printer: in situ formation of planar biomaterials and tissues," *Lab on a Chip,* vol. 18, p. 1440–1451, 2018.

[19] M. Albanna, K. W. Binder, S. V. Murphy, J. Kim, S. A. Qasem, W. Zhao, J. Tan, I. B. El-Amin, D. D. Dice, J. Marco, J. Green, T. Xu, A. Skardal, J. H. Holmes, J. D. Jackson, A. Atala and J. J. Yoo, "In Situ Bioprinting of Autologous Skin Cells Accelerates Wound Healing of Extensive Excisional Full-Thickness Wounds," *Scientific Reports,* vol. 9, February 2019.

[20] Y. Tianyuan, Z. Yi, J. Zhian and L. Yuanyuan, "A Novel Handheld Device: Application to in Situ Bioprinting Compound Dressing for the Treatment of Wound," *Journal of Physics: Conference Series,* vol. 1965, p. 012059, July 2021.

[21] K. W. Binder, W. Zhao, T. Aboushwareb, D. Dice, A. Atala and J. J. Yoo, "In situ bioprinting of the skin for burns," *Journal of the American College of Surgeons,* vol. 211, p. S76, September 2010.

[22] K. W. Binder, *In Situ Bioprinting of the Skin,* 2011.

[23] M. Sheikholeslam, M. E. E. Wright, M. G. Jeschke and S. Amini-Nik, "Biomaterials for Skin Substitutes," *Advanced Healthcare Materials,* vol. 7, p. 1700897, December 2017.

[24] P. Pleguezuelos-Beltrán, P. Gálvez-Martín, D. Nieto-García, J. A. Marchal and E. López-Ruiz, "Advances in spray products for skin regeneration," *Bioactive Materials,* vol. 16, p. 187–203, October 2022.

[25] M. Wang, J. He, Y. Liu, M. Li, D. Li and Z. Jin, "The trend towards in vivo bioprinting," *International Journal of Bioprinting,* July 2015.

[26] S. Singh, D. Choudhury, F. Yu, V. Mironov and M. W. Naing, "In situ bioprinting – Bioprinting from benchside to bedside?," *Acta Biomaterialia,* vol. 101, p. 14–25, January 2020.

[27] P. G. Campbell and L. E. Weiss, "Tissue engineering with the aid of inkjet printers," *Expert Opinion on Biological Therapy,* vol. 7, p. 1123–1127, August 2007.

[28] M. H. Murdock and S. F. Badylak, "Biomaterials-based in situ tissue engineering," *Current Opinion in Biomedical Engineering,* vol. 1, p. 4–7, March 2017.

[29] K. Kahin, Z. Khan, M. Albagami, S. Usman, S. Bahnshal, H. Alwazani, M. A. Majid, S. Rauf and C. Hauser, "Development of a robotic 3D bioprinting and microfluidic pumping system for tissue and organ engineering," in *Microfluidics, BioMEMS, and Medical Microsystems XVII*, 2019.

[30] L. Leng, S. Amini-Nik, Q. Ba, M. G. Jeschke and A. Günther, "Skin Printer : Microfluidic Approach For Skin Regeneration and Wound Dressings," 2013.

[31] M. Hoffman, *The skin (human anatomy): Picture, definition, function, and skin conditions,* WebMD.

[32] J. M. Abdo, N. A. Sopko and S. M. Milner, "The applied anatomy of human skin: A model for regeneration," *Wound Medicine,* vol. 28, p. 100179, March 2020.

[33] A. Kalra and A. Lowe, "Mechanical Behaviour of Skin: A Review," *Journal of Material Science & Engineering,* vol. 5, 2016.

[34] M. Pawlaczyk, M. Lelonkiewicz and M. Wieczorowski, "Age-dependent biomechanical properties of the skin," *Advances in Dermatology and Allergology,* vol. 5, p. 302–306, 2013.

[35] J. van Kuilenburg, M. A. Masen and E. van der Heide, "Contact modelling of human skin: What value to use for the modulus of elasticity?," *Proceedings of the Institution of Mechanical Engineers, Part J: Journal of Engineering Tribology,* vol. 227, p. 349–361, November 2012.

[36] J. R. Yu, J. Navarro, J. C. Coburn, B. Mahadik, J. Molnar, J. H. Holmes, A. J. Nam and J. P. Fisher, "Current and Future Perspectives on Skin Tissue Engineering: Key Features of Biomedical Research, Translational Assessment, and Clinical Application," *Advanced Healthcare Materials,* vol. 8, p. 1801471, February 2019.

[37] S. MacNeil, "Progress and opportunities for tissue-engineered skin," *Nature,* vol. 445, p. 874–880, February 2007.

[38] S. Diridollou, M. Berson, V. Vabre, D. Black, B. Karlsson, F. Auriol, J. M. Gregoire, C. Yvon, L. Vaillant, Y. Gall and F. Patat, "An In Vivo Method for Measuring the Mechanical Properties of the Skin Using Ultrasound," *Ultrasound in Medicine & Biology,* vol. 24, pp. 215-224, 1998.

[39] G. Boyer, C. Pailler Mattei, J. Molimard, M. Pericoi, S. Laquieze and H. Zahouani, "Non contact method for in vivo assessment of skin mechanical properties for assessing effect of ageing," *Medical Engineering & Physics,* vol. 34, p. 172–178, March 2012.

[40] Y. Wang, R. Xu, W. He, Z. Yao, H. Li, J. Zhou, J. Tan, S. Yang, R. Zhan, G. Luo and J. Wu, "Three-Dimensional Histological Structures of the Human Dermis," *Tissue Engineering Part C: Methods,* vol. 21, p. 932–944, September 2015.

[41] L. Belk, N. Tellisi, H. Macdonald, A. Erdem, N. Ashammakhi and I. Pountos, "Safety Considerations in 3D Bioprinting Using Mesenchymal Stromal Cells," *Frontiers in Bioengineering and Biotechnology,* vol. 8, October 2020.

[42] A. Matsiko, J. P. Gleeson and F. J. O'Brien, "Scaffold Mean Pore Size Influences Mesenchymal Stem Cell Chondrogenic Differentiation and Matrix Deposition," *Tissue Engineering Part A*, vol. 21, p. 486–497, February 2015.

[43] R. Augustine, "Skin bioprinting: a novel approach for creating artificial skin from synthetic and natural building blocks," *Progress in Biomaterials*, vol. 7, p. 77–92, May 2018.

[44] M. F. Griffin, B. C. Leung, Y. Premakumar, M. Szarko and P. E. Butler, "Comparison of the mechanical properties of different skin sites for auricular and nasal reconstruction," *Journal of Otolaryngology - Head & Neck Surgery*, vol. 46, April 2017.

[45] A. Ní Annaidh, K. Bruyère, M. Destrade, M. D. Gilchrist and M. Otténio, "Characterization of the anisotropic mechanical properties of excised human skin," *Journal of the Mechanical Behavior of Biomedical Materials*, vol. 5, p. 139–148, January 2012.

[46] C. Jacquemoud, K. Bruyere-Garnier and M. Coret, "Methodology to determine failure characteristics of planar soft tissues using a dynamic tensile test," *Journal of Biomechanics*, vol. 40, p. 468–475, January 2007.

[47] A. J. Gallagher, A. N. Annaidh, K. Bruyère and et al., *Dynamic Tensile Properties of Human Skin*, 2012.

[48] M. Ottenio, D. Tran, A. Ní Annaidh, M. D. Gilchrist and K. Bruyère, "Strain rate and anisotropy effects on the tensile failure characteristics of human skin," *Journal of the Mechanical Behavior of Biomedical Materials*, vol. 41, p. 241–250, January 2015.

[49] H. Joodaki and M. B. Panzer, "Skin mechanical properties and modeling: A review," *Proceedings of the Institution of Mechanical Engineers, Part H: Journal of Engineering in Medicine*, vol. 232, p. 323–343, March 2018.

[50] B. Holt, A. Tripathi and J. Morgan, "Viscoelastic response of human skin to low magnitude physiologically relevant shear," *Journal of Biomechanics*, vol. 41, p. 2689–2695, August 2008.

[51] Y. Wang, X. Yuan, B. Yao, S. Zhu, P. Zhu and S. Huang, "Tailoring bioinks of extrusion-based bioprinting for cutaneous wound healing," *Bioactive Materials*, vol. 17, p. 178–194, November 2022.

[52] R. Augustine, N. Kalarikkal and S. Thomas, "Effect of zinc oxide nanoparticles on thein vitrodegradation of electrospun polycaprolactone membranes in simulated body fluid,"

International Journal of Polymeric Materials and Polymeric Biomaterials, vol. 65, p. 28–37, September 2015.

[53] A. GhavamiNejad, N. Ashammakhi, X. Y. Wu and A. Khademhosseini, "3D Bioprinting: Crosslinking Strategies for 3D Bioprinting of Polymeric Hydrogels (Small 35/2020)," *Small*, vol. 16, p. 2070195, September 2020.

[54] W. Hu, Z. Wang, Y. Xiao, S. Zhang and J. Wang, "Advances in crosslinking strategies of biomedical hydrogels," *Biomaterials Science,* vol. 7, p. 843–855, 2019.

[55] A. Oryan, A. Kamali, A. Moshiri, H. Baharvand and H. Daemi, "Chemical crosslinking of biopolymeric scaffolds: Current knowledge and future directions of crosslinked engineered bone scaffolds," *International Journal of Biological Macromolecules,* vol. 107, p. 678–688, February 2018.

[56] T. R. Kyriakides, "Molecular Events at Tissue–Biomaterial Interface," in *Host Response to Biomaterials*, Elsevier, 2015, p. 81–116.

[57] E. Ajami, E. Mahno, V. C. Mendes, S. Bell, R. Moineddin and J. E. Davies, "Bone healing and the effect of implant surface topography on osteoconduction in hyperglycemia," *Acta Biomaterialia,* vol. 10, p. 394–405, January 2014.

[58] Y. Zhu, H. Liang, X. Liu, J. Wu, C. Yang, T. M. Wong, K. Y. H. Kwan, K. M. C. Cheung, S. Wu and K. W. K. Yeung, "Regulation of macrophage polarization through surface topography design to facilitate implant-to-bone osteointegration," *Science Advances,* vol. 7, April 2021.

[59] C. H. Lee, E. K. Moioli and J. J. Mao, "Fibroblastic Differentiation of Human Mesenchymal Stem Cells using Connective Tissue Growth Factor," in *2006 International Conference of the IEEE Engineering in Medicine and Biology Society*, 2006.

[60] X. Gao, M. Fraulob and G. Haïat, "Biomechanical behaviours of the bone–implant interface: a review," *Journal of The Royal Society Interface,* vol. 16, p. 20190259, July 2019.

[61] G. Haïat, H.-L. Wang and J. Brunski, "Effects of Biomechanical Properties of the Bone–Implant Interface on Dental Implant Stability: From In Silico Approaches to the Patient's Mouth," *Annual Review of Biomedical Engineering,* vol. 16, p. 187–213, July 2014.

[62] R. Londono and S. F. Badylak, "Factors Which Affect the Host Response to Biomaterials," in *Host Response to Biomaterials*, Elsevier, 2015, p. 1–12.

[63] K. Sadtler, A. Singh, M. T. Wolf, X. Wang, D. M. Pardoll and J. H. Elisseeff, "Design, clinical translation and immunological response of biomaterials in regenerative medicine," *Nature Reviews Materials,* vol. 1, June 2016.

[64] M. E. Scarritt, R. Londono and S. F. Badylak, "Host Response to Implanted Materials and Devices: An Overview," in *The Immune Response to Implanted Materials and Devices*, Springer International Publishing, 2016, p. 1–14.

[65] J. M. Anderson and S. Jiang, "Implications of the Acute and Chronic Inflammatory Response and the Foreign Body Reaction to the Immune Response of Implanted Biomaterials," in *The Immune Response to Implanted Materials and Devices*, Springer International Publishing, 2016, p. 15–36.

[66] J. O. Abaricia, N. Farzad, T. J. Heath, J. Simmons, L. Morandini and R. Olivares-Navarrete, "Control of innate immune response by biomaterial surface topography, energy, and stiffness," *Acta Biomaterialia,* vol. 133, p. 58–73, October 2021.

[67] S. T. Lopresti and B. N. Brown, "Host Response to Naturally Derived Biomaterials," in *Host Response to Biomaterials*, Elsevier, 2015, p. 53–79.

[68] B. D. Ratner, "The Biocompatibility of Implant Materials," in *Host Response to Biomaterials*, Elsevier, 2015, p. 37–51.

[69] R. M. Boehler, J. G. Graham and L. D. Shea, "Tissue engineering tools for modulation of the immune response," *BioTechniques,* vol. 51, p. 239–254, October 2011.

[70] Y. Asawa, T. Sakamoto, M. Komura, M. Watanabe, S. Nishizawa, Y. Takazawa, T. Takato and K. Hoshi, "Early Stage Foreign Body Reaction against Biodegradable Polymer Scaffolds Affects Tissue Regeneration during the Autologous Transplantation of Tissue-Engineered Cartilage in the Canine Model," *Cell Transplantation,* vol. 21, p. 1431–1442, July 2012.

[71] L. Felländer-Tsai, F. P. Reinholt and I. Turan, "Complications with infection and foreign body reaction after silicon implant arthroplasty in the second metatarsophalangeal joint in an adolescent: A case report," *The Journal of Foot and Ankle Surgery,* vol. 36, pp. 452-456, 1997.

[72] B. Gaudillière, G. K. Fragiadakis, R. V. Bruggner, M. Nicolau, R. Finck, M. Tingle, J. Silva, E. A. Ganio, C. G. Yeh, W. J. Maloney, J. I. Huddleston, S. B. Goodman, M. M. Davis, S. C.

Bendall, W. J. Fantl, M. S. Angst and G. P. Nolan, "Clinical recovery from surgery correlates with single-cell immune signatures," *Science Translational Medicine,* vol. 6, September 2014.

[73] S. Reinke, S. Geissler, W. R. Taylor, K. Schmidt-Bleek, K. Juelke, V. Schwachmeyer, M. Dahne, T. Hartwig, L. Akyüz, C. Meisel, N. Unterwalder, N. B. Singh, P. Reinke, N. P. Haas, H.-D. Volk and G. N. Duda, "Terminally Differentiated CD8+T Cells Negatively Affect Bone Regeneration in Humans," *Science Translational Medicine,* vol. 5, March 2013.

[74] P. Matzinger, "Friendly and dangerous signals: is the tissue in control?," *Nature Immunology,* vol. 8, p. 11–13, January 2007.

[75] L. Y. Daikuara, X. Chen, Z. Yue, D. Skropeta, F. M. Wood, M. W. Fear and G. G. Wallace, "3D Bioprinting Constructs to Facilitate Skin Regeneration," *Advanced Functional Materials,* vol. 32, p. 2105080, August 2021.

[76] M. D. Shoulders and R. T. Raines, "Collagen Structure and Stability," *Annual Review of Biochemistry,* vol. 78, p. 929–958, June 2009.

[77] M. v. d. Rest, R. Garrone and D. Herbage, "Collagen: A Family of Proteins with many Facets," in *Extracellular Matrix*, Elsevier, 1993, p. 1–67.

[78] C. M. Kielty and M. E. Grant, "The Collagen Family: Structure, Assembly, and Organization in the Extracellular Matrix," in *Connective Tissue and Its Heritable Disorders*, John Wiley & Sons, Inc., p. 159–221.

[79] S. Gorgieva and V. Kokol, "Collagen- vs. Gelatine-Based Biomaterials and Their Biocompatibility: Review and Perspectives," in *Biomaterials Applications for Nanomedicine*, InTech, 2011.

[80] T. L. Bao Ha, T. Minh, D. Nguyen and D. Minh, "Naturally Derived Biomaterials: Preparation and Application," in *Regenerative Medicine and Tissue Engineering*, InTech, 2013.

[81] D. F. Williams, "On the mechanisms of biocompatibility," *Biomaterials,* vol. 29, p. 2941–2953, July 2008.

[82] H. B. Bohidar and S. S. Jena, "Kinetics of sol–gel transition in thermoreversible gelation of gelatin," *The Journal of Chemical Physics,* vol. 98, p. 8970–8977, June 1993.

[83] M. P. Linnes, B. D. Ratner and C. M. Giachelli, "A fibrinogen-based precision microporous scaffold for tissue engineering," *Biomaterials,* vol. 28, p. 5298–5306, December 2007.

[84] K. Schenke-Layland, S. Liebscher and S. L. Layland, "Use of Extracellular Matrix Proteins and Natural Materials in Bioengineering," in *Biomaterials Science*, Elsevier, 2020, p. 401–413.

[85] D. Eyrich, F. Brandl, B. Appel, H. Wiese, G. Maier, M. Wenzel, R. Staudenmaier, A. Goepferich and T. Blunk, "Long-term stable fibrin gels for cartilage engineering," *Biomaterials*, vol. 28, p. 55–65, January 2007.

[86] T. J. Keane, R. Londono, N. J. Turner and S. F. Badylak, "Consequences of ineffective decellularization of biologic scaffolds on the host response," *Biomaterials*, vol. 33, p. 1771–1781, February 2012.

[87] A. Khademhosseini, 3D Bioprinting in Regenerative Engineering, CRC Press, 2018.

[88] R. A. A. Muzzarelli, J. Boudrant, D. Meyer, N. Manno, M. DeMarchis and M. G. Paoletti, "Current views on fungal chitin/chitosan, human chitinases, food preservation, glucans, pectins and inulin: A tribute to Henri Braconnot, precursor of the carbohydrate polymers science, on the chitin bicentennial," *Carbohydrate Polymers*, vol. 87, p. 995–1012, January 2012.

[89] D. F. Coutinho, S. Sant, M. Shakiba, B. Wang, M. E. Gomes, N. M. Neves, R. L. Reis and A. Khademhosseini, "Microfabricated photocrosslinkable polyelectrolyte-complex of chitosan and methacrylated gellan gum," *Journal of Materials Chemistry*, vol. 22, p. 17262, 2012.

[90] J.-M. Rabanel, N. Bertrand, S. Sant, S. Louati and P. Hildgen, "Polysaccharide Hydrogels for the Preparation of Immunoisolated Cell Delivery Systems," in *ACS Symposium Series*, American Chemical Society, 2006, p. 305–339.

[91] P. J. VandeVord, H. W. T. Matthew, S. P. DeSilva, L. Mayton, B. Wu and P. H. Wooley, "Evaluation of the biocompatibility of a chitosan scaffold in mice," *Journal of Biomedical Materials Research*, vol. 59, p. 585–590, December 2001.

[92] K. Kaladhar and C. P. Sharma, "Supported Cell Mimetic Monolayers and Their Interaction with Blood," *Langmuir*, vol. 20, p. 11115–11122, November 2004.

[93] N. Wu, Z.-S. Wen, X.-W. Xiang, Y.-N. Huang, Y. Gao and Y.-L. Qu, "Immunostimulative Activity of Low Molecular Weight Chitosans in RAW264.7 Macrophages," *Marine Drugs*, vol. 13, p. 6210–6225, September 2015.

[94] F.-L. Mi, Y.-C. Tan, H.-F. Liang and H.-W. Sung, "In vivo biocompatibility and degradability of a novel injectable-chitosan-based implant," *Biomaterials*, vol. 23, p. 181–191, January 2002.

[95] J. Berger, M. Reist, J. M. Mayer, O. Felt, N. A. Peppas and R. Gurny, "Structure and interactions in covalently and ionically crosslinked chitosan hydrogels for biomedical applications," *European Journal of Pharmaceutics and Biopharmaceutics*, vol. 57, p. 19–34, January 2004.

[96] T. Freier, H. S. Koh, K. Kazazian and M. S. Shoichet, "Controlling cell adhesion and degradation of chitosan films by N-acetylation," *Biomaterials*, vol. 26, p. 5872–5878, October 2005.

[97] M. I. Neves, L. Moroni and C. C. Barrias, "Modulating Alginate Hydrogels for Improved Biological Performance as Cellular 3D Microenvironments," *Frontiers in Bioengineering and Biotechnology*, vol. 8, June 2020.

[98] K. Sarkar, Y. Xue and S. Sant, "Host Response to Synthetic Versus Natural Biomaterials," in *The Immune Response to Implanted Materials and Devices*, Springer International Publishing, 2016, p. 81–105.

[99] C. Termeer, J. P. Sleeman and J. C. Simon, "Hyaluronan – magic glue for the regulation of the immune response?," *Trends in Immunology*, vol. 24, p. 112–114, March 2003.

[100] E. Puré and C. A. Cuff, "A crucial role for CD44 in inflammation," *Trends in Molecular Medicine*, vol. 7, p. 213–221, May 2001.

[101] J. E. Rayahin, J. S. Buhrman, Y. Zhang, T. J. Koh and R. A. Gemeinhart, "High and Low Molecular Weight Hyaluronic Acid Differentially Influence Macrophage Activation," *ACS Biomaterials Science & Engineering*, vol. 1, p. 481–493, June 2015.

[102] M. N. Collins and C. Birkinshaw, "Hyaluronic acid based scaffolds for tissue engineering—A review," *Carbohydrate Polymers*, vol. 92, p. 1262–1279, February 2013.

[103] R.-Z. Lin, Y.-C. Chen, R. Moreno-Luna, A. Khademhosseini and J. Melero-Martin, "Transdermal regulation of vascular network bioengineering using a photopolymerizable methacrylated gelatin hydrogel.," *Biomaterials*, vol. 34 28, pp. 6785-96, 2013.

[104] H. Xu, J. Casillas, S. Krishnamoorthy and C. Xu, "Effects of Irgacure 2959 and lithium phenyl-2, 4, 6-trimethylbenzoylphosphinate on cell viability, physical properties, and microstructure in 3D bioprinting of vascular-like constructs," *Biomedical Materials*, vol. 15, p. 055021, August 2020.

[105] J. Lee, R. Prud'homme and I. Aksay, "Cure depth in photopolymerization: Experiments and theory," *Journal of Materials Research,* vol. 16, pp. 3536-3544, 2001.

[106] Z. Wang, H. Kumar, Z. Tian, X. Jin, J. F. Holzman, F. Menard and K. Kim, "Visible Light Photoinitiation of Cell-Adhesive Gelatin Methacryloyl Hydrogels for Stereolithography 3D Bioprinting," *ACS Applied Materials: Interfaces,* vol. 10, p. 26859–26869, July 2018.

[107] H. Kumar, K. Sakthivel, M. G. A. Mohamed, E. Boras, S. Shin and K. Kim, "Designing Gelatin Methacryloyl (GelMA)-Based Bioinks for Visible Light Stereolithographic 3D Biofabrication.," *Macromolecular bioscience,* p. e2000317, 2020.

[108] C. O'Connell, B. Zhang, C. Onofrillo, S. Duchi, R. Blanchard, A. Quigley, J. Bourke, S. Gambhir, R. Kapsa, C. di Bella, P. Choong and G. Wallace, "Tailoring the mechanical properties of gelatin methacryloyl hydrogels through manipulation of the photocrosslinking conditions.," *Soft matter,* vol. 14 11, pp. 2142-2151, 2018.

[109] I. Noshadi, S. Hong, K. E. Sullivan, E. S. Sani, R. Portillo-Lara, A. Tamayol, S. R. Shin, A. E. Gao, W. L. Stoppel, I. I. I. Lauren D. Black, A. Khademhosseini and N. Annabi, "In vitro and in vivo analysis of visible light crosslinkable gelatin methacryloyl (GelMA) hydrogels," *Biomaterials Science,* vol. 5, p. 2093–2105, 2017.

[110] W. T. Han, T.-S. Jang, S. Chen, L. Chong, H.-D. Jung and J. Song, "Improved cell viability for large-scale biofabrication with photo-crosslinkable hydrogel systems through a dual-photoinitiator approach.," *Biomaterials science,* 2019.

[111] M. Zhou, B. Lee and L. P. Tan, "A dual crosslinking strategy to tailor rheological properties of gelatin methacryloyl," *International Journal of Bioprinting,* vol. 3, 2017.

[112] O. Bas, E. M. D. Juan-Pardo, M. P. Chhaya, F. M. Wunner, J. E. Jeon, T. J. Klein and D. W. Hutmacher, "Enhancing structural integrity of hydrogels by using highly organised melt electrospun fibre constructs," *European Polymer Journal,* vol. 72, p. 451–463, November 2015.

[113] H. Dong, J. P. Snyder, K. S. Williams and J. Andzelm, "Cation-induced hydrogels of cellulose nanofibrils with tunable moduli," *Biomacromolecules,* vol. 14, no. 9, pp. 3338-3345, 2013.

[114] M. Vergara-Barberán, Ó. Mompó-Roselló, J. M. Herrero-Martínez and E. F. Simó-Alfonso, "Poly(ethylene glycol) diacrylate based monolithic capillary columns for the analysis of polar

small solutes by capillary electrochromatography," *Journal of Separation Science,* vol. 41, no. 12, pp. 2632-2639, 2018.

[115] L. Gu, T. Li, X. Song, X. Yang, S. Li, L. Chen, P. Liu, X. Gong, C. Chen and L. Sun, "Preparation and characterization of methacrylated gelatin/bacterial cellulose composite hydrogels for cartilage tissue engineering," *Regenerative Biomaterials,* vol. 7, p. 195–202, December 2019.

[116] J. Kucińska-Lipka, I. Gubańska and H. Janik, "Bacterial cellulose in the field of wound healing and regenerative medicine of skin: recent trends and future prospectives," *Polymer Bulletin,* vol. 72, no. 9, pp. 2399-2419, 2015.

[117] S. Ahadian, S. Yamada, J. Ramón-Azcón, M. Estili, X. Liang, K. Nakajima, H. Shiku, A. Khademhosseini and T. Matsue, "Hybrid hydrogel-aligned carbon nanotube scaffolds to enhance cardiac differentiation of embryoid bodies," *Acta Biomaterialia,* vol. 31, p. 134–143, February 2016.

[118] H. Dong, J. P. Snyder, K. S. Williams and J. Andzelm, "Cation-induced hydrogels of cellulose nanofibrils with tunable moduli," *Biomacromolecules,* vol. 14, no. 9, pp. 3338-3345, 2013.

[119] W. Xu, B. Z. Molino, F. Cheng, P. Molino, Z. Yue, D. Su, X. Wang, S. Willför, C. Xu and G. Wallace, "On Low-Concentration Inks Formulated by Nanocellulose Assisted with Gelatin Methacrylate (GelMA) for 3D Printing toward Wound Healing Application," *ACS Applied Materials & Interfaces,* vol. 11, pp. 8838-8848, 2019.

[120] S. Kubota, H. Nishikiori, N. Tanaka, M. Endo and T. Fujii, "Dispersion of acid-treated carbon nanofibers into gel matrices prepared by the sol-gel method.," *The journal of physical chemistry. B,* vol. 109 49, pp. 23170-4, 2005.

[121] C. O'Connell, J. Ren, L. Pope, Y. Zhang, A. Mohandas, R. Blanchard, S. Duchi and C. Onofrillo, "Characterizing Bioinks for Extrusion Bioprinting: Printability and Rheology," in *Methods in Molecular Biology*, Springer US, 2020, p. 111–133.

[122] N. Gasek and D. J. Weiss, "Effect of temperature on gelation and cross-linking of gelatin methacryloyl for biomedical applications," *Physics of Fluids,* vol. 32, p. 033102, March 2020.

[123] M. S. Hu, Z. N. Maan, J.-C. Wu, R. C. Rennert, W. X. Hong, T. S. Lai, A. T. M. Cheung, G. G. Walmsley, M. T. Chung, A. McArdle, M. T. Longaker and H. P. Lorenz, "Tissue Engineering

and Regenerative Repair in Wound Healing," *Annals of Biomedical Engineering*, vol. 42, p. 1494–1507, May 2014.

[124] G. C. Gurtner, S. Werner, Y. Barrandon and M. T. Longaker, "Wound repair and regeneration," *Nature*, vol. 453, p. 314–321, May 2008.

[125] M. Peck, J. Molnar and D. Swart, "A global plan for burn prevention and care," *Bulletin of the World Health Organization*, vol. 87, p. 802–803, October 2009.

[126] D. P. Orgill and R. Ogawa, "Current Methods of Burn Reconstruction," *Plastic and Reconstructive Surgery*, vol. 131, p. 827e–836e, May 2013.

[127] M. Loss, V. Wedler, W. Künzi, C. Meuli-Simmen and V. E. Meyer, "Artificial skin, split-thickness autograft and cultured autologous keratinocytes combined to treat a severe burn injury of 93% of TBSA," *Burns*, vol. 26, p. 644–652, November 2000.

[128] D. G. M. Coppens, S. de Wilde, H. J. Guchelaar, M. L. De Bruin, H. G. M. Leufkens, P. Meij and J. Hoekman, "A decade of marketing approval of gene and cell-based therapies in the United States, European Union and Japan: An evaluation of regulatory decision-making," *Cytotherapy*, vol. 20, p. 769–778, June 2018.

[129] G. Han and R. Ceilley, "Chronic Wound Healing: A Review of Current Management and Treatments," *Advances in Therapy*, vol. 34, p. 599–610, January 2017.

[130] B. ter Horst, G. Chouhan, N. S. Moiemen and L. M. Grover, "Advances in keratinocyte delivery in burn wound care," *Advanced Drug Delivery Reviews*, vol. 123, p. 18–32, January 2018.

[131] A. W. C. Chua, C. F. Saphira and S. J. Chong, "Skin Tissue Engineering in Severe Burns: A Review on Its Therapeutic Applications," in *Regenerative Medicine and Plastic Surgery*, Springer International Publishing, 2019, p. 117–136.

[132] N. J. Turner and S. F. Badylak, "The Use of Biologic Scaffolds in the Treatment of Chronic Nonhealing Wounds," *Advances in Wound Care*, vol. 4, p. 490–500, August 2015.

[133] M. S. Hu, M. R. Borrelli, H. P. Lorenz, M. T. Longaker and D. C. Wan, "Mesenchymal Stromal Cells and Cutaneous Wound Healing: A Comprehensive Review of the Background, Role, and Therapeutic Potential," *Stem Cells International*, vol. 2018, p. 1–13, 2018.

[134] J. Still, P. Glat, P. Silverstein, J. Griswold and D. Mozingo, "The use of a collagen sponge/living cell composite material to treat donor sites in burn patients," *Burns,* vol. 29, p. 837–841, December 2003.

[135] D. Popp, C. Tapking and L. K. Branski, "Skin Substitutes for Burn Wounds," in *Regenerative Medicine and Plastic Surgery*, Springer International Publishing, 2019, p. 137–146.

[136] L. I. Bernstam, F. L. Vaughan and I. A. Bernstein, "Keratinocytes grown at the air-liquid interface," *In Vitro Cellular & Developmental Biology,* vol. 22, p. 695–705, December 1986.

[137] T. Uchino, T. Takezawa and Y. Ikarashi, "Reconstruction of three-dimensional human skin model composed of dendritic cells, keratinocytes and fibroblasts utilizing a handy scaffold of collagen vitrigel membrane," *Toxicology in Vitro,* vol. 23, p. 333–337, March 2009.

[138] M. Sakamoto, N. Morimoto, S. Ogino, C. Jinno, T. Taira and S. Suzuki, "Efficacy of gelatin gel sheets in sustaining the release of basic fibroblast growth factor for murine skin defects," *Journal of Surgical Research,* vol. 201, p. 378–387, April 2016.

[139] S. G. Llames, M. Del Rio, F. Larcher, E. García, M. García, M. José Escamez, J. L. Jorcano, P. Holguín and A. Meana, "Human plasma as a dermal scaffold for the generation of a completely autologous bioengineered skin," *Transplantation,* vol. 77, p. 350–355, February 2004.

[140] S. Xu, L. Sang, Y. Zhang, X. Wang and X. Li, "Biological evaluation of human hair keratin scaffolds for skin wound repair and regeneration," *Materials Science and Engineering: C,* vol. 33, p. 648–655, March 2013.

[141] J. Wang, S. Song, L. Shi, Q. Zhu, C. Ma, X. Tan, Y. Ding and Z. Niu, "Correction: Temporal Expression of Pelp1 during Proliferation and Osteogenic Differentiation of Rat Bone Marrow Mesenchymal Stem Cells," *PLoS ONE,* vol. 8, December 2013.

[142] L. Zaulyanov and R. S. Kirsner, "A review of a bi-layered living cell treatment (Apligraf?) in the treatment of venous leg ulcers and diabetic foot ulcers," *Clinical Interventions in Aging,* vol. 2, p. 93–98, March 2007.

[143] J. C. Coburn, S. Brody, K. L. Billiar and A. Pandit, "Biaxial mechanical evaluation of cholecyst-derived extracellular matrix: A weakly anisotropic potential tissue engineered biomaterial," *Journal of Biomedical Materials Research Part A,* vol. 81A, p. 250–256, April 2007.

[144] F. Hartmann-Fritsch, T. Biedermann, E. Braziulis, J. Luginbühl, L. Pontiggia, S. Böttcher-Haberzeth, T. H. van Kuppevelt, K. A. Faraj, C. Schiestl, M. Meuli and E. Reichmann, "Collagen hydrogels strengthened by biodegradable meshes are a basis for dermo-epidermal skin grafts intended to reconstitute human skin in a one-step surgical intervention," *Journal of Tissue Engineering and Regenerative Medicine,* vol. 10, p. 81–91, December 2012.

[145] S. D. Sarkar, B. L. Farrugia, T. R. Dargaville and S. Dhara, "Chitosan-collagen scaffolds with nano/microfibrous architecture for skin tissue engineering," *Journal of Biomedical Materials Research Part A,* vol. 101, p. 3482–3492, April 2013.

[146] Y. Wang, J. Beekman, J. Hew, S. Jackson, A. C. Issler-Fisher, R. Parungao, S. S. Lajevardi, Z. Li and P. K. M. Maitz, "Burn injury: Challenges and advances in burn wound healing, infection, pain and scarring," *Advanced Drug Delivery Reviews,* vol. 123, p. 3–17, January 2018.

[147] P. J. Matts, V. Alard, M. W. Brown, L. Ferrero, H. Gers-Barlag, N. Issachar, D. Moyal and R. Wolber, "The COLIPAin vitroUVA method: a standard and reproducible measure of sunscreen UVA protection," *International Journal of Cosmetic Science,* vol. 32, p. 35–46, February 2010.

[148] A. Skardal, D. Mack, E. Kapetanovic, A. Atala, J. D. Jackson, J. Yoo and S. Soker, "Bioprinted Amniotic Fluid-Derived Stem Cells Accelerate Healing of Large Skin Wounds," *Stem Cells Translational Medicine,* vol. 1, p. 792–802, October 2012.

[149] A. Nourian Dehkordi, F. Mirahmadi Babaheydari, M. Chehelgerdi and S. Raeisi Dehkordi, "Skin tissue engineering: wound healing based on stem-cell-based therapeutic strategies," *Stem Cell Research & Therapy,* vol. 10, March 2019.

[150] R. Y. Cheng, G. Eylert, J.-M. Gariepy, S. He, H. Ahmad, Y. Gao, S. Priore, N. Hakimi, M. G. Jeschke and A. Günther, "Handheld instrument for wound-conformal delivery of skin precursor sheets improves healing in full-thickness burns," *Biofabrication,* vol. 12, p. 025002, February 2020.

[151] P. Johnstone, J. S.-S. Kwei, G. Filobbos, D. Lewis and S. Jeffery, "Successful application of keratinocyte suspension using autologous fibrin spray," *Burns,* vol. 43, p. e27–e30, May 2017.

[152] J. C. Gerlach, C. Johnen, C. Ottoman, K. Bräutigam, J. Plettig, C. Belfekroun, S. Münch and B. Hartmann, "Method for Autologous Single Skin Cell Isolation for Regenerative Cell Spray

Transplantation with Non-Cultured Cells," *The International Journal of Artificial Organs,* vol. 34, p. 271–279, January 2011.

[153] M. Ueda, "Sprayed Cultured Mucosal Epithelial Cell for Deep Dermal Burns," *Journal of Craniofacial Surgery,* vol. 21, p. 1729–1732, November 2010.

[154] J. C. Gerlach, C. Johnen, E. McCoy, K. Bräutigam, J. Plettig and A. Corcos, "Autologous skin cell spray-transplantation for a deep dermal burn patient in an ambulant treatment room setting," *Burns,* vol. 37, p. e19–e23, June 2011.

[155] B. Hartmann, A. Ekkernkamp, C. Johnen, J. C. Gerlach, C. Belfekroun and M. V. K??ntscher, "Sprayed Cultured Epithelial Autografts for Deep Dermal Burns of the Face and Neck," *Annals of Plastic Surgery,* vol. 58, p. 70–73, January 2007.

[156] L. J. Currie, R. Martin, J. R. Sharpe and S. E. James, "A comparison of keratinocyte cell sprays with and without fibrin glue," *Burns,* vol. 29, pp. 677-685, 2003.

[157] R. Esteban-Vives, M. S. Choi, M. T. Young, P. Over, J. Ziembicki, A. Corcos and J. C. Gerlach, "Second-degree burns with six etiologies treated with autologous noncultured cell-spray grafting," *Burns,* vol. 42, p. e99–e106, November 2016.

[158] F. A. Navarro, M. L. Stoner, C. S. Park, J. C. Huertas, H. B. Lee, F. M. Wood and D. P. Orgill, "Sprayed Keratinocyte Suspensions Accelerate Epidermal Coverage in a Porcine Microwound Model," *Journal of Burn Care & Rehabilitation,* vol. 21, p. 513–518, November 2000.

[159] F. A. Navarro, M. L. Stoner, H. B. Lee, C. S. Park, F. M. Wood and D. P. Orgill, "Melanocyte Repopulation in Full-Thickness Wounds Using a Cell Spray Apparatus," *Journal of Burn Care & Rehabilitation,* vol. 22, p. 41–46, January 2001.

[160] T. Svensjö, F. Yao, B. Pomahac and E. Eriksson, "Autologous Keratinocyte Suspensions Accelerate Epidermal Wound Healing in Pigs," *Journal of Surgical Research,* vol. 99, p. 211–221, August 2001.

[161] I. Grant, K. Warwick, J. Marshall, C. Green and R. Martin, "The co-application of sprayed cultured autologous keratinocytes and autologous fibrin sealant in a porcine wound model," *British Journal of Plastic Surgery,* vol. 55, p. 219–227, April 2002.

[162] D. Kym, H. Yim, J. Yoon, H.-T. Yang, Y. S. Cho, J. Hur, W. Chun and J.-H. Kim, "The application of cultured epithelial autografts improves survival in burns," *Wound Repair and Regeneration,* vol. 23, p. 340–344, May 2015.

[163] H. Lee, "Outcomes of sprayed cultured epithelial autografts for full-thickness wounds: A single-centre experience," *Burns,* vol. 38, p. 931–936, September 2012.

[164] V. Falanga, S. Iwamoto, M. Chartier, T. Yufit, J. Butmarc, N. Kouttab, D. Shrayer and P. Carson, "Autologous Bone Marrow–Derived Cultured Mesenchymal Stem Cells Delivered in a Fibrin Spray Accelerate Healing in Murine and Human Cutaneous Wounds," *Tissue Engineering,* vol. 13, p. 1299–1312, June 2007.

[165] C. Kengla, E. Renteria, C. Wivell, A. Atala, J. J. Yoo and S. J. Lee, "Clinically Relevant Bioprinting Workflow and Imaging Process for Tissue Construct Design and Validation," *3D Printing and Additive Manufacturing,* vol. 4, p. 239–247, December 2017.

[166] D. Y. Park, S.-H. Kim, S.-H. Park, J. S. Jang, J. J. Yoo and S. J. Lee, "3D Bioprinting Strategies for Articular Cartilage Tissue Engineering," *Annals of Biomedical Engineering,* May 2023.

[167] D. Choudhury, S. Anand and M. W. Naing, "The Arrival of Commercial Bioprinters - Towards 3D Bioprinting Revolution!," *International Journal of Bioprinting,* vol. 4, June 2018.

[168] W. Oropallo and L. A. Piegl, "Ten challenges in 3D printing," *Engineering with Computers,* vol. 32, p. 135–148, June 2015.

[169] D. Ahlers, F. Wasserfall, N. Hendrich and J. Zhang, "3D Printing of Nonplanar Layers for Smooth Surface Generation," in *2019 IEEE 15th International Conference on Automation Science and Engineering (CASE)*, 2019.

[170] M. S. Chaudhry and A. Czekanski, "Evaluating FDM Process Parameter Sensitive Mechanical Performance of Elastomers at Various Strain Rates of Loading," *Materials,* vol. 13, p. 3202, July 2020.

[171] S. Chaudhry, M. Al-Dojayli and A. Czekanski, "Performance of 3-D Printed Thermoplastic Polyurethane Under Quasi-Static and High-Strain Rate Loading," in *Volume 9: Mechanics of Solids, Structures and Fluids; NDE, Diagnosis, and Prognosis*, 2016.

[172] A. Dolenc and I. Mäkelä, "Slicing procedures for layered manufacturing techniques," *Computer-Aided Design,* vol. 26, p. 119–126, February 1994.

[173] J. Q. Yan, M. Y. Zhou and J. T. Xi, "Adaptive direct slicing with non-uniform cusp heights for rapid prototyping," *The International Journal of Advanced Manufacturing Technology*, vol. 23, p. 20–27, January 2004.

[174] J. Tyberg and J. Helge Bøhn, "Local adaptive slicing," *Rapid Prototyping Journal,* vol. 4, p. 118–127, September 1998.

[175] D. Ding, Z. Pan, D. Cuiuri, H. Li, N. Larkin and S. van Duin, "Automatic multi-direction slicing algorithms for wire based additive manufacturing," *Robotics and Computer-Integrated Manufacturing,* vol. 37, p. 139–150, February 2016.

[176] H.-m. Zhao, Y. He, J.-z. Fu and J.-j. Qiu, "Inclined layer printing for fused deposition modeling without assisted supporting structure," *Robotics and Computer-Integrated Manufacturing,* vol. 51, p. 1–13, June 2018.

[177] D. Chakraborty, B. Aneesh Reddy and A. Roy Choudhury, "Extruder path generation for Curved Layer Fused Deposition Modeling," *Computer-Aided Design,* vol. 40, p. 235–243, February 2008.

[178] S. Singamneni, A. Roychoudhury, O. Diegel and B. Huang, "Modeling and evaluation of curved layer fused deposition," *Journal of Materials Processing Technology,* vol. 212, p. 27–35, January 2012.

[179] G. M. Fortunato, G. Rossi, A. F. Bonatti, A. D. Acutis, C. Mendoza-Buenrostro, G. Vozzi and C. D. Maria, "Robotic platform and path planning algorithm for in situ bioprinting," *Bioprinting,* vol. 22, p. e00139, June 2021.

[180] G. M. Fortunato, M. Nicoletta, E. Batoni, G. Vozzi and C. D. Maria, "A fully automatic non-planar slicing algorithm for the additive manufacturing of complex geometries," *Additive Manufacturing,* vol. 69, p. 103541, May 2023.

[181] I. E. Yigit, S. A. Khan and I. Lazoglu, "Robotic additive turning with a novel cylindrical slicing method," *The International Journal of Advanced Manufacturing Technology,* vol. 119, p. 7641–7651, January 2022.

[182] I. Mitropoulou, M. Bernhard and B. Dillenburger, "Nonplanar 3D Printing of Bifurcating Forms," *3D Printing and Additive Manufacturing,* vol. 9, p. 189–202, June 2022.

[183] A. Schwab, R. Levato, M. D'Este, S. Piluso, D. Eglin and J. Malda, "Printability and Shape Fidelity of Bioinks in 3D Bioprinting," *Chemical Reviews*, vol. 120, p. 11028–11055, August 2020.

[184] B. J. Albert, C. Wang, C. Williams and J. T. Butcher, "Non-planar embedded 3D printing for complex hydrogel manufacturing," *Bioprinting*, vol. 28, p. e00242, December 2022.

[185] R. R. Ma, J. T. Belter and A. M. Dollar, "Hybrid Deposition Manufacturing: Design Strategies for Multimaterial Mechanisms Via Three-Dimensional Printing and Material Deposition," *Journal of Mechanisms and Robotics*, vol. 7, May 2015.

[186] Z. Zhu, S.-Z. Guo, T. Hirdler, C. Eide, X. Fan, J. Tolar and M. C. McAlpine, "3D Printed Functional and Biological Materials on Moving Freeform Surfaces," *Advanced Materials*, vol. 30, April 2018.

[187] T. Shen, C. A. Nelson, K. Warburton and D. Oleynikov, "Design and Analysis of a Novel Articulated Drive Mechanism for Multifunctional NOTES Robot," *Journal of Mechanisms and Robotics*, vol. 7, February 2015.

[188] L. Kang, W. Kim and B.-J. Yi, "Modeling and Applications of a Family of Five-Degree-of-Freedom Parallel Mechanisms With Kinematic and Actuation Redundancy," *Journal of Mechanisms and Robotics*, vol. 10, July 2018.

[189] F. Gharagozloo, B. Tempesta, M. Meyer, D. Nguyen, S. Gruessner and J. Redan, "History of Robotic Surgery," in *Robotic Surgery*, Springer International Publishing, 2021, p. 21–29.

[190] N. Simaan, R. M. Yasin and L. Wang, "Medical Technologies and Challenges of Robot-Assisted Minimally Invasive Intervention and Diagnostics," *Annual Review of Control, Robotics, and Autonomous Systems*, vol. 1, p. 465–490, May 2018.

[191] A. Banach, M. Strydom, A. Jaiprakash, G. Carneiro, A. Eriksson, R. Crawford and A. McFadyen, "Visual Localisation for Knee Arthroscopy," *International Journal of Computer Assisted Radiology and Surgery*, vol. 16, p. 2137–2145, July 2021.

[192] L. Li, X. Li, B. Ouyang, S. Ding, S. Yang and Y. Qu, "Autonomous Multiple Instruments Tracking for Robot-Assisted Laparoscopic Surgery With Visual Tracking Space Vector Method," *IEEE/ASME Transactions on Mechatronics*, vol. 27, p. 733–743, April 2022.

[193] X. Hu, A. Nguyen and F. R. y Baena, *Occlusion-robust Visual Markerless Bone Tracking for Computer-Assisted Orthopaedic Surgery*, 2021.

[194] C.-Y. Huang and J. Galeotti, "Robust Skin-Feature Tracking in Free-Hand Video from Smartphone or Robot-Held Camera, to Enable Clinical-Tool Localization and Guidance," in *2021 IEEE International Conference on Robotics and Automation (ICRA)*, 2021.

[195] S. Atallah, Ed., Digital Surgery, Springer International Publishing, 2021.

[196] B. Zhao and C. A. Nelson, "Estimating Tool–Tissue Forces Using a 3-Degree-of-Freedom Robotic Surgical Tool," *Journal of Mechanisms and Robotics*, vol. 8, May 2016.

[197] S. Yoshida, T. Kanno and K. Kawashima, "Surgical Robot With Variable Remote Center of Motion Mechanism Using Flexible Structure," *Journal of Mechanisms and Robotics,* vol. 10, April 2018.

[198] Z. Wang, S. Bao, D. Wang, S. Qian, J. Zhang and M. Hai, "Design of a Novel Flexible Robotic Laparoscope Using a Two Degrees-of-Freedom Cable-Driven Continuum Mechanism With Major Arc Notches," *Journal of Mechanisms and Robotics*, vol. 15, January 2023.

[199] A. Dutta, A. Mondal, N. Dey, S. Sen, L. Moraru and A. E. Hassanien, "Vision Tracking: A Survey of the State-of-the-Art," *SN Computer Science*, vol. 1, January 2020.

[200] S. Ji, X. Fan, D. W. Roberts, A. Hartov and K. D. Paulsen, "Cortical surface shift estimation using stereovision and optical flow motion tracking via projection image registration," *Medical Image Analysis*, vol. 18, p. 1169–1183, October 2014.

[201] M. Allan, S. Ourselin, D. J. Hawkes, J. D. Kelly and D. Stoyanov, "3-D Pose Estimation of Articulated Instruments in Robotic Minimally Invasive Surgery," *IEEE Transactions on Medical Imaging*, vol. 37, p. 1204–1213, May 2018.

[202] C. Liu, T. Tosun and M. Yim, "A Low-Cost, Highly Customizable Solution for Position Estimation in Modular Robots," *Journal of Mechanisms and Robotics*, vol. 13, May 2021.

[203] Y.-S. Wang and K.-T. Song, "Image-based Pose Estimation and Tracking of Surgical Instruments in Minimally Invasive Surgery," in *2020 International Automatic Control Conference (CACS)*, 2020.

[204] B. Yang, W.-K. Wong, C. Liu and P. Poignet, "3D soft-tissue tracking using spatial-color joint probability distribution and thin-plate spline model," *Pattern Recognition,* vol. 47, p. 2962–2973, September 2014.

[205] M. Ye, S. Giannarou, A. Meining and G.-Z. Yang, "Online tracking and retargeting with applications to optical biopsy in gastrointestinal endoscopic examinations," *Medical Image Analysis,* vol. 30, p. 144–157, May 2016.

[206] Springer Handbook of Robotics, Springer International Publishing, 2016.

[207] H. Chen, W. Zhang and D. Yan, "Robust Visual Tracking with Reliable Object Information and Kalman Filter," *Sensors,* vol. 21, p. 889, January 2021.

[208] B. Sebastian and P. Ben-Tzvi, "Active Disturbance Rejection Control for Handling Slip in Tracked Vehicle Locomotion," *Journal of Mechanisms and Robotics,* vol. 11, February 2019.

[209] D. Bouget, M. Allan, D. Stoyanov and P. Jannin, "Vision-based and marker-less surgical tool detection and tracking: a review of the literature," *Medical Image Analysis,* vol. 35, p. 633–654, January 2017.

[210] W. L. Ng, S. Wang, W. Y. Yeong and M. W. Naing, "Skin Bioprinting: Impending Reality or Fantasy?," *Trends in Biotechnology,* vol. 34, p. 689–699, September 2016.

[211] S. Boyce, P. Chang and P. Warner, "Burn Dressings and Skin Substitutes," in *Biomaterials Science*, Elsevier, 2020, p. 1169–1180.

[212] C. M. Witten, R. D. McFarland and S. L. Simek, "Concise Review: The U.S. Food and Drug Administration and Regenerative Medicine," *Stem Cells Translational Medicine,* vol. 4, p. 1495–1499, October 2015.

[213] C.-C. Wei, A. B. Lin and S.-C. Hung, "Mesenchymal Stem Cells in Regenerative Medicine for Musculoskeletal Diseases: Bench, Bedside, and Industry," *Cell Transplantation,* vol. 23, p. 505–512, May 2014.

[214] C. Di Bella, A. Fosang, D. M. Donati, G. G. Wallace and P. F. M. Choong, "3D Bioprinting of Cartilage for Orthopedic Surgeons: Reading between the Lines," *Frontiers in Surgery,* vol. 2, August 2015.

[215] P. Datta, A. Barui, Y. Wu, V. Ozbolat, K. K. Moncal and I. T. Ozbolat, "Essential steps in bioprinting: From pre- to post-bioprinting," *Biotechnology Advances*, vol. 36, p. 1481–1504, September 2018.

[216] M. Hospodiuk, M. Dey, D. Sosnoski and I. T. Ozbolat, "The bioink: A comprehensive review on bioprintable materials," *Biotechnology Advances*, vol. 35, p. 217–239, March 2017.

[217] I. T. Ozbolat and B. Koc, "3D hybrid wound devices for spatiotemporally controlled release kinetics," *Computer Methods and Programs in Biomedicine*, vol. 108, p. 922–931, December 2012.

[218] W.-C. Yan, P. Davoodi, S. Vijayavenkataraman, Y. Tian, W. C. Ng, J. Y. H. Fuh, K. S. Robinson and C.-H. Wang, "3D bioprinting of skin tissue: From pre-processing to final product evaluation," *Advanced Drug Delivery Reviews*, vol. 132, p. 270–295, July 2018.

[219] I. T. Ozbolat, "Bioprinting scale-up tissue and organ constructs for transplantation," *Trends in Biotechnology*, vol. 33, p. 395–400, July 2015.

[220] D. L. Cohen, J. I. Lipton, L. J. Bonassar and H. Lipson, "Additive manufacturing for in situ repair of osteochondral defects," *Biofabrication*, vol. 2, p. 035004, September 2010.

[221] C. Di Bella, S. Duchi, C. D. O'Connell, R. Blanchard, C. Augustine, Z. Yue, F. Thompson, C. Richards, S. Beirne, C. Onofrillo, S. H. Bauquier, S. D. Ryan, P. Pivonka, G. G. Wallace and P. F. Choong, "in situ handheld three-dimensional bioprinting for cartilage regeneration," *Journal of Tissue Engineering and Regenerative Medicine*, vol. 12, p. 611–621, August 2017.

[222] A. N. Leberfinger, S. Dinda, Y. Wu, S. V. Koduru, V. Ozbolat, D. J. Ravnic and I. T. Ozbolat, "Bioprinting functional tissues," *Acta Biomaterialia*, vol. 95, p. 32–49, September 2019.

[223] P.-L. Tremblay, V. Hudon, F. Berthod, L. Germain and F. A. Auger, "Inosculation of Tissue-Engineered Capillaries with the Host's Vasculature in a Reconstructed Skin Transplanted on Mice," *American Journal of Transplantation*, vol. 5, p. 1002–1010, May 2005.

[224] V. H. Thourani, W. L. Ingram and D. V. Feliciano, "Factors Affecting Success of Split-Thickness Skin Grafts in the Modern Burn Unit," *The Journal of Trauma: Injury, Infection, and Critical Care*, vol. 54, p. 562–568, March 2003.

[225] J. E. Janis, R. K. Kwon and C. E. Attinger, "The New Reconstructive Ladder: Modifications to the Traditional Model," *Plastic and Reconstructive Surgery*, vol. 127, p. 205S–212S, January 2011.

[226] A. Perez-Valle, C. Del Amo and I. Andia, "Overview of Current Advances in Extrusion Bioprinting for Skin Applications," *International Journal of Molecular Sciences*, vol. 21, p. 6679, September 2020.

[227] Y.-J. Choi, H. Park, D.-H. Ha, H.-S. Yun, H.-G. Yi and H. Lee, "3D Bioprinting of In Vitro Models Using Hydrogel-Based Bioinks," *Polymers*, vol. 13, p. 366, January 2021.

[228] L. Piegl and W. Tiller, The NURBS Book, Springer Berlin Heidelberg, 1995.

[229] G. Hodgson, A. Ranellucci and J. Moe, "Slicer Mnaual- Flow Math," LulzBot- Aleph Objects, Inc, [Online]. Available: https://manual.slic3r.org/advanced/flow-math. [Accessed 12 12 2022].

[230] L. K. Narayanan, P. Huebner, M. B. Fisher, J. T. Spang, B. Starly and R. A. Shirwaiker, "3D-Bioprinting of Polylactic Acid (PLA) Nanofiber–Alginate Hydrogel Bioink Containing Human Adipose-Derived Stem Cells," *{ACS} Biomaterials Science {\&}amp$\mathsemicolon$ Engineering*, vol. 2, p. 1732–1742, July 2016.

[231] N. Leal, E. Leal and J. W. Branch, "Simple Method for Constructing NURBS Surfaces from Unorganized Points," in *Proceedings of the 19th International Meshing Roundtable*, Springer Berlin Heidelberg, 2010, p. 161–175.

[232] S. Sharifi, H. Sharifi, A. Akbari and J. Chodosh, "Systematic optimization of visible light-induced crosslinking conditions of gelatin methacryloyl (GelMA)," *Scientific Reports*, vol. 11, December 2021.

[233] N. Hakimi, R. Cheng, L. Leng, M. Sotoudehfar, P. Q. Ba, N. Bakhtyar, S. Amini-Nik, M. G. Jeschke and A. Günther, "Handheld skin printer: in situ formation of planar biomaterials and tissues," *Lab on a Chip*, vol. 18, p. 1440–1451, 2018.

[234] J. Xu, J. Ji, J. Jiao, L. Zheng, Q. Hong, H. Tang, S. Zhang, X. Qu and B. Yue, "3D Printing for Bone-Cartilage Interface Regeneration," *Frontiers in Bioengineering and Biotechnology*, vol. 10, February 2022.

[235] M. S. Chaudhry and A. Czekanski, "Tool Path Generation for Free Form Surface Slicing In Additive Manufacturing/Fused Filament Fabrication," in *Volume 2B: Advanced Manufacturing*, 2021.

[236] M. S. Chaudhry and A. Czekanski, "Slicing Procedure For Non-Planar Fused Filament Fabrication," in *Progress in Canadian Mechanical Engineering. Volume 4*, 2021.

[237] S. Hutchinson, G. D. Hager and P. I. Corke, "A tutorial on visual servo control," *IEEE Transactions on Robotics and Automation,* vol. 12, p. 651–670, 1996.

[238] N. Pettinelli, S. Rodríguez-Llamazares, R. Bouza, L. Barral, S. Feijóo-Bandín and F. Lago, "Carrageenan-based physically crosslinked injectable hydrogel for wound healing and tissue repairing applications.," *International journal of pharmaceutics,* p. 119828, 2020.

[239] Z. Yang, Z. Ma, S. Liu and J. Li, "Tissue adhesion with tough hydrogels: Experiments and modeling," *Mechanics of Materials,* vol. 157, p. 103800, 2021.

[240] M. S. Chaudhry and A. Czekanski, "In-situ bioprinting of skin - A review," *Bioprinting,* vol. 31, p. e00271, June 2023.

[241] B. J. Klotz, D. Gawlitta, A. Rosenberg, J. Malda and F. Melchels, "Gelatin-Methacryloyl Hydrogels: Towards Biofabrication-Based Tissue Repair.," *Trends in biotechnology,* vol. 34 5, pp. 394-407, 2016.

[242] J. Ramón-Azcón, S. Ahadian, R. Obregon, G. Camci-Unal, S. Ostrovidov, V. Hosseini, H. Kaji, K. Ino, H. Shiku, A. Khademhosseini and T. Matsue, "Gelatin methacrylate as a promising hydrogel for 3D microscale organization and proliferation of dielectrophoretically patterned cells.," *Lab on a chip,* vol. 12 16, pp. 2959-69, 2012.

[243] A. A. Adib, A. Sheikhi, M. Shahhosseini, A. Simeunovic, S. Wu, C. Castro, R. Zhao, A. Khademhosseini and D. Hoelzle, "Direct-write 3D printing and characterization of a GelMA-based biomaterial for intracorporeal tissue engineering," *Biofabrication,* vol. 12, 2020.

[244] L. Ning, R. Mehta, C. Cao, A. S. Theus, M. L. Tomov, N. Zhu, E. Weeks, H. Bauser-Heaton and V. Serpooshan, "Embedded 3D Bioprinting of Gelatin Methacryloyl-Based Constructs with Highly Tunable Structural Fidelity.," *ACS applied materials & interfaces,* 2020.

[245] C. O'Connell, S. Konate, C. Onofrillo, R. Kapsa, C. Baker, S. Duchi, T. Eekel, Z. Yue, S. Beirne, G. Barnsley, C. di Bella, P. Choong and G. Wallace, "Free-form co-axial bioprinting of

a gelatin methacryloyl bio-ink by direct in situ photo-crosslinking during extrusion," *Bioprinting,* vol. 19, 2020.

[246] C. Claaßen, M. H. Claaßen, V. Truffault, L. Sewald, G. E. M. Tovar, K. Borchers and A. Southan, "Quantification of Substitution of Gelatin Methacryloyl: Best Practice and Current Pitfalls," *Biomacromolecules,* vol. 19, p. 42–52, December 2017.

[247] M. Zhu, Y. Wang, G. Ferracci, J. Zheng, N.-J. Cho and B. H. Lee, "Gelatin methacryloyl and its hydrogels with an exceptional degree of controllability and batch-to-batch consistency," *Scientific Reports,* vol. 9, May 2019.

[248] M. S. Chaudhry and A. Czekanski, "Surface Slicing and Toolpath Planning for In-situ Bioprinting of Skin Implants," *(accepted) Biofabrication* , 2023.

[249] M. S. Chaudhry and A. Czekanski, "Visual Control for Robotic 3D Printing on a Moving Platform," *(Under 2nd Revision) Mechatronics* , 2023.

[250] M. S. Chaudhry and A. Czekanski, "Rheological and Mechanical Transformations of Gelatin Methacrylol (Gelma) with Cellulose Nanofibrils," *(Under Revision) Materials Characterization* , 2023.

[251] M. S. Chaudhry and A. Czekanski, "Evaluating FDM Process Parameter Sensitive Mechanical Performance of Elastomers at Various Strain Rates of Loading," *Materials,* vol. 13, p. 3202, July 2020.

[252] S. Chaudhry, M. Al-Dojayli and A. Czekanski, "Performance of 3-D Printed Thermoplastic Polyurethane Under Quasi-Static and High-Strain Rate Loading," in *Volume 9: Mechanics of Solids, Structures and Fluids; NDE, Diagnosis, and Prognosis*, 2016.

Appendix A

Algorithm A-I: Slicing and Surface Intersection for 3D Model Layer Generation

Input: slicingSurface, model, layerHeight , SlicingDirection (TD/BU)

Output: slices, a list of intersected surfaces

Procedure:

1: Initialize slicingSurface to desired initial position
2: Compute bounding box for slicingSurface (boundS) and model (boundM)
3: Initialize sList as an empty list to store slicing surfaces
4: Set currentOffset to layerHeight
5: While True:
    a: Copy slicingSurface and move it vertically by currentOffset
    b: Append the moved surface to sList
    c: Increment currentOffset by layerHeight if BU (Bottom Up)
    d: Decrement currentOffset by layerHeight if TD (Top Down)
    e: If boundS within boundM, exit loop
6: If SlicingDirection is Top Down (TD), reverse sList
7: For each surface in sList:
    a: Intersect surface with model to create sliceSections
    b: If sliceSections is not None and is a list:
        i: Iterate over each sliceSection
        ii: Check if sliceSection is within model's bounding box and has threshold area
        iii: If true, add sliceSection to the list of slices
8: Record script execution time
End Procedure

Algorithm A-II: Tool Path Generation for Bioprinting

Input: sList.sections surfaces (slices), lineWidth, layerHeight, pts_per_lineWidth (parameters for printing)

Output: sList.toolpath, (Generated tool paths for bioprinting)

1: Initialize parameters (lineWidth, pts_per_lineWidth, layerHeight, etc.)
2: For each layer in the sList, do:
  2.1: Initialize data structures for the current layer (sections, sectionBoundaries, etc.)
  2.2: For each section in the current layer(sList.sections), do:
    2.2.1: Determine the bounding box of the section
    2.2.2: If the section area is above the threshold, do:
      2.2.2.1: Create seed points for toolpath generation
      2.2.2.2: Generate a first perimeter curve offset from the section edge
      2.2.2.3: Generate a second perimeter curve offset from the first
      2.2.2.4: Split the section using the second perimeter curve
      2.2.2.5: Check if the split section is inside the bounding box
      2.2.2.6: Generate tool paths by interpolating points along the surface
  2.3: Append generated tool paths to the current layer
3: Return the list of generated tool paths for all layers

Algorithm A-III: Tool Path Generation for G-code Output

Input: sList.toolpath

Output: toolpath.gcode

1. Start
2. Initialize variables and parameters
    2.1 Define the path and file name for G-code output
    2.2 Set parameters like lineWidth, nozzle diameter (diaNoz), layer height (layerH), and filament diameter (diaFil)
3. Open the file for writing G-code
4. Calculate the area for extrusion based on lineWidth, layerH, and diaFil
5. Write the start text for G-code file
6. Initialize the extrusion length (e) and position (p)
7. For each layer in the model:
   7.1 Write layer change commands in G-code
   7.2 For each section in the layer:
      7.2.1 Write section start commands in G-code
      7.2.2 For each curve in the section:
         7.2.2.1 Write curve start commands in G-code
         7.2.2.2 For each point in the curve:
            - Move the nozzle to the point coordinates
            - Calculate the incremental extrusion length
            - Write the movement and extrusion commands in G-code
   7.3 Write layer end commands in G-code
8. Write the end text for G-code file
9. Close the G-code file and End

Slicing and Toolpath Generation (Algorithm A)

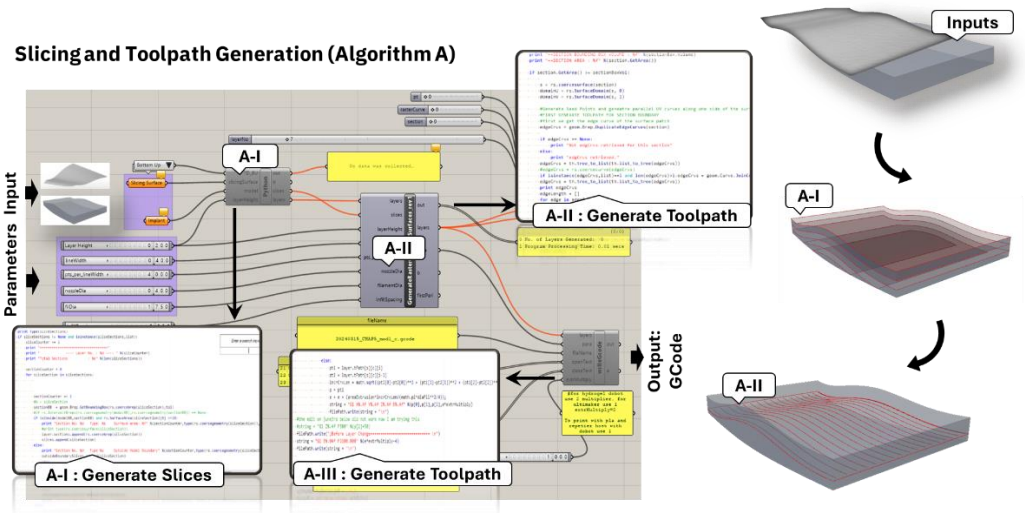

Algorithm B: Tracking Mechanism

Input: Calibrated image, Marker template

Output: Object position in world coordinates

1. Cast the image to an 8-bit unsigned integer format for standardized intensity values.
2. Set the calibration parameters based on the previously established camera model.
3. Match the known pattern or template within the image to identify the object of interest.
4. Refine pattern learning to enhance the precision of object detection.
5. Utilize a predefined marker template for consistent tracking of the object.
6. Process the image frame to extract object coordinates (u, v).
7. Apply a loop with a defined interval (100 ms) for real-time tracking.
8. Calculate the object's position in the camera frame using the homography matrix.
9. Transform the camera frame coordinates into world coordinates using rotation and translation matrices.

Algorithm C: Printer Control

Input: Xc: G-code Command Position, Xr: Robot Pose, Xg: Target Position for Printing, kp: Proportional Control Gain, Threshold: Motion Detection Threshold

Output: Xout: Output Position for the Printer Control

Begin

Initialize Loop Time to 20 ms. State Estimate X' to zero, Kalman Filter State

Loop:

Read G-code Command (Xc)

Read Robot Pose (Xr)

Kalman Predict Phase

Kalman Update Phase

Check Motion Detection

Embed and Process G-code

Serial Out

End Loop

End

Algorithm D: Calibration Procedure
Input: Image in native format **Output**: Target points in calibrated space 1. Convert the image format from native to U16 (16-bit unsigned integer). 2. Perform perspective calibration using intrinsic and extrinsic camera parameters. 3. Apply a thresholding operation to differentiate the target from the background. 4. Employ a particle filter to detect and analyze relevant features. 5. Learn the camera model, taking into account the specific characteristics of the camera used. 6. Transform the detected features into target points in the calibrated space.

Appendix B

Without Control Input (no IMU)

$$\hat{\boldsymbol{x}}_{n+1,n} = \boldsymbol{F}\hat{\boldsymbol{x}}_{n,n}$$

$$\begin{bmatrix} \hat{x}_{n+1,n} \\ \hat{y}_{n+1,n} \\ \hat{z}_{n+1,n} \\ \hat{\dot{x}}_{n+1,n} \\ \hat{\dot{y}}_{n+1,n} \\ \hat{\dot{z}}_{n+1,n} \\ \hat{\ddot{x}}_{n+1,n} \\ \hat{\ddot{y}}_{n+1,n} \\ \hat{\ddot{z}}_{n+1,n} \end{bmatrix} = \begin{bmatrix} 1 & 0 & 0 & \Delta t & 0 & 0 & 0.5\Delta t^2 & 0 & 0 \\ 0 & 1 & 0 & 0 & \Delta t & 0 & 0 & 0.5\Delta t^2 & 0 \\ 0 & 0 & 1 & 0 & 0 & \Delta t & 0 & 0 & 0.5\Delta t^2 \\ 0 & 0 & 0 & 1 & 0 & 0 & \Delta t & 0 & 0 \\ 0 & 0 & 0 & 0 & 1 & 0 & 0 & \Delta t & 0 \\ 0 & 0 & 0 & 0 & 0 & 1 & 0 & 0 & \Delta t \\ 0 & 0 & 0 & 0 & 0 & 0 & 1 & 0 & 0 \\ 0 & 0 & 0 & 0 & 0 & 0 & 0 & 1 & 0 \\ 0 & 0 & 0 & 0 & 0 & 0 & 0 & 0 & 1 \end{bmatrix} \begin{bmatrix} \hat{x}_{n,n} \\ \hat{y}_{n,n} \\ \hat{z}_{n,n} \\ \hat{\dot{x}}_{n,n} \\ \hat{\dot{y}}_{n,n} \\ \hat{\dot{z}}_{n,n} \\ \hat{\ddot{x}}_{n,n} \\ \hat{\ddot{y}}_{n,n} \\ \hat{\ddot{z}}_{n,n} \end{bmatrix}$$

With Control Input (IMU)

$$\hat{\boldsymbol{x}}_{n+1,n} = \boldsymbol{F}\hat{\boldsymbol{x}}_{n,n} + \boldsymbol{G}\boldsymbol{u}_n$$

$$\begin{bmatrix} \hat{x}_{n+1,n} \\ \hat{y}_{n+1,n} \\ \hat{z}_{n+1,n} \\ \hat{\dot{x}}_{n+1,n} \\ \hat{\dot{y}}_{n+1,n} \\ \hat{\dot{z}}_{n+1,n} \end{bmatrix} = \begin{bmatrix} 1 & 0 & 0 & \Delta t & 0 & 0 \\ 0 & 1 & 0 & 0 & \Delta t & 0 \\ 0 & 0 & 1 & 0 & 0 & \Delta t \\ 0 & 0 & 0 & 1 & 0 & 0 \\ 0 & 0 & 0 & 0 & 1 & 0 \\ 0 & 0 & 0 & 0 & 0 & 1 \end{bmatrix} \begin{bmatrix} \hat{x}_{n,n} \\ \hat{y}_{n,n} \\ \hat{z}_{n,n} \\ \hat{\dot{x}}_{n,n} \\ \hat{\dot{y}}_{n,n} \\ \hat{\dot{z}}_{n,n} \end{bmatrix} + \begin{bmatrix} 0.5\Delta t^2 & 0 & 0 \\ 0 & 0.5\Delta t^2 & 0 \\ 0 & 0 & 0.5\Delta t^2 \\ \Delta t & 0 & 0 \\ 0 & \Delta t & 0 \\ 0 & 0 & \Delta t \end{bmatrix} \begin{bmatrix} \ddot{x}_n \\ \ddot{y}_n \\ \ddot{z}_n \end{bmatrix}$$